

**MODAL EXPANSION ANALYSIS OF
MONOPOLE AND MICROSTRIP
ANTENNAS**

by

Zhongxiang Shen

**A thesis
presented to the University of Waterloo
in fulfilment of the
thesis requirement for the degree of
Doctor of Philosophy
in
Electrical Engineering**

Waterloo, Ontario, Canada, 1997

©Zhongxiang Shen 1997



**National Library
of Canada**

**Acquisitions and
Bibliographic Services**

**395 Wellington Street
Ottawa ON K1A 0N4
Canada**

**Bibliothèque nationale
du Canada**

**Acquisitions et
services bibliographiques**

**395, rue Wellington
Ottawa ON K1A 0N4
Canada**

Your file Votre référence

Our file Notre référence

The author has granted a non-exclusive licence allowing the National Library of Canada to reproduce, loan, distribute or sell copies of this thesis in microform, paper or electronic formats.

The author retains ownership of the copyright in this thesis. Neither the thesis nor substantial extracts from it may be printed or otherwise reproduced without the author's permission.

L'auteur a accordé une licence non exclusive permettant à la Bibliothèque nationale du Canada de reproduire, prêter, distribuer ou vendre des copies de cette thèse sous la forme de microfiche/film, de reproduction sur papier ou sur format électronique.

L'auteur conserve la propriété du droit d'auteur qui protège cette thèse. Ni la thèse ni des extraits substantiels de celle-ci ne doivent être imprimés ou autrement reproduits sans son autorisation.

0-612-30645-3

Canada

The University of Waterloo requires the signatures of all persons using or photocopying this thesis. Please sign below, and give address and date.

Abstract

Antenna problems are traditionally treated as open-region problems and solved by formulating one or two integral equations, whose solutions can be found analytically or numerically. Unlike most previous techniques available in the literature, this thesis presents an accurate and versatile technique for many canonical antenna problems. The proposed method treats the models, which are very close to the actual structures for practical engineering applications, in a very rigorous way. After properly introducing a boundary, the open-region antenna problems are transformed into "closed-region" guided-wave problems, which are then solved by the full-wave, formally exact modal expansion method. The distinguishing advantage of this approach to many antenna problems is that it can easily take into account all the effects of the feed line, junction discontinuities, and conductor thickness.

A number of techniques are introduced in this thesis to efficiently implement the modal expansion analysis. The "perfectly matched boundary", which is the combination of an electric wall and a magnetic wall, is used to truncate the free-space domain. An improved formulation for cascaded waveguide junctions is developed to save the computational effort involved in the modal expansion analysis.

Successful applications of the technique to various monopole and microstrip patch antennas are demonstrated. The input impedance and radiation pattern of various monopole antennas, including conventional monopole, sleeve monopole, dielectric-buried monopole, multilayer insulated monopole, and monopole on a finite ground plane, are thoroughly investigated by the proposed modal expansion method. Single and stacked circular and annular-ring microstrip patch antennas are also studied in detail in the thesis. Extensive computed results are presented for all the antenna structures considered.

Acknowledgements

First, I would like to express my deepest gratitude to my supervisor, Professor Robert H. MacPhie, for his constant support, invaluable guidance, and enthusiastic encouragement throughout the entire program of my studies at the University of Waterloo. Without his kind help, fruitful suggestions, and many hours of inspiring discussions we had in the past three and half years, nothing of the work reported in this thesis would have come true.

Second, I also wish to thank Professor S.K. Chaudhuri, Professor Y.L. Chow, Professor Wei-Ping Huang and Professor S. Safavi-Naeini for all they have taught me and for their useful comments on the thesis.

Third, I would also like to acknowledge my indebtedness to Dr. Gordon Strachan, Dr. Chenglin Xu, and Mr. Fred Ma for their help on computer programming.

Finally, my special thanks are due to my wife, Xinman Yang, for her dedication of love and her constant support and understanding.

Contents

1	Introduction	1
1.1	Review of Literature	4
1.1.1	Monopole Antennas	4
1.1.2	Microstrip Antennas	8
1.2	Organization of the Thesis	11
2	Theoretical Formulation for Monopole Antennas	13
2.1	Perfectly Matched Boundary	14
2.2	General Formulation	16
2.2.1	Description of the Problem	16
2.2.2	Field Component Expressions	19
2.2.3	Application of Boundary Conditions	23
2.2.4	Far-Field Radiation Pattern	28
2.3	Conclusions	32

3	Numerical Results for Monopole Antennas	33
3.1	Conventional Monopole Antennas	34
3.1.1	Comparison with Others' Data	37
3.1.2	Junction Effects	39
3.2	The Sleeve Monopole	47
3.3	Dielectric-Coated and Buried Monopoles	54
3.3.1	Dielectric-Coated Monopole	54
3.3.2	Dielectric-Buried Monopole	57
3.4	Insulated Monopoles	62
3.5	Monopole on a Finite Ground-Plane	69
4	Theoretical Formulation for Circular Microstrip Antennas	77
4.1	New Formulation for Cascaded Junctions	78
4.1.1	Enlargement-Reduction Cascaded Junctions	80
4.1.2	Derived Expressions for the Other Two Types	83
4.2	Simple Analysis of Open-Ended Waveguides	85
4.3	General Formulation for Circular Microstrip Antennas	92
4.4	Conclusions	99
5	Numerical Results for Circular Microstrip Antennas	101
5.1	Circular Patch Fed by a Centered Coaxial Line	102
5.2	Circular Patch Fed by an Off-Centered Cable	110

5.3	Annular-Ring Microstrip Antenna	117
5.4	Annular-Ring-Loaded Circular Disk Antenna	120
5.5	Stacked Circular Patch Antennas	122
5.6	Concluding Remarks	124
6	Conclusions	125
6.1	Summary of Contributions	125
6.2	Recommendations for Future Research	128
A	Waveguide Modal Functions	130
A.1	Parallel-Plate Waveguide	130
A.2	Rectangular Waveguide	131
A.3	Circular Waveguide	132
A.4	Coaxial Waveguide	133
B	E-Field Mode-Matching Matrices	135
B.1	Parallel-Plate Waveguide Junction	135
B.2	Rectangular Waveguide Junction	136
B.3	Circular-to-Circular Waveguide Junction	137
B.4	Coaxial-to-Circular Waveguide Junction	138
B.5	Coaxial-to-Coaxial Waveguide Junction	139
C	Expressions of Matrix Elements in (2.49)-(2.56)	141

D Derivation of (4.58)	143
Bibliography	146

List of Tables

3.1	Convergence of the admittance (Millimhos) of a quarter-wavelength monopole with respect to N_I ($a_I = 0.05985\lambda_0$, $b_I = 1.187a_I$).	35
3.2	Convergence of the admittance (Millimhos) of a quarter-wavelength monopole with respect to N_{II} ($a_I = 0.05985\lambda_0$, $b_I = 1.187a_I$).	36
3.3	Convergence of the impedance (Ohms) of a quarter-wavelength sleeve monopole with respect to N_I ($h = 0.25\lambda_0$, $l = 0.5\lambda_0$).	47
3.4	Convergence of the impedance (Ohms) of a quarter-wavelength sleeve monopole with respect to N_{II} ($h = 0.25\lambda_0$, $l = 0.5\lambda_0$).	48
3.5	Impedance of a sleeve monopole for different values of relative permittivity of the dielectric in the feed line ($h = l = 0.25\lambda_0$).	52
3.6	Input impedance of 0.5in diameter monopole elements on an 8ft diameter ground plane.	74
4.1	Comparison of computation time of our improved formulation and the generalized scattering matrix technique ($f = 11GHz$, $l = 15mm$).	82

4.2	Magnitude and phase of the reflection coefficient of an open-ended coaxial line with infinite flange. Case 1: using $\epsilon''_{r_2} = -0.1, -0.2, -0.3$ three points for extrapolation; Case 2: using $\epsilon''_{r_2} = -0.2, -0.4, -0.6$ three points; Case 3: using $\epsilon''_{r_2} = -0.5, -1.0, -1.5$ three points . . .	90
5.1	Convergence of the impedance (Ohms) of a circular disk antenna with respect to N_1 ($a_0 = 0.6mm, a = 30mm, k_0a = 3.5, \epsilon_r = 1, h = 1.5mm, t = 0.1mm$).	103
5.2	Convergence of the impedance (Ohms) of a disk antenna with respect to N_3 ($a_0 = 0.6mm, a = 30mm, k_0a = 3.5, \epsilon_r = 1, h = 1.5mm, t = 0.1mm$).	103
5.3	Comparison between our results and theoretical and experimental ones in [82] for the frequency (GHz) at minimum $10\log_{10} S_{110} ^2$ ($a_0 = 0.6mm, a = 30mm, \epsilon_r = 1, t = 0.1mm$).	105
5.4	Convergence of a circular microstrip antenna's impedance (Ohms) with respect to N_1 ($f = 2.65GHz$).	111
5.5	Convergence of a circular microstrip antenna's impedance (Ohms) with respect to N_3 ($f = 2.65GHz$).	111
5.6	Convergence of a circular microstrip antenna's impedance (Ohms) with respect to N_2 ($f = 2.65GHz$).	112

List of Figures

1.1	Geometry of a conventional monopole antenna.	5
1.2	A microstrip patch antenna fed by a coaxial line.	9
2.1	Illustration of perfectly matched boundary.	15
2.2	General configuration of a multilayer insulated sleeve monopole antenna.	17
2.3	Geometry of a sleeve monopole antenna.	29
3.1	Geometry of a conventional monopole antenna.	34
3.2	Variation of the input admittance of a monopole with respect to the distance d from the assumed PMB to the end of the monopole ($k_0 a_I = 0.05985$).	36
3.3	Surface current on a monopole antenna ($k_0 a_I = 0.04412$, $k_0 h = 0.75\pi$).	37
3.4	Input admittance of a monopole fed through an infinite ground plane by a coaxial line ($a_I = 0.0509\lambda_0$).	38
3.5	Radiated field pattern of a quarter-wavelength monopole antenna ($a_I = 0.0509\lambda_0$).	38

3.6	Three types of junction between the monopole and the feed line. . .	40
3.7	Input impedance of a monopole antenna shown in Figure 3.6(a) ($a_0 = 0.00397\lambda_0$, $a_0 = 1.33a_I$, $b_I = 1.67a_0$).	41
3.8	Effect of the junction between the feed line and the monopole on the antenna's admittance ($a_0 = 0.0509\lambda_0$, $b_I = 1.187a_I$).	42
3.9	Admittance of the monopole shown in Figure 3.6(b) ($b_I = 2.301a_I$).	43
3.10	Effect of the gap length t between the bottom of the monopole and the ground plane on the antenna's admittance ($a_I = 0.0509\lambda_0$, $b_I = 2.301a_I$, $a_0 = 3b_I$).	44
3.11	Equivalent circuit for characterizing the junction effect of the third type shown in Figure 2.6 (c).	45
3.12	Effect of the step junction between the monopole and the feed line on the antenna's admittance ($a_I = 0.0509\lambda_0$, $b_I = 2.301a_I$).	46
3.13	Variation of a sleeve monopole's impedance with respect to the distance d ($l = 0.45\lambda_0$, $h = 0.25\lambda_0$).	48
3.14	Surface current on a sleeve monopole antenna ($l = 0.45\lambda_0$, $h = 0.25\lambda_0$).	50
3.15	Comparison of our results for the impedance of a sleeve monopole with those obtained by others ($h = 0.25\lambda_0$).	50
3.16	Input impedance of a sleeve monopole for different sleeve lengths.	51
3.17	Radiation pattern of a sleeve monopole for different sleeve lengths ($h = 0.25\lambda_0$).	52
3.18	Input impedance of a sleeve monopole for different thicknesses of the sleeve.	53

3.19	Geometry of a dielectric-coated monopole antenna.	54
3.20	Variation of the admittance of a dielectric-coated monopole with respect to d ($b_I = 3a_I$, $a_1 = 11.43mm$, $h = 0.25\lambda_0$, $f = 600MHz$).	55
3.21	Admittance of a dielectric-coated monopole ($b_I = 3a_I$, $f = 0.6GHz$).	56
3.22	Geometry of a monopole antenna partially buried in a grounded substrate.	57
3.23	Input impedance loci of a monopole partially buried in a grounded dielectric substrate ($a_I = 6.35mm$, $b_I = 3.24a_I$).	58
3.24	Normalized radiated power vs. relative dielectric constant $\epsilon_{r,s}$ for a buried quarter-wavelength monopole ($k_0a_I = 0.05985$, $b_I = 2.301a_I$).	59
3.25	Normalized radiated power vs. substrate thickness t/h for a buried quarter-wavelength monopole ($k_0a_I = 0.05985$, $b_I = 2.301a_I$).	59
3.26	Resonant length vs. relative dielectric constant $\epsilon_{r,s}$ for the buried monopole ($a_I = 0.00635\lambda_0$, $b_I = 2.301a_I$).	60
3.27	Input impedance of a monopole half-buried in a grounded dielectric substrate for different dielectric permittivities ($k_0a_I = 0.05985$, $b_I = 2.301a_I$).	61
3.28	Geometry of an air-insulated monopole antenna.	62
3.29	Variation of the admittance of an air-insulated quarter-wavelength monopole in sand with respect to d ($a_I = 3.175mm$, $b_I = 3a_I$, $a_1 = 4a_I$, $f = 380MHz$).	63
3.30	Input admittance of an air-insulated monopole in lake water ($a_I = 3.175mm$, $b_I = 3a_I$, $a = 2 = a_1 = 4a_I$).	64

3.31	Current distribution on an air-insulated monopole antenna in sand ($a_I = 3.175mm$, $b_I = 3a_I$, $a_2 = a_1 = 4a_I$).	64
3.32	Input admittance of an air-insulated monopole antenna in sand ($a_I =$ $3.175mm$, $b_I = 3a_I$, $a_2 = a_1 = 4a_I$).	65
3.33	Variation of the admittance of an air-insulated quarter-wavelength monopole with respect to a_1/a_I ($a_I = 3.175mm$, $b_I = 2.301a_I$, $f_0 =$ $380MHz$).	66
3.34	Variation of the admittance of an air-insulated quarter-wavelength monopole with respect to the dielectric constant ϵ_r of the external medium ($a_I = 3.175mm$, $b_I = 2.301a_I$, $f_0 = 380MHz$).	67
3.35	Effect of the finite thickness of the insulating layer on a monopole's admittance ($a_I = 3.175mm$, $b_I = 2.301a_I$, $a_1 = 4a_I$).	68
3.36	Theoretical model for a monopole over a finite ground plane.	69
3.37	Variation of the impedance of a monopole with respect to a_1/λ_0 ($a_I = 1.588mm$, $b_I = 5.2mm$, $a_1 = 75mm$).	72
3.38	Variation of the impedance of a monopole with respect to the nor- malized radius a_1/λ_0 of the ground plane (same parameters as Figure 3.37).	75
3.39	Impedance of a monopole as a function of a_1/λ_0 with its thickness as a parameter (same parameters as Figure 3.37).	76
4.1	Three types of two cascaded waveguide junctions.	79
4.2	Side-view of an open-ended waveguide and its simplified waveguide junction model.	86

4.3	Variation of the reflection coefficient of an open-ended coaxial line with respect to the radius of the large circular waveguide for different values of loss tangent ($f = 6GHz$).	88
4.4	Magnitude and phase of the reflection coefficient of a coaxial line terminated by an infinite flange ($a_1 = 1.4364mm$, $b_1 = 4.725mm$, $\epsilon_{r1} = \epsilon_{r2} = 2.05$).	89
4.5	Aperture admittance of an open-ended rectangular waveguide with infinite flange ($a = 2.25b$).	91
4.6	Analysis model of an annular-ring-loaded stacked circular microstrip patch antenna.	93
5.1	Geometry of a circular patch antenna fed by a centered coaxial line and covered by a superstrate.	102
5.2	Variation of the input impedance of a circular patch with respect to the radius of the assumed boundary ($a_0 = 0.6mm$, $a = 30mm$, $f = 6GHz$, $\epsilon_r = 1$, $h = 1.5mm$, $t = 0.1mm$).	104
5.3	Input impedance of a circular patch antenna fed by a centered coaxial line ($a_0 = 0.6mm$, $a = 30mm$, $\epsilon_r = 1$, $h = 1.5mm$, $t = 0.1mm$). . . .	105
5.4	Effect of the superstrate on the circular patch antenna's impedance ($a_0 = 0.5mm$, $a = 30mm$, $a = 15mm$, $h = 1.6mm$, $t = 0.1mm$, $\epsilon_r^p = \epsilon_r^b$).	106
5.5	Effect of the finite thickness of the circular patch on the antenna's impedance ($a_0 = 0.5mm$, $a = 15mm$, $h = 1.6mm$, $t = 0.1mm$, $\epsilon_r = 1$).108	

5.6	Effect of the anisotropy of the substrate and superstrate on a circular patch antenna's impedance ($a_0 = 0.5mm$, $l = h$, $t = 0.1mm$, $\epsilon_{r_2}^b = \epsilon_{r_2}^p = 3.4$).	109
5.7	Geometry of a circular patch antenna fed by an off-centered coaxial line.	110
5.8	Impedance loci of a circular microstrip antenna for different values of b_1 , the size of the outer cylindrical wall ($a_0 = 0.45mm$).	113
5.9	Impedance loci of a circular microstrip antenna fed by an off-centered coaxial line.	113
5.10	Radiated E-field patterns of a circular microstrip antenna at resonance and at off-resonance.	114
5.11	Impedance loci of a circular microstrip antenna for different values of a_0	115
5.12	Impedance loci of a circular microstrip antenna for different values of d	115
5.13	Input impedance of a circular microstrip antenna for different substrate thicknesses.	116
5.14	Effect of the finite thickness of the patch on the input impedance of a circular microstrip antenna ($a_0 = 0.32mm$, $b_0 = 2.301a_0$, $a_1 = 5mm$, $h = 1.2mm$, $d = 2mm$, $\epsilon_r = 2.6$).	116
5.15	Effect of the substrate's anisotropy on the input impedance of a circular microstrip antenna ($a_0 = 0.8mm$, $b_0 = 2.301a_0$, $a_1 = 20mm$).	118
5.16	Geometry of an annular-ring patch antenna fed by a coaxial line.	119

5.17	Input impedance of an annular-ring microstrip antenna fed by an off-centered coaxial line.	119
5.18	Geometry of an annular-ring-loaded circular microstrip antenna fed by a coaxial line.	120
5.19	Input impedance of an annular-ring-loaded circular microstrip antenna fed by an off-centered coaxial line.	121
5.20	Geometry of a stacked circular microstrip antenna fed by an off-centered coaxial line.	122
5.21	Impedance loci of a stacked circular microstrip antenna fed by an off-centered coaxial line.	123
A.1	Parallel-plate waveguide.	130
A.2	Rectangular waveguide.	132
B.1	Parallel-plate to parallel-plate waveguide junction.	135
B.2	Rectangular-to-rectangular waveguide junction.	137
B.3	Circular-to-circular waveguide junction.	137
B.4	Coaxial-to-circular waveguide junction.	138
B.5	Junction between two noncollinear coaxial waveguides.	139

Chapter 1

Introduction

Antennas are a fundamental link in the ability to communicate with and sense the world around us. They are the windows upon which complex electronic systems must rely. Every wireless communication system needs two antennas to fulfill the task of transmitting and receiving electromagnetic energy which usually contains the information to be exchanged. An antenna acts as the electromagnetic transducer which is designed to convert guided waves within a transmission line to radiated free-space waves or to convert free-space waves to guided waves. The antenna serves a communication system the same purpose that eyes and eyeglasses serve a human.

Since Heinrich Hertz experimentally verified in 1887 the wave phenomena predicted by Maxwell's electromagnetic theory, an immense variety of antenna structures have been built and extensively investigated. Various types of antenna structures are used in many aspects of our daily lives. The size of antennas can vary significantly from a couple of centimeters to hundreds of meters in diameter, while their physical shapes can also be quite diverse. The physical shape and size of an

antenna determine its performance in free space. The performance of an antenna plays an important role in the overall performance of a communication system. A good design of the antenna can relax system requirements and improve overall system performance.

Numerous books have been published on this old and yet vivid subject—analysis and design of antennas. Accurate analysis of various antenna structures not only provides better physical understanding of the existing antennas, but also is the fundamental part of designing these antennas. Furthermore, theoretical analysis is the main means to suggest novel antenna structures. Generally, the theoretical analysis of antennas is carried out into two steps: the formulation of a theoretical model which corresponds, as closely as possible, to the actual antenna, and the analysis of the model using a particular mathematical technique. The theoretical model used to characterize the antenna usually involves approximations introduced to simplify the analysis. For example, for the cylindrical dipole antenna, the first antenna which Hertz used to perform his famous experiments, an idealized source is often used—the so-called “delta-function” generator. This source does not correspond to any realizable experimental structure. For planar microstrip antennas, the infinitely thin patch and infinitely large ground plane are usually assumed in their models. Moreover, the equations involved are often also approximate. For instance, for the cylindrical dipole antenna, the thin-wire approximation is often invoked to simplify the exact integral equation. Approximations like these mentioned above, lead to the discrepancies between theoretical and experimental results, and it is often difficult to quantitatively account for the effects of the different approximations.

With the advent of high-speed computers, accurate analysis of various antennas is becoming a reality, and the discrepancies between theoretical and experimental

results are being greatly decreased. The method of moments [1] presented about three decades ago dominates the analysis and design of most small antennas. Recently, the finite-difference time-domain (FDTD) method [2] has been attracting increased attention due to its distinctive advantages. These methods are very general and can handle any arbitrary antenna structures in theory, but both require extensive computer resources. Their efficiency is still a problem as far as design is concerned at this stage of computer development.

This thesis is primarily concerned with the accurate analysis of two different types of antenna. One is the widely-used cylindrical monopole antenna and the other is the microstrip patch antenna of circular shape. There are extensive works reported on these two antennas in the past, and they will be individually reviewed in the next section. Unlike most previous work, which directly dealt with the open-region antenna problems, this thesis presents a new technique: transform the open-region antenna problems to “closed-region” guided-wave problems and solve the resulting waveguide problems by the modal expansion method. The transformation is realized by simply introducing an appropriate boundary to partially enclose the antenna structure. The purpose of employing this transformation is to facilitate expressing the electromagnetic fields by discrete modal functions weighted by some unknown coefficients. As will be seen later, this modal expansion method can rigorously account for the effect of the feed line, which was often approximated by a delta voltage or a line current in most previously reported works. Furthermore, finite thicknesses of conductors can also be taken into consideration in this technique. Therefore, the models with which this thesis is primarily concerned are very close to those used in practical applications. The modal-expansion method employed in the thesis as the mathematical treatment is formally exact and can provide very accurate results.

1.1 Review of Literature

This section reviews the extensive work devoted to cylindrical monopole antennas and microstrip patch antennas with circular geometries. The cylindrical monopole antenna, which will be briefly reviewed in the first subsection, has been widely used in communication systems, remote sensing, probing, measuring and medical systems. The microstrip planar antennas has been evolving into one of the most useful antenna structures during the past two decades and will be separately reviewed in the second subsection.

1.1.1 Monopole Antennas

The problem of a monopole fed through an infinite conducting ground plane by a coaxial line has received extensive attention in the literature. The conventional model with which most previous research works dealt is illustrated in Figure 1.1, where the monopole is actually the extended inner conductor of the coaxial feed line over the ground plane.

R.W.P. King carried out extensive investigations on this classical antenna problem; many useful data for practical applications are graphically and tabularly given in his books [3], [4]. Chang [5] solved the problem of an electrically thick tubular monopole driven by a voltage across a finite gap by formulating an integral equation for the current distribution on the monopole. Morris [6] presented a rigorous mathematical analysis of a tubular monopole based on the model shown in Figure 1.1 by establishing a coupled pair of singular integral equations whose numerical solution is not easily attainable. An accurate computation of the performance of this monopole antenna by using the finite difference time domain method was performed by Maloney et al. [7]. Do-Nhat and MacPhie [8] introduced a full-wave

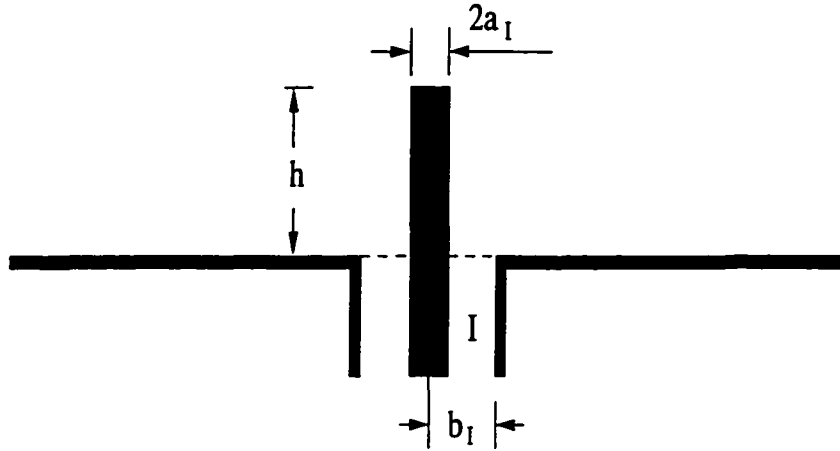


Figure 1.1: Geometry of a conventional monopole antenna.

analysis of this monopole problem by the conservation of complex power technique (CCPT).

The sleeve-monopole antenna is basically an extended structure of the conventional monopole with the outer conductor of the coaxial feed line projected over the ground plane. The projected sleeve acts as another tubular cylindrical antenna which can be used to adjust the performance of the monopole. The sleeve-monopole antenna has been widely used in wireless communication systems and remote sensing due to its broad-band characteristics [9] and horizontally omnidirectional radiation pattern.

The sleeve antenna was thoroughly investigated by Taylor [10] about 45 years ago and some of his important results were summarized in King's classic book [3]. King [3] and Taylor [10] employed the method of images and the superposition theorem to determine the currents on the monopole and on the sleeve, but they did not take into account the effect of the different radii of the monopole and the sleeve. Recently, Rispin and Chang [11] introduced a simple thin-wire analysis for sleeve antennas as well as other wire antennas by constructing the standing-wave current

on the antenna surface. Wunsch [12] determined the impedance and radiation pattern of the sleeve-monopole antenna by using a Fourier series representation of its surface current.

The characteristics of a monopole antenna can be greatly influenced by coating the monopole with a dielectric layer. An important experimental investigation was carried out by Lamensdorf [13] to examine the effect due to the coating dielectric. Several numerical techniques such as: the integral equation technique [14], the moment method [15], and the Wiener-Hopf technique [16] were reported to theoretically predict the input impedance of the dielectric-coated monopole.

A similar problem of a vertical monopole antenna partially or entirely buried in a grounded dielectric substrate has attracted some attention [17], [18] because the structure has found application such as a monopole submerged partially or entirely in soil or water and as the feed structure of a microstrip antenna. Of all the numerical techniques developed for this problem, the moment method in conjunction with various integral equation formulations [17], [18] appears to be the most rigorous one. Nevertheless, this technique involves numerical evaluation of the Sommerfeld integral and most of the previous work is limited to the case of thin monopoles.

Insulated antennas have found wide applications in subsurface communication, geophysical exploration, and biomedical telemetry. The insulation layer between the antenna and the ambient medium not only prevents a direct contact of the antenna with its surrounding material and the leakage of electric charges into a conducting medium, but also provides flexibilities in controlling the current distribution on the antenna and the resulting radiation pattern and input impedance [19]. An insulated linear antenna consists of a metal wire enclosed in a cylinder that is usually composed of a low-loss dielectric material. When such a two-layered

structure is immersed in an extended medium that is often characterized by a wave number larger in magnitude than the wave number of the insulating material, the radiation properties of the antenna differ significantly from those of the bare antenna. Considerable theoretical and experimental investigations of the insulated antenna have been performed by King [20], [21], Wu [22], and Lee [23], [24]. Unfortunately, much of their work is restricted to the case where the complex permittivity of the exterior medium is much greater than that of the insulating layer. Lee [23] extended the applicable range of the transmission line solution based on a complicated formulation. Furthermore, most attention of the previous work was focused on the current and charge distributions along the insulated antenna.

Monopole antennas, as shown in Figure 1.1, are not physically realizable since the ground plane, in reality, can not be of infinite extent. It is important and of practical value to understand the effect of the finite ground plane on the monopole's performance. There are a number of techniques available in the literature for predicting the effect of diffraction by the finite ground plane on a monopole antenna. As early as in 1930, Bardeen [25] determined the electromagnetic fields generated by the current on a ground plane of small radius by using the integral equation method. The input impedance of a monopole over a circular disk was experimentally measured by Meier and Summers [26]. Leitner and Spence [27] and Hahn and Fikioris [28] employed oblate spheroidal wave functions to study the effect of the finite ground plane on the monopole's radiation. A variational formula for the impedance of a monopole on a large circular ground plane was derived by Storer [29]. A hybrid method, which combines the moment method with the geometrical theory of diffraction (GTD), was also successfully applied to this practical problem [30]. Wait and Surtees [31] obtained an approximate expression for the impedance of a monopole at the center of a circular disk on the flat earth. A similar problem of

a monopole on a thick cylinder over a ground plane was studied by Yung and Butler [32] by formulating coupled integral-differential equations for the evaluation of the current distribution on the antenna surface and the electric field in the annular aperture of the coaxial line feed. Richmond [33] developed the sinusoidal-Galerkin moment method for the input impedance of a monopole antenna on a finite ground plane. Weiner [34] carried out a thorough study for the input impedance and directive gain of a monopole at the center of a circular ground plane whose radius is small or comparable to a wavelength. Most of these works addressed above are limited to the case of a monopole over a finite ground plane with zero thickness.

1.1.2 Microstrip Antennas

Microstrip antennas have been one of the most innovative topics in current antenna theory and design, and are increasingly finding application in a wide range of modern communication systems. A microstrip antenna consists of a metallic patch residing on a grounded dielectric substrate. The patch is fed either by a microstrip line or by a coaxial probe through the ground plane, as shown in Figure 1.2 for the coaxial line feeding structure. The microstrip patch antenna has many unique and desirable features such as compatibility with integrated-circuit technology, thin profile, light weight, low-cost, conformability to a shaped surface, and easy fabrication into linear or planar arrays. Due to these features, microstrip patch antennas have been extensively investigated experimentally, analytically, and numerically in the past two decades.

The idea of the microstrip antenna dates back to the 1950's [35], but it was not until the 1970's that serious attention was given to this element. Among a variety of patch shapes, microstrip antennas with rectangular and circular patches are the

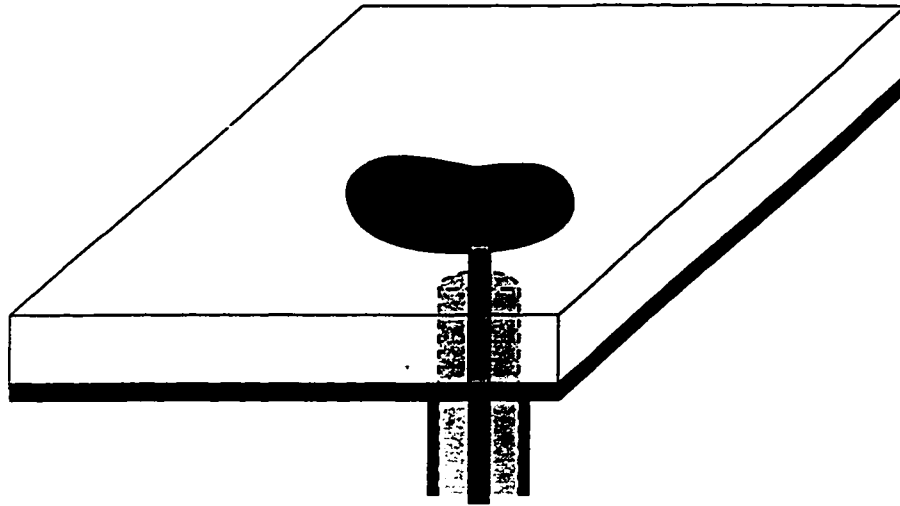


Figure 1.2: A microstrip patch antenna fed by a coaxial line.

most-widely used in engineering applications. In the following, microstrip antennas with circular geometries will be reviewed.

The first important theoretical work on microstrip antennas of regular shapes was due to Lo et al. [36], who developed the cavity model to predict the impedance and radiation pattern of rectangular and circular patch antennas. The Hankel transform was used by Chew and Kong [37] and Araki and Itoh [38] to analyze the circular microstrip disk antenna. A Green's function technique was applied by Yano and Ishimaru [39] to study the input impedance of a circular patch antenna. Davidovitz and Lo [40] considered the effect of the off-centered feed probe on the input impedance of a circular disk antenna. The moment method was also employed by Bailey and Deshpande [41] and Kishk and Shafai [42] to study the input impedance and radiation characteristics of a circular microstrip antenna. Accurate characterization of microstrip antennas was conducted in [43] by the finite-difference time-domain (FDTD) method. Radiation and scattering from a probe-fed microstrip antenna was investigated by Aberle et al. [44]. The annular-ring mi-

crostrip antenna has also been investigated; Chew [45] and Ali et al. [46] found that annular-ring planar antennas can be excited in TM_{12} mode for broad-band operation.

It was realized quite early in the development of microstrip antenna technology that patch antennas have a major limitation of narrow bandwidth. There are a number of ways to circumvent this limitation. One way is use to a thick substrate, which may excite a strong surface wave. Another way to broaden the bandwidth is to use another passive patch that resonates at a frequency which is very close to that of the driven patch. Nie et al. [47] carried out a study of the annular-ring-loaded circular microstrip antenna. The loading annular-ring can widen the bandwidth of a circular disk antenna. Circular microstrip antennas of stacked configurations were proposed by Long and Walton [48] and studied by Tulintseff et al. [49] to overcome the inherent narrow bandwidth limitation of the single circular patch antenna. Stacked annular-ring structure was also experimentally investigated in [50] for dual-frequency application.

Microstrip antennas on uniaxial substrates have been receiving attention in the recent years since most substrates used at microwave frequencies exhibit anisotropy. Due to its narrow-band nature, it is important to predict the effect of the substrate's anisotropy on the microstrip antenna's resonant frequency. Pozar [51] and Nelson et al. [52] studied the effect of the substrate's anisotropy on a rectangular microstrip antenna's performance.

In most published works mentioned above, the coaxial feed line is often approximately modeled by an idealized probe current source; this is inadequate in correctly predicting the input impedance when the thickness of the substrate is greater than $0.02\lambda_0$, where λ_0 is the wavelength in free-space. Moreover, most previous works neglected the finite thickness of the patch, which may have a noticeable effect on

the antenna's performances at millimeter-wave bands.

1.2 Organization of the Thesis

The rest of the thesis is organized as follows. Chapter 2 presents a unified formulation for modeling a multilayer insulated sleeve monopole antenna. The geometry of the monopole considered is quite general and will reduce to many practical antennas under certain circumstances. Chapter 2 begin with an introduction of a "perfect matched boundary" (PMB), which is simply a combination of an electric wall and a magnetic wall. After that, a detailed formulation for determining the input impedance and radiated field pattern of the general insulated sleeve monopole antenna is given.

Chapter 3 is solely devoted to numerical results and discussions for various monopole antennas. Considered in this chapter are the conventional monopole with emphasis on characterizing the junction effect, the sleeve monopole antenna, the dielectric-coated and -buried monopoles, the insulated monopole antenna and a monopole over a finite ground plane. Extensive computed results are presented and compared with results obtained by others.

Chapter 4 starts with the introduction of two useful techniques which will be employed in the analysis of circular microstrip antennas. The first technique is an improved formulation for two cascaded waveguide junctions. The other is a simple technique for calculating the reflection coefficient of an open-ended waveguide. The detailed formulation for a stacked annular-ring-loaded circular microstrip antenna is then presented in this chapter.

Chapter 5 provides computed results for various microstrip antennas with cir-

cular geometries. Considered in this category are a single circular disk fed by a centered coaxial line, a circular patch antenna fed by an off-centered coaxial cable, an annular-ring microstrip antenna, annular-ring-loaded circular patch antenna, and a stacked circular microstrip antenna. Comparison of calculated results with experimental data available in the literature is made and good agreement is observed.

Chapter 6 is the last chapter of this thesis; it summarizes the major contributions made in the dissertation and recommendations for further research work are given.

Chapter 2

Theoretical Formulation for Monopole Antennas

This chapter presents a unified formulation for a general configuration of monopole antennas. Considered in the category of the monopole antennas are the conventional monopole with emphasis on the junction effect, the sleeve monopole, dielectric-coated and -buried monopole antennas, multilayer insulated monopole antennas, and a monopole over a finite ground plane. The unified formulation presented below can handle all the monopole structures mentioned above except the last one, which is solved by a slightly different treatment in the next chapter. This chapter begins with the introduction of a “perfectly matched boundary” (PMB), which is simply the combination of an electric wall and a magnetic wall. While the PMB is simple in the form, the theoretical reflection factor of a plane wave striking it is null at any frequency, any incidence angle and any polarization. After employing this PMB, the open-region monopole antenna problem is transformed into a “closed-region” guided-wave problem, which is then formulated in detail

by the modal expansion method. An efficient recursive algorithm based on 2 by 2 matrix multiplications is introduced to implement the analysis of an arbitrary multilayer structure. Expressions for calculating the far-field radiation pattern are derived. Chapter 3 will be solely devoted to extensive numerical results for all these practical examples.

2.1 Perfectly Matched Boundary

The basic idea of the PMB is very similar to the even-odd excitation theory which has been widely used for symmetric structures such as branch-line directional couplers. As illustrated in Figure 2.1, the PMB is simply the combination of an electric wall and a magnetic wall. The reflectionless properties of a plane-wave incident on a PMB will be briefly proved here.

Consider a plane-wave incident on a perfectly conducting plate [Figure 2.1(a)], which coincides with the $x - y$ plane at $z = 0$. The electromagnetic fields of an incident plane wave are

$$\vec{E}_i = \vec{E}_{i0} \exp(-j\vec{k}_i \cdot \vec{r}) \quad (2.1)$$

$$\vec{H}_i = \frac{1}{\omega\mu} \vec{k}_i \times \vec{E}_{i0} \exp(-j\vec{k}_i \cdot \vec{r}) \quad (2.2)$$

where $\vec{E}_{i0} = \hat{x}E_{x0} + \hat{y}E_{y0} + \hat{z}E_{z0}$ and $\vec{k}_i = \hat{x}k_x + \hat{y}k_y + \hat{z}k_z$. The electromagnetic fields of the reflected wave can be easily found [53] and have the form of

$$\vec{E}_r^e = \vec{E}_{r0}^e \exp(-j\vec{k}_r^e \cdot \vec{r}) \quad (2.3)$$

$$\vec{H}_r^e = \frac{1}{\omega\mu} \vec{k}_r^e \times \vec{E}_{r0}^e \exp(-j\vec{k}_r^e \cdot \vec{r}) \quad (2.4)$$

where $\vec{E}_{r0}^e = -\hat{x}E_{x0} - \hat{y}E_{y0} + \hat{z}E_{z0}$ and $\vec{k}_r^e = \hat{x}k_x + \hat{y}k_y - \hat{z}k_z$.

Similarly, the reflected electromagnetic fields of the same plane wave (2.1) and (2.2) striking a magnetic wall [Figure 2.1(b)] are

$$\vec{E}_r^m = \vec{E}_{r0}^m \exp(-j\vec{k}_r^m \cdot \vec{r}) \quad (2.5)$$

$$\vec{H}_r^m = \frac{1}{\omega\mu} \vec{k}_r^m \times \vec{E}_{r0}^m \exp(-j\vec{k}_r^m \cdot \vec{r}) \quad (2.6)$$

where $\vec{E}_{r0}^m = \hat{x}E_{x0} + \hat{y}E_{y0} - \hat{z}E_{z0} = -\vec{E}^e$ and $\vec{k}_r^m = \hat{x}k_x + \hat{y}k_y - \hat{z}k_z = \vec{k}_r^e$.

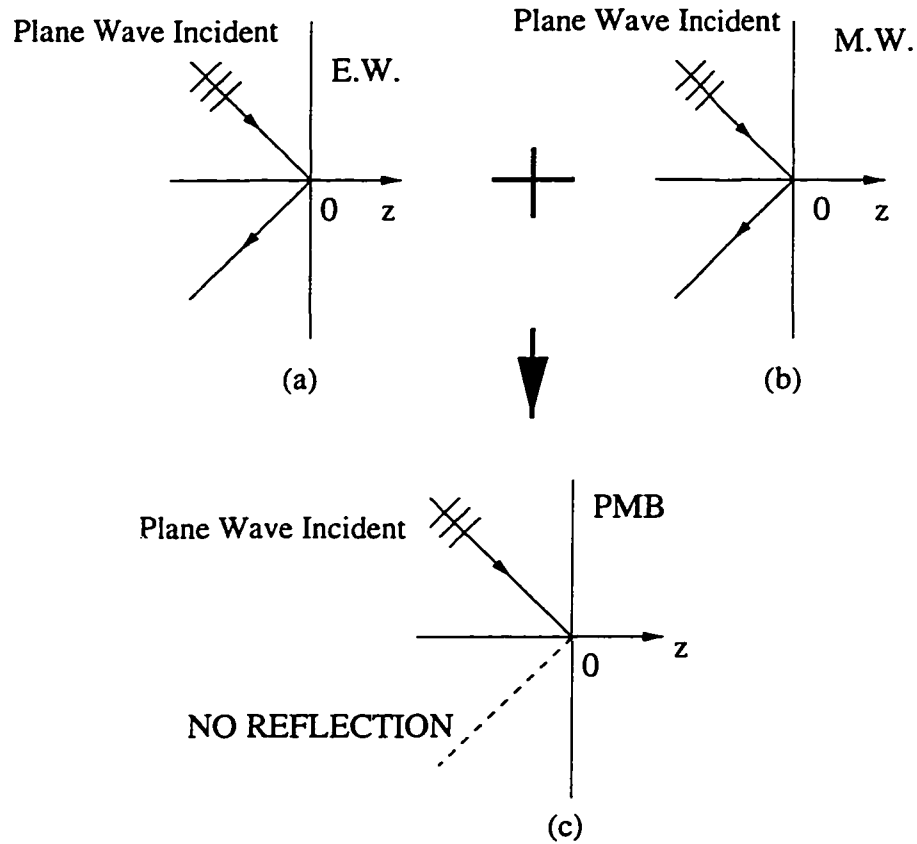


Figure 2.1: Illustration of perfectly matched boundary.

It is obvious that the reflected wave in (2.5) and (2.6) for a magnetic wall exactly cancels that in (2.3) and (2.4) for an electric wall. Therefore, if we sum up these two reflected waves, we have no reflection. That is to say, the PMB, the

combination of an electric wall and a magnetic wall, will produce a perfectly reflectionless (matched) boundary for plane waves of any frequency, arbitrary incidence, and arbitrary polarization. This PMB will be used to transform the open-region monopole antenna problem into a “closed-region” guided-wave problem in the next section.

2.2 General Formulation

2.2.1 Description of the Problem

The theoretical model that we employ to characterize an N -layer insulated sleeve monopole antenna fed by a coaxial transmission line is shown in Figure 2.2, where a perfectly matched boundary (PMB) is placed parallel to the ground plane at a distance d from the end of the monopole. It is noted that there is a step junction between the monopole and the coaxial feed line [21]. An infinite grounded dielectric substrate of thickness t is also included in the configuration. Therefore, the structure of the problem shown in Figure 2.2 is quite general and will reduce to many special cases under certain conditions. All these resulting practical structures will be thoroughly studied in the next chapter.

As illustrated in Figure 2.2, the inner and outer radii of the coaxial feed line are a_I and b_I , respectively, while the radius of the monopole antenna is a_0 ($a_0 \leq a_I$). The inner and outer radii of the sleeve are assumed to be a_1 and a_2 , respectively, with their difference $a_2 - a_1$ being the thickness of the sleeve. The dielectric constant in region i ($i = 1, 2, \dots, N + 1$) is ϵ_i . For simplicity of presenting the formulation below, we assume that the thickness of the dielectric substrate is equal to or less than the length of the sleeve, i.e., $t \leq l$.

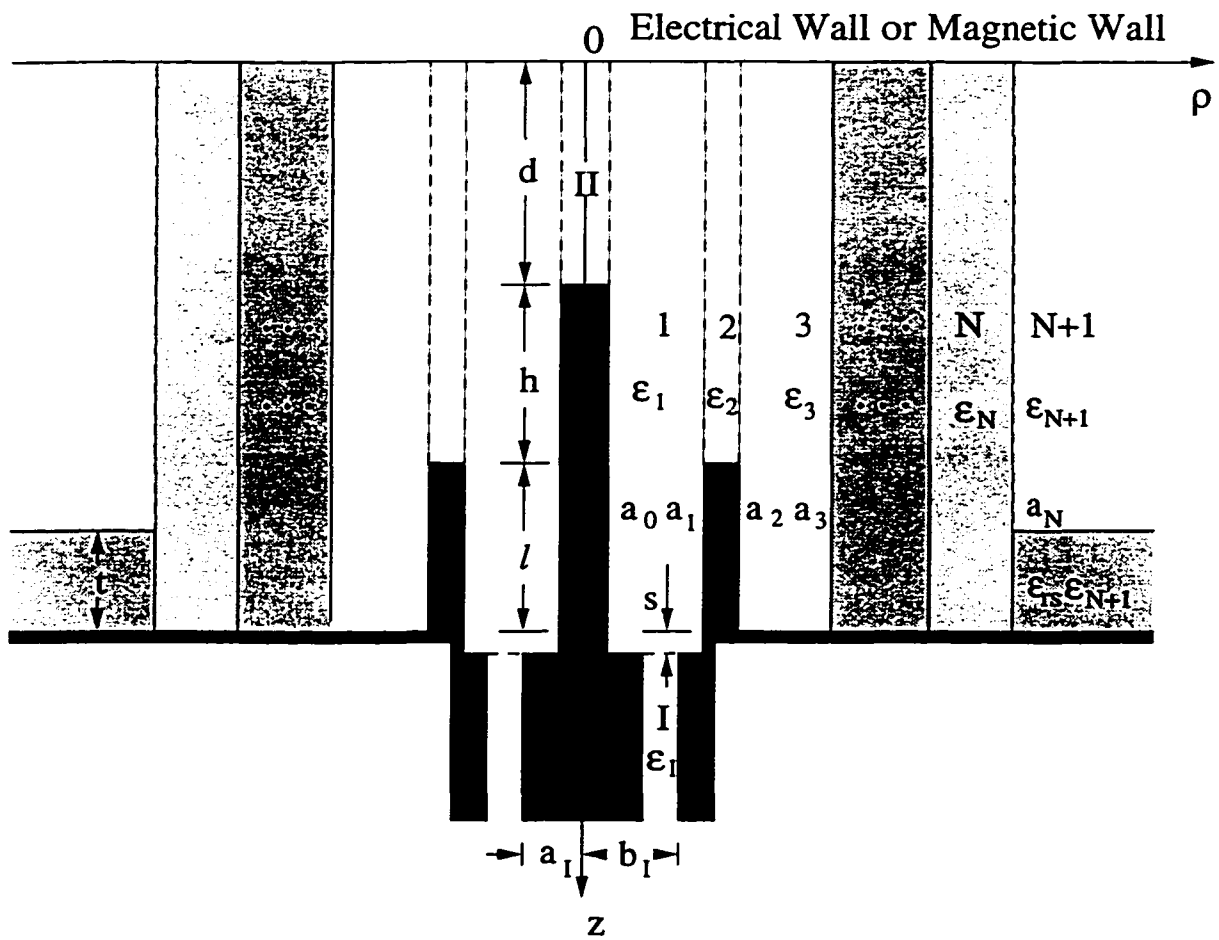


Figure 2.2: General configuration of a multilayer insulated sleeve monopole antenna.

As introduced in the previous section, the PMB, which is the combination of an electric wall and a magnetic wall, can completely absorb a plane wave of any frequency, any incident angle, and any polarization. Moreover, the major radiation of the monopole antenna occurs in the radial direction and the radiated power in the vertical direction is null. Therefore, it is expected that the introduced PMB does not have significant effect on the antenna's radiation. The analysis of the N -layer insulated sleeve monopole antenna requires the solution of the two problems: one with a parallel electric wall and the other with a parallel magnetic wall; they are both solved by the modal expansion method. The reflection coefficient at the feed point, which is related to the antenna's input impedance, and the current distribution, which is used to compute the far-region radiation pattern, are then obtained by halving the sum of these two results. For example, the total reflection coefficient Γ_{in} in the feed coaxial waveguide is calculated using

$$\Gamma_{in} = \frac{1}{2}(S_{11}^e + S_{11}^m) \quad (2.7)$$

where S_{11}^e and S_{11}^m are the reflection coefficients of the dominant TEM mode in the feed line with an electric wall and a magnetic wall placed at a distance d from the top of the antenna, respectively. Since the formulation for the case of the magnetic wall is very similar to that of the electric wall, we will only give the formulation for the electric wall in the following.

Referring to Figure 2.2, the whole structure of interest is divided into $(N + 3)$ subregions: I, II, 1, 2, \dots , N and $N + 1$. Since the structure and the incident dominant TEM mode in the coaxial feed waveguide are axi-symmetric (no ϕ -variation), only three field components (E_z , E_ρ , and H_θ) are non-zero. The detailed expressions for the electromagnetic fields in all these regions are given in the next subsection.

2.2.2 Field Component Expressions

Starting with Maxwell's curl equations

$$\nabla \times \vec{H} = j\omega\epsilon\vec{E} \quad (2.8)$$

$$\nabla \times \vec{E} = -j\omega\mu\vec{H} \quad (2.9)$$

and using the relation $\frac{\partial}{\partial\phi} = 0$, one can derive the following expressions for three non-zero field components E_z , E_ρ , and H_θ .

$$E_\rho = \frac{-1}{j\omega\epsilon} \frac{\partial}{\partial z} H_\theta \quad (2.10)$$

$$E_z = \frac{1}{j\omega\epsilon} \frac{1}{\rho} \frac{\partial}{\partial\rho} (\rho H_\theta) \quad (2.11)$$

$$\frac{\partial^2 H_\theta}{\partial\rho^2} + \frac{1}{\rho} \frac{\partial H_\theta}{\partial\rho} + \frac{\partial^2 H_\theta}{\partial z^2} + (k^2 - \frac{1}{\rho^2}) H_\theta = 0. \quad (2.12)$$

It is noted that the $\exp(j\omega t)$ time dependence is assumed and suppressed for all the fields throughout this thesis. Based on these relations, one has no difficulty in finding the field expressions for all the subregions in Figure 2.2.

For the coaxial feed waveguide (Region I), the transverse electromagnetic fields with respect to the z -axis can be represented by

$$E_\rho^I = \sum_{n=1}^{N_I} [A_{Iin} \exp(\gamma_{In}(z - D)) + A_{Irn} \exp(-\gamma_{In}(z - D))] e_{In\rho} \quad (2.13)$$

$$H_\theta^I = \sum_{n=1}^{N_I} [-A_{Iin} \exp(\gamma_{In}(z - D)) + A_{Irn} \exp(-\gamma_{In}(z - D))] Y_{In} e_{In\rho} \quad (2.14)$$

where $\mathbf{A}_{Iin} = (A_{Ii1}, A_{Ii2}, \dots, A_{IiN_I})^T$ and $\mathbf{A}_{Irn} = (A_{Ir1}, A_{Ir2}, \dots, A_{IrN_I})^T$, with T representing the transpose operation, are the incident and reflected modal amplitude column vectors in the coaxial feed waveguide; $D = d + h + l + s$, $\gamma_{In} = j\beta_{In}$ and Y_{In} are, respectively, the propagation constant and modal admittance for the feed

line. N_I is the number of modes considered in the feed waveguide. The expressions for the normalized transverse modal electric field $e_{In\rho}$ and for the propagation constant γ_{In} and modal admittance Y_{In} of coaxial waveguide can be found in Appendix A.

In Region II, we have

$$E_z^{II} = \sum_{n=0}^{N_{II}} \frac{\epsilon_n A_n^{II}}{j\omega\epsilon_0\epsilon_r^{II}d} \cos \frac{n\pi z}{d} \frac{\gamma_n^{II} J_0(\gamma_n^{II}\rho)}{J_1(\gamma_n^{II}a_0)} \quad (2.15)$$

$$E_\rho^{II} = \sum_{n=1}^{N_{II}} \frac{\epsilon_n n\pi A_n^{II}}{j\omega\epsilon_0\epsilon_r^{II}d^2} \sin \frac{n\pi z}{d} \frac{J_1(\gamma_n^{II}\rho)}{J_1(\gamma_n^{II}a_0)} \quad (2.16)$$

$$H_\phi^{II} = \sum_{n=0}^{N_{II}} \frac{\epsilon_n A_n^{II}}{d} \cos \frac{n\pi z}{d} \frac{J_1(\gamma_n^{II}\rho)}{J_1(\gamma_n^{II}a_0)} \quad (2.17)$$

where $\epsilon_n = 1$ for $n = 0$; and $\epsilon_n = 2$ for $n > 0$, $(\gamma_n^{II})^2 = k_0^2\epsilon_r^{II} - (n\pi/d)^2$, J_0 and J_1 are the first kind Bessel functions of order 0 and 1, respectively. A_n^{II} is the expansion coefficient to be determined and $N_{II} + 1$ is the number of modes retained in Region II.

The expressions for the electromagnetic fields in Region 1 can be obtained by employing the resonator method [54], [55], which expresses the electromagnetic fields by superimposing three suitably chosen standing-wave solutions:

$$E_z^1 = \frac{1}{j\omega\epsilon_1} \left(\sum_{n=0}^{N_{11}} [U_{1n}(\rho)A_{1n} + V_{1n}(\rho)B_{1n}] \cos \frac{n\pi z}{D} + \sum_{n=1}^{N_{12}} C_{1n} e_{1nz}(\rho) \frac{\cos(\alpha_n z)}{\cos(\alpha_n D)} \right) \quad (2.18)$$

$$E_\rho^1 = \frac{-1}{j\omega\epsilon_1} \sum_{n=0}^{N_{11}} \frac{n\pi}{\gamma_{1n}^2 D} [U'_{1n}(\rho)A_{1n} + V'_{1n}(\rho)B_{1n}] \sin \frac{n\pi z}{D} + \frac{1}{j\omega\epsilon_1} \sum_{n=1}^{N_{12}} C_{1n} e_{1n\rho}(\rho) \frac{\alpha_n \sin(\alpha_n z)}{\cos(\alpha_n D)} \quad (2.19)$$

$$H_\phi^1 = \sum_{n=0}^{N_{11}} \frac{-1}{\gamma_{1n}^2} [U'_{1n}(\rho)A_{1n} + V'_{1n}(\rho)B_{1n}] \cos \frac{n\pi z}{D} + \sum_{n=1}^{N_{12}} C_{1n} e_{1n\rho}(\rho) \frac{\cos(\alpha_n z)}{\cos(\alpha_n D)} \quad (2.20)$$

where $\gamma_{1n}^2 = k_0^2 \epsilon_{r1} - (n\pi/D)^2$, $e_{1nz}(\rho)$ and $e_{1n\rho}(\rho)$ are the longitudinal and transverse electric-field components in a coaxial waveguide whose inner and outer radii are a_0 and a_1 , respectively; $\alpha_n = j\beta_{1n}$ is the propagation constant of this waveguide. Moreover,

$$U_{in}(\rho) = \frac{J_0(\gamma_{in}\rho)Y_0(\gamma_{in}a_{i-1}) - Y_0(\gamma_{in}\rho)J_0(\gamma_{in}a_{i-1})}{J_0(\gamma_{in}a_i)Y_0(\gamma_{in}a_{i-1}) - Y_0(\gamma_{in}a_i)J_0(\gamma_{in}a_{i-1})} \quad (2.21)$$

$$V_{in}(\rho) = -\frac{J_0(\gamma_{in}\rho)Y_0(\gamma_{in}a_i) - Y_0(\gamma_{in}\rho)J_0(\gamma_{in}a_i)}{J_0(\gamma_{in}a_i)Y_0(\gamma_{in}a_{i-1}) - Y_0(\gamma_{in}a_i)J_0(\gamma_{in}a_{i-1})} \quad (2.22)$$

for $i = 1, 2, \dots, N$. In (2.19) and (2.20) $U'_{1n}(\rho)$ and $V'_{1n}(\rho)$ indicate the derivative of $U_{1n}(\rho)$ and $V_{1n}(\rho)$ with respect to ρ .

Similarly, the electromagnetic fields in Region 2 are found as follows:

$$E_z^2 = \frac{1}{j\omega\epsilon_2} \sum_{n=0}^{N_2} [U_{2n}(\rho)A_{2n} + V_{2n}(\rho)B_{2n}] \cos \frac{n\pi z}{L} \quad (2.23)$$

$$E_\rho^2 = \frac{-1}{j\omega\epsilon_2} \sum_{n=0}^{N_2} \frac{n\pi}{\gamma_{2n}^2 L} [U'_{2n}(\rho)A_{2n} + V'_{2n}(\rho)B_{2n}] \sin \frac{n\pi z}{L} \quad (2.24)$$

$$H_\phi^2 = \sum_{n=0}^{N_2} \frac{-1}{\gamma_{2n}^2} [U'_{2n}(\rho)A_{2n} + V'_{2n}(\rho)B_{2n}] \cos \frac{n\pi z}{L} \quad (2.25)$$

with $L = d + h$, and

$$\gamma_{2n}^2 = k_0^2 \epsilon_{r2} - (n\pi/L)^2.$$

For Region i ($i = 3, 4, \dots, N$), we can get the following field component expressions:

$$E_z^i = \frac{1}{j\omega\epsilon_i} \sum_{n=0}^{N_3} [U_{in}(\rho)A_{in} + V_{in}(\rho)B_{in}] \cos \frac{n\pi z}{H} \quad (2.26)$$

$$E_\rho^i = \frac{-1}{j\omega\epsilon_i} \sum_{n=0}^{N_3} \frac{n\pi}{H\gamma_{in}^2} [U'_{in}(\rho)A_{in} + V'_{in}(\rho)B_{in}] \sin \frac{n\pi z}{H} \quad (2.27)$$

$$H_\phi^i = \sum_{n=0}^{N_3} \frac{-1}{\gamma_{in}^2} [U'_{in}(\rho)A_{in} + V'_{in}(\rho)B_{in}] \cos \frac{n\pi z}{H} \quad (2.28)$$

where $H = d + h + l$, $U_{in}(\rho)$ and $V_{in}(\rho)$ are defined in (2.21) and (2.22) with $\gamma_{in}^2 = k_0^2 \epsilon_{ri} - (n\pi/H)^2$ for $i = 3, 4, \dots, N$.

Finally, the electromagnetic field components in Region $N + 1$ can be found by taking the radiation condition at $\rho = \infty$ into account.

$$E_z^{N+1} = \frac{1}{j\omega\epsilon_{N+1}} \sum_{n=0}^{N_3} A_{(N+1)n} \frac{W_n(z)}{\epsilon_r(z)} \frac{H_0^{(2)}(\gamma_{(N+1)n}\rho)}{H_0^{(2)}(\gamma_{(N+1)n}a_N)} \quad (2.29)$$

$$E_\rho^{N+1} = \frac{-1}{j\omega\epsilon_{N+1}} \sum_{n=0}^{N_3} A_{(N+1)n} \frac{W'_n(z)}{\epsilon_r(z)} \frac{H_1^{(2)}(\gamma_{(N+1)n}\rho)}{\gamma_{(N+1)n} H_0^{(2)}(\gamma_{(N+1)n}a_N)} \quad (2.30)$$

$$H_\phi^{N+1} = \sum_{n=0}^{N_3} A_{(N+1)n} W_n(z) \frac{H_1^{(2)}(\gamma_{(N+1)n}\rho)}{\gamma_{(N+1)n} H_0^{(2)}(\gamma_{(N+1)n}a_N)} \quad (2.31)$$

where $H_0^{(2)}$ and $H_1^{(2)}$ are the outgoing second kind Hankel functions of order 0 and 1, respectively, and

$$W_n(z) = \begin{cases} \cos(k_{zn}^A z) \cos(k_{zn}^D t) / \cos(k_{zn}^A T), & T > z > 0 \\ \cos[k_{zn}^D (H - z)], & H > z > T \end{cases}$$

$$\epsilon_r(z) = \begin{cases} 1, & T > z > 0 \\ \epsilon_{rs}, & H > z > T \end{cases}$$

and $T = H - t$. k_{zn}^A and k_{zn}^D can be found by solving the following transcendental equation

$$k_{zn}^A \tan(k_{zn}^A T) = -\frac{k_{zn}^D}{\epsilon_{rs}} \tan(k_{zn}^D t)$$

with $\gamma_{(N+1)n}^2 = k_0^2 \epsilon_{(N+1)r} - (k_{zn}^A)^2 = k_0^2 \epsilon_{(N+1)r} \epsilon_{rs} - (k_{zn}^D)^2$. After having found all the field expressions for subregions $I, II, 1, 2, \dots, N$, and $N + 1$, boundary conditions at conducting surfaces and regional interfaces will be invoked to determine the unknown expansion coefficients in the next subsection.

2.2.3 Application of Boundary Conditions

Application of the boundary conditions that the tangential electromagnetic fields must be continuous at the interface $\rho = a_N$ results in

$$\mathbf{A}_{N+1} = \mathbf{K}_A \mathbf{A}_N \quad (2.32)$$

$$\mathbf{D}_A \mathbf{A}_N + \mathbf{D}_B \mathbf{B}_N = \mathbf{Z}^T \mathbf{Y}_{N+1} \mathbf{A}_{N+1} \quad (2.33)$$

where

$$K_{A,mn} = \frac{\epsilon_{N+1}}{N_{sn} \epsilon_N} Z_{mn} U_{Nn}(a_N)$$

$$Z_{mn} = \int_0^H W_m(z) \cos \frac{n\pi z}{H} dz$$

$$D_{A,mn} = \frac{-H U'_{Nn}(a_N) \delta_{nm}}{\epsilon_n \gamma_{Nn}^2}, \quad D_{B,mn} = \frac{-H V'_{Nn}(a_N) \delta_{nm}}{\epsilon_n \gamma_{Nn}^2}$$

$$Y_{(N+1)n} = \frac{H_1^{(2)}(\gamma_{(N+1)n} a_N)}{\gamma_{(N+1)n} H_0^{(2)}(\gamma_{(N+1)n} a_N)}$$

$$N_{sn} = \frac{t}{2\epsilon_{rs}} + \frac{L \cos^2(k_{zn}^D t)}{2 \cos^2(k_{zn}^A L)} + \frac{k^2(1 - \epsilon_{rs}) \sin(2k_{zn}^D t)}{4\epsilon_{rs} (k_{zn}^A)^2 k_{zn}^D}$$

and $\delta_{nm} = 1$ for $n = m$; $\delta_{nm} = 0$ for $n \neq m$ and $\epsilon_n = 1$ for $n = 1$; $\epsilon_n = 2$ for $n > 1$.

From (2.32) and (2.33), we get

$$\mathbf{B}_N = \mathbf{\Gamma}_N \mathbf{A}_N \quad (2.34)$$

where

$$\mathbf{\Gamma}_N = \mathbf{D}_B^{-1} (\mathbf{Z}^T \mathbf{Y}_{N+1} \mathbf{K}_A - \mathbf{D}_A).$$

Enforcement of the continuity conditions of tangential electromagnetic fields at the interface $\rho = a_i$ ($i = 3, 4, \dots, N-1$) leads to

$$\frac{A_{in}}{\epsilon_i} = \frac{B_{(i+1)n}}{\epsilon_{i+1}} \quad (2.35)$$

$$-\frac{U'_{in}(a_i)}{\gamma_{in}^2}A_{in} - \frac{V'_{in}(a_i)}{\gamma_{in}^2}B_{in} = -\frac{U'_{(i+1)n}}{\gamma_{(i+1)n}^2}A_{(i+1)n} - \frac{V'_{(i+1)n}}{\gamma_{(i+1)n}^2}B_{(i+1)n} \quad (2.36)$$

or

$$\begin{bmatrix} A_{in} \\ B_{in} \end{bmatrix} = \mathbf{T}_i \begin{bmatrix} A_{(i+1)n} \\ B_{(i+1)n} \end{bmatrix} \quad (2.37)$$

where

$$\mathbf{T}_i = \begin{bmatrix} 0 & \epsilon_i/\epsilon_{i+1} \\ \frac{\gamma_{in}^2 U'_{(i+1)n}(a_i)}{\gamma_{(i+1)n}^2 V'_{in}(a_i)} & \frac{\gamma_{in}^2 V'_{(i+1)n}(a_i)}{\gamma_{(i+1)n}^2 V'_{in}(a_i)} - \frac{\epsilon_i U'_{in}(a_i)}{\epsilon_{i+1} V'_{in}(a_i)} \end{bmatrix}. \quad (2.38)$$

Equation (2.37) provides a recursive relation of the electromagnetic fields between two adjacent dielectric regions.

Repeatedly using (2.37), we can obtain the following relation

$$\begin{bmatrix} A_{3n} \\ B_{3n} \end{bmatrix} = \mathbf{T}^t \begin{bmatrix} A_{Nn} \\ B_{Nn} \end{bmatrix} = \begin{bmatrix} T_{11}^t & T_{12}^t \\ T_{21}^t & T_{22}^t \end{bmatrix} \begin{bmatrix} A_{Nn} \\ B_{Nn} \end{bmatrix} \quad (2.39)$$

where

$$\mathbf{T}^t = \mathbf{T}_3 \mathbf{T}_4 \cdots \mathbf{T}_{N-1}.$$

Combining (2.34) and (2.39) yields

$$\mathbf{A}_3 = \mathbf{\Gamma}_3 \mathbf{B}_3 \quad (2.40)$$

where

$$\mathbf{\Gamma}_3 = \mathbf{R}_A \mathbf{R}_B^{-1}$$

with

$$R_{A,mn} = T_{11n}^t \delta_{mn} + T_{12m}^t \Gamma_{N,mn}$$

$$R_{B,mn} = T_{21n}^t \delta_{mn} + T_{22m}^t \Gamma_{N,mn}.$$

Application of the boundary conditions that the tangential electromagnetic field components must be continuous at the interfaces $\rho = a_0$, $\rho = a_1$, $\rho = a_2$ and $z = D$ yields

$$\frac{1}{j\omega\epsilon_1} \sum_{n=0}^{N_{11}} B_{1n} \cos \frac{n\pi z}{D} = \begin{cases} \sum_{n=0}^{N_{11}} \frac{\epsilon_n A_n^{II}}{j\omega\epsilon_0 \epsilon_1^{II} d} \cos \frac{n\pi z}{d} \frac{\gamma_n^{II} J_0(\gamma_n^{II} a_0)}{J_1(\gamma_n^{II} a_0)}, & 0 < z < d \\ 0, & d < z < D \end{cases} \quad (2.41)$$

$$\begin{aligned} \sum_{n=0}^{N_{11}} \frac{\epsilon_n A_n^{II}}{d} \cos \frac{n\pi z}{d} &= \sum_{n=0}^{N_{11}} \frac{-1}{\gamma_{1n}^2} [U'_{1n}(a_0)A_{1n} + V'_{1n}(a_0)B_{1n}] \cos \frac{n\pi z}{D} \\ &+ \sum_{n=1}^{N_{12}} C_{1n} e_{1n\rho}(a_0) \frac{\cos(\alpha_n z)}{\cos(\alpha_n D)}, \quad 0 < z < d \end{aligned} \quad (2.42)$$

$$\frac{1}{j\omega\epsilon_1} \sum_{n=0}^{N_{11}} A_{1n} \cos \frac{n\pi z}{D} = \begin{cases} \frac{1}{j\omega\epsilon_2} \sum_{n=0}^{N_2} B_{2n} \cos \frac{n\pi z}{L}, & 0 < z < L \\ 0, & L < z < D \end{cases} \quad (2.43)$$

$$\begin{aligned} \sum_{n=0}^{N_2} \frac{-1}{\gamma_{2n}^2} [U'_{2n}(a_1)A_{2n} + V'_{2n}(a_1)B_{2n}] \cos \frac{n\pi z}{L} &= \sum_{n=0}^{N_{11}} \frac{-1}{\gamma_{1n}^2} [U'_{1n}(a_1)A_{1n} \\ &+ V'_{1n}(a_0)B_{1n}] \cos \frac{n\pi z}{D} + \sum_{n=1}^{N_{12}} C_{1n} e_{1n\rho}(a_1) \frac{\cos(\alpha_n z)}{\cos(\alpha_n D)}, \quad 0 < z < L \end{aligned} \quad (2.44)$$

$$\frac{1}{j\omega\epsilon_3} \sum_{n=0}^{N_3} B_{3n} \cos \frac{n\pi z}{H} = \begin{cases} \frac{1}{j\omega\epsilon_2} \sum_{n=0}^{N_2} A_{2n} \cos \frac{n\pi z}{L}, & 0 < z < L \\ 0, & L < z < H \end{cases} \quad (2.45)$$

$$\begin{aligned} \sum_{n=0}^{N_2} \frac{-1}{\gamma_{2n}^2} [U'_{2n}(a_2)A_{2n} + V'_{2n}(a_2)B_{2n}] \cos \frac{n\pi z}{L} \\ = \sum_{n=0}^{N_3} \frac{-1}{\gamma_{3n}^2} [U'_{3n}(a_2)A_{3n} + V'_{3n}(a_2)B_{3n}] \cos \frac{n\pi z}{H}, \quad 0 < z < L \end{aligned} \quad (2.46)$$

$$\sum_{n=1}^{N_{12}} \frac{\alpha_n \tan(\alpha_n D)}{j\omega\epsilon_1} C_{1n} e_{1nz}(\rho) = \begin{cases} \sum_{n=1}^{N_I} (A_{Iin} + A_{Irn}) e_{In\rho}(\rho), & a_I < \rho < b_I \\ 0, & \text{elsewhere} \end{cases} \quad (2.47)$$

$$\sum_{n=1}^{N_I} (-A_{Iin} + A_{Irn}) Y_{In} e_{In\rho} = \sum_{n=0}^{N_{11}} \frac{(-1)^{n+1}}{\gamma_{1n}^2} [U'_{1n}(\rho)A_{1n}$$

$$+ V'_{1n}(\rho)B_{1n}] + \sum_{n=1}^{N_{12}} C_{1n}e_{1n\rho}(\rho), \quad a_I < \rho < b_I \quad (2.48)$$

From the above equations, we can derive the following matrix equations:

$$\mathbf{B}_1 = \mathbf{P}_B \mathbf{A}^{II} \quad (2.49)$$

$$\mathbf{A}^{II} = \mathbf{M}_{IIA} \mathbf{A}_1 + \mathbf{M}_{IIB} \mathbf{B}_1 + \mathbf{M}_{IIC} \mathbf{C}_1 \quad (2.50)$$

$$\mathbf{A}_1 = \mathbf{P}_A \mathbf{B}_2 \quad (2.51)$$

$$\mathbf{Y}_{1A} \mathbf{A}_2 + \mathbf{Y}_{1B} \mathbf{B}_2 = \mathbf{M}_{2A} \mathbf{A}_1 + \mathbf{M}_{2B} \mathbf{B}_1 + \mathbf{M}_{2C} \mathbf{C}_1 \quad (2.52)$$

$$\mathbf{B}_3 = \mathbf{P}_D \mathbf{A}_2 \quad (2.53)$$

$$\mathbf{Y}_{3A} \mathbf{A}_2 + \mathbf{Y}_{3B} \mathbf{B}_2 = \mathbf{M}_{3A} \mathbf{A}_3 + \mathbf{M}_{3B} \mathbf{B}_3 \quad (2.54)$$

$$\mathbf{C}_1 = \mathbf{P}_C (\mathbf{A}_{Ii} + \mathbf{A}_{Ir}) \quad (2.55)$$

$$\mathbf{Y}_I (\mathbf{A}_{Ii} - \mathbf{A}_{Ir}) = \mathbf{M}_{IA} \mathbf{A}_1 + \mathbf{M}_{IB} \mathbf{B}_1 + \mathbf{M}_{IC} \mathbf{C}_1 \quad (2.56)$$

where the elements of all the above matrices are elucidated in Appendix C.

After some manipulations one has no difficulty in arriving at

$$\mathbf{A}_{Ir} = \mathbf{S}_{I11} \mathbf{A}_{Ii} = [2(\mathbf{I} - \mathbf{Y}_I^{-1} \mathbf{Y}_{LI})^{-1} - \mathbf{I}] \mathbf{A}_{Ii} \quad (2.57)$$

where

$$\mathbf{Y}_{LI} = [(\mathbf{M}_{IA} + \mathbf{M}_{IB} \mathbf{W} \mathbf{M}_{IIA}) \mathbf{S} + \mathbf{M}_{IB} \mathbf{W} \mathbf{M}_{IIC} + \mathbf{M}_{IC}] \mathbf{P}_C$$

$$\mathbf{S} = \mathbf{P}_A \mathbf{Q} \mathbf{V} (\mathbf{M}_{2C} + \mathbf{M}_{2B} \mathbf{W} \mathbf{M}_{IIC}).$$

$$\mathbf{V} = [\mathbf{Y}_{1A} + \mathbf{Y}_{1B} \mathbf{Q} - (\mathbf{M}_{2A} + \mathbf{M}_{2B} \mathbf{W} \mathbf{M}_{IIA}) \mathbf{P}_A \mathbf{Q}]^{-1}$$

$$\mathbf{W} = \mathbf{P}_B (\mathbf{I} - \mathbf{M}_{IIB} \mathbf{P}_B)^{-1}$$

$$\mathbf{Q} = \mathbf{Y}_{3B}^{-1} [-\mathbf{Y}_{3A} + (\mathbf{M}_{3A} \mathbf{\Gamma}_3 + \mathbf{M}_{3B}) \mathbf{P}_D]$$

Equation (2.57) can be used to calculate the reflected modal amplitude vector \mathbf{A}_{I_r} for both the dominant TEM mode and higher order modes in the coaxial-feed waveguide assuming that the incident modal column vector \mathbf{A}_{I_i} is known [for example, $(1, 0, \dots, 0)^T$]. Other expansion coefficients A_n^{II} , A_{1n} , B_{1n} , C_{1n} , A_{in} and B_{in} , for $i = 2, 3, \dots, N$, can be calculated from (2.49)-(2.56).

It should be pointed out that these Bessel and Hankel functions used above should be replaced by their corresponding modified Bessel functions when their arguments become imaginary; specifically, $J_0(\gamma_n^{II}\rho)$ is replaced by $I_0(\gamma_n^{II}\rho)$ when $(\gamma_n^{II})^2 < 0$; $Y_0(\gamma_{1n}\rho)$ will be replaced by $K_0(\gamma_{1n}\rho)$ when $\gamma_{1n}^2 < 0$; and $H_0^{(2)}(\gamma_{(N+1)n}\rho)$ will be replaced by $K_0(\gamma_{(N+1)n}\rho)$ when $\gamma_{(N+1)n}^2 < 0$, and the like. Here, I_0 and K_0 are the zeroth-order modified Bessel functions [56] of the first kind and the second kind, respectively.

From (2.57) one can extract the reflection coefficient S_{I11}^e for the dominant TEM mode in the coaxial-feed waveguide when an electric wall is at a height of d over the end of the monopole. Following the procedure described above, one can obtain the reflection coefficient S_{I11}^m with a magnetic wall over the top of the monopole. The final reflection coefficient Γ_{in} for the incident TEM mode in the feed line of the monopole antenna is then calculated from (2.7). The input impedance of the monopole antenna is defined as

$$Z_{in} = Z_{I0} \frac{1 + \Gamma_{in}}{1 - \Gamma_{in}} \quad (2.58)$$

where Z_{I0} is the impedance of the TEM mode in the coaxial waveguide (Region I).

Once all the expansion coefficients in (2.13)-(2.31) are known, the surface currents on both the monopole and the sleeve can be found by summing the tangential

magnetic field series. For the current on the monopole, from (2.20) we have

$$I_m(z) = 2\pi a_0 \sum_{n=0}^{N_{11}} \frac{-1}{\gamma_{1n}^2} [U'_{1n}(a_0)A_{1n} + V'_{1n}(a_0)B_{1n}] \cos \frac{n\pi z}{D} \\ + 2\pi a_0 \sum_{n=1}^{N_{12}} C_{1n} e_{1n\rho}(a_0) \frac{\cos(\alpha_n z)}{\cos(\alpha_n D)} \quad (2.59)$$

where $d < z < L$. For the current on the sleeve, from (2.28) we obtain

$$I_s(z) = 2\pi a_2 \sum_{n=0}^{N_3} \frac{-1}{\gamma_{3n}^2} [U'_{3n}(a_2)A_{3n} + V'_{3n}(a_2)B_{3n}] \cos \frac{n\pi z}{H} \quad (2.60)$$

where $L < z < L + l$.

Radial ρ -directed currents also flow in the end surfaces of the sleeve at $z = L$ and of the monopole at $z = d$; they have the following forms:

$$J_\rho(\rho) = \sum_{n=0}^{N_2} \frac{2\pi(-1)^{n+1}}{\gamma_{2n}^2} [U'_{2n}(\rho)A_{2n} + V'_{2n}(\rho)B_{2n}] \quad (2.61)$$

for $a_2 > \rho > a_1$ at $z = d + h$ and

$$J_\rho(\rho) = 2\pi \sum_{n=0}^{N_{II}} A_n^{II} (-1)^n \frac{\epsilon_n J_1(\gamma_n^{II} \rho)}{d J_1(\gamma_n^{II} a_0)} \quad (2.62)$$

for $a_0 > \rho > 0$ at $z = d$.

2.2.4 Far-Field Radiation Pattern

After the field components and current distributions on the antenna are found, it is possible to compute the far-region radiation pattern of the monopole antenna. In order to make the derivation simple, this subsection only considers the calculation of the far-field radiation pattern of the sleeve monopole antenna, which is shown in Figure 2.3. The radiation pattern for the conventional monopole antenna can be simply computed by letting the sleeve length be zero in the following formulas. For

this sleeve monopole, we have $a_0 = a_I$, $b_I = a_1$ and there are only 4 subregions: I , II , 1, and 2. The field components for Regions I , II , and 1 are defined by (2.13) to (2.20) with $D = h + d = L$. The field expressions for Region 2 are given by

$$E_{2z} = \frac{1}{j\omega\epsilon_2} \sum_{n=0}^{N_2} \frac{\epsilon_n A_{2n}}{H} \cos \frac{n\pi z}{H} \frac{H_0^{(2)}(\gamma_{2n}\rho)}{H_0^{(2)}(\gamma_{2n}a_2)} \quad (2.63)$$

$$E_{2\rho} = \frac{1}{j\omega\epsilon_2} \sum_{n=0}^{N_2} \frac{n\pi\epsilon_n A_{2n}}{H^2} \sin \frac{n\pi z}{H} \frac{H_1^{(2)}(\gamma_{2n}\rho)}{\gamma_{2n}H_0^{(2)}(\gamma_{2n}a_2)} \quad (2.64)$$

$$H_{2\phi} = \sum_{n=0}^{N_2} \frac{\epsilon_n A_{2n}}{H} \cos \frac{n\pi z}{H} \frac{H_1^{(2)}(\gamma_{2n}\rho)}{\gamma_{2n}H_0^{(2)}(\gamma_{2n}a_2)} \quad (2.65)$$

where $\gamma_{2n}^2 = k^2 - (n\pi/H)^2$ with $H = L + l$.

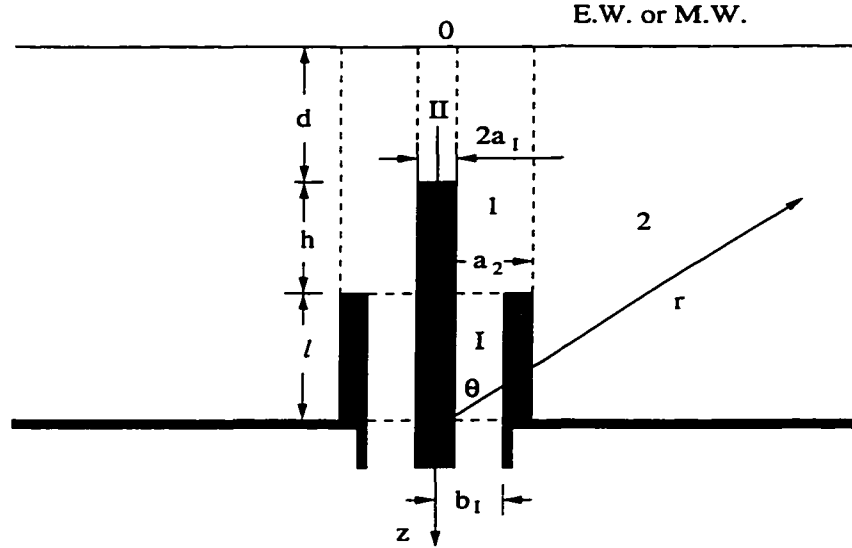


Figure 2.3: Geometry of a sleeve monopole antenna.

To calculate the far-region radiated field pattern, the method of images is initially employed to transform the sleeve monopole into a sleeve dipole. Then the far-zone radiated fields can be evaluated by Green's function integrations [57] over the outer surfaces of the sleeve dipole. There are three distinct current contributions to the radiated fields: 1) physical electric currents on the cylindrical surfaces of

both the monopole ($\rho = a_0 = a_I, d < z < L$) and the sleeve ($\rho = a_2, L < z < L+l$), 2) physical electric currents on the end surfaces of both the monopole ($0 < \rho < a_I, z = d$) and the sleeve ($b_I = a_1 < \rho < a_2, z = L$), and 3) equivalent electric and magnetic currents on the aperture surface of the feed line ($a_I < \rho < b_I, z = L$). For most practical applications, the monopole is thin and the thickness of the sleeve is relatively small compared to the wavelength of operation. Therefore, the far-zone radiated pattern is mainly determined by the first part.

The far-zone radiated electric field due to physical electric current can be calculated as follows [57]

$$\vec{E}_J = \frac{-j\omega\mu}{4\pi} \int \int_S \vec{J}(\rho', \phi') \frac{\exp(-jk_0 R)}{R} ds' \quad (2.66)$$

where $R = r - \rho' \sin \theta \cos(\phi - \phi')$, and $\vec{J}(\rho', \phi') = \hat{n} \times \vec{H}(\rho', \phi')$ on the conductor surface. Similarly the radiated electric field in the far-region due to the equivalent magnetic current is computed by

$$\vec{E}_M = \frac{jk_0}{4\pi} \int \int_S [\hat{r} \times \vec{M}(\rho', \phi')] \frac{\exp(-jk_0 R)}{R} ds' \quad (2.67)$$

where $\vec{M}(\rho', \phi') = \vec{E}(\rho', \phi') \times \hat{n}$ on the aperture surface. These expressions are employed to derive the following components for the far-zone electric field.

The θ -directed electric field component E_{θ_1} in the far-zone due to the physical-electric current on the cylindrical surface of the monopole is

$$\begin{aligned} E_{\theta_1}(\theta) = & \frac{j\omega\mu e^{-jk_0 r}}{r} a_I \sin \theta J_0(k_0 a_I \sin \theta) \sum_{n=0}^{N_{11}} [U'_{1n}(a_I) A_{1n} + V'_{1n}(a_I) B_{1n}] I_{1n}(\theta) \\ & + \frac{j\omega\mu e^{-jk_0 r}}{r} a_I \sin \theta J_0(k_0 a_I \sin \theta) \sum_{n=1}^{N_{12}} C_{1n} I_{2n}(\theta) \end{aligned} \quad (2.68)$$

where

$$I_{1n}(\theta) = \frac{-1}{\gamma_{1n}^2} \int_l^{h+l} \cos \frac{n\pi(L+l-z')}{L} \cos(k_0 z' \cos \theta) dz'$$

$$I_{2n}(\theta) = \frac{e_{1n\rho}(a_I)}{\cos(\alpha_n D)} \int_l^{h+l} \cos[\alpha_n(L+l-z')] \cos(k_0 z' \cos \theta) dz'$$

and $z' = L + l - z$. It should be mentioned that the relation

$$\int_0^{2\pi} \exp[jk_0 a_I \sin \theta \cos(\phi - \phi')] d\phi' = 2\pi J_0(k_0 a_I \sin \theta)$$

is employed to derive (2.68).

The radiated electric field $E_{\theta 2}$ due to the physical electric current on the cylindrical surface of the sleeve has the form of

$$E_{\theta 2}(\theta) = \frac{j\omega\mu e^{-jk_0 r}}{r} a_2 \sin \theta J_0(k_0 a_2 \sin \theta) \sum_{n=0}^{N_2} \frac{\epsilon_n A_{2n}}{H} \frac{H_1^{(2)}(\gamma_{2n} a_2)}{\gamma_{2n} H_0^{(2)}(\gamma_{2n} a_2)} I_{3n}(\theta) \quad (2.69)$$

where

$$I_{3n}(\theta) = \int_0^l \cos \frac{n\pi(H-z')}{H} \cos(k_0 z' \cos \theta) dz'$$

The far-zone electric field $E_{\theta 3}$ due to the physical electric current in the end surface of the monopole can be calculated as follows:

$$E_{\theta 3}(\theta) = \frac{-j\omega\mu e^{-jk_0 r}}{r} \cos \theta \sin[k_0(h+l) \cos \theta] \sum_0^{N_{II}} \frac{(-1)^n \epsilon_n A_n^{II}}{dJ_1(\gamma_n^{II} a_0)} I_{4n}(\theta) \quad (2.70)$$

where

$$I_{4n}(\theta) = \int_0^{a_I} J_1(\gamma_n^{II} \rho') J_1(k_0 \rho' \sin \theta) \rho' d\rho'$$

Similarly, the θ -directed electric field $E_{\theta 4}$ generated by both the physical electric current on the end surface of the sleeve and the equivalent electric current on the aperture of the coaxial feed line is

$$E_{\theta 4}(\theta) = \frac{-j\omega\mu e^{-jk_0 r}}{r} \cos \theta \sin(k_0 l \cos \theta) \left[\sum_{n=0}^{N_{11}} \frac{(-1)^{n+1}}{\gamma_{1n}^2} I_{5n}(\theta) + \sum_{n=1}^{N_{12}} C_{1n} I_{6n}(\theta) \right] \quad (2.71)$$

where

$$I_{5n}(\theta) = \int_{a_I}^{a_2} [U'_{1n}(\rho') A_{1n} + V'_{1n}(\rho') B_{1n}] J_1(k_0 \rho' \sin \theta) \rho' d\rho$$

$$I_{6n}(\theta) = \int_{a_I}^{a_2} e_{1n\rho}(\rho') J_1(k_0 \rho' \sin \theta) \rho' d\rho'.$$

The far-region electric field component $E_{\theta 5}$ generated by the equivalent magnetic current on the aperture is

$$E_{\theta 5}(\theta) = \frac{j k_0 e^{-j k_0 r}}{r} \cos(k_0 l \cos \theta) \sum_{n=1}^{N_I} (A_{Iin} + A_{Irn}) \int_{a_I}^{b_I} e_{In\rho}(\rho') J_1(k_0 \rho' \sin \theta) \rho' d\rho'. \quad (2.72)$$

Finally, the total far-zone radiated field pattern $|r E_{\theta}(\theta)|$ can be computed by summing all the above components

$$|r E_{\theta}(\theta)| = |r E_{\theta 1}(\theta) + r E_{\theta 2}(\theta) + r E_{\theta 3}(\theta) + r E_{\theta 4}(\theta) + r E_{\theta 5}(\theta)|. \quad (2.73)$$

Radiated power pattern can be easily calculated by squaring the above expression.

2.3 Conclusions

A unified mathematical formulation has been presented in this chapter. The rigorous treatment of a general monopole problem has been realized by introducing a PMB (a combination of an electric wall and a magnetic wall) over the monopole antenna. The electromagnetic field components in all the regions of the resulting structure are expressed as the summation of its modal functions weighted by unknown coefficients. Expansion coefficients are then determined by enforcing the boundary conditions at the conducting surfaces and regional interfaces. This analysis is valid for both thin and thick monopoles, while most previously reported methods are only valid for the case of thin monopoles. The formulation presented can also take the feed line and the finite thickness of the sleeve and the insulating layer into account. Numerical results for various monopole structures will be given in the next chapter.

Chapter 3

Numerical Results for Monopole Antennas

This chapter is devoted to numerical results and discussions for various monopole antennas. It is comprised of five sections; each of them deals with one monopole antenna structure. Considered in this chapter are the conventional monopole antenna, the sleeve monopole, dielectric-coated and -buried monopoles, a multilayer insulated monopole, and a monopole over a finite ground plane. The general formulation for all these structures except the last one is described in the previous chapter. In the last section, a waveguide junction cascading formulation is briefly presented to calculate the input impedance of a monopole over a finite ground plane of arbitrary thickness. For all these examples we will consider, our computed results shall be compared with available theoretical or experimental data in the literature. Very good agreement can be observed. Numerical convergence and effect of the assumed PMB on the performance parameters of each antenna structure are initially examined, but only a few will be given below. Extensive computed results

are given to show the junction effect, end effect, and finite thickness influence on all these antennas' input impedances and radiation patterns.

3.1 Conventional Monopole Antennas

In this section, we will study the conventional monopole antenna with emphasis on the junction effect at the feed point of the monopole [58]. The structure of the conventional monopole is shown in Figure 3.1, where the monopole is actually the extended inner conductor of the coaxial feed line over the ground plane.

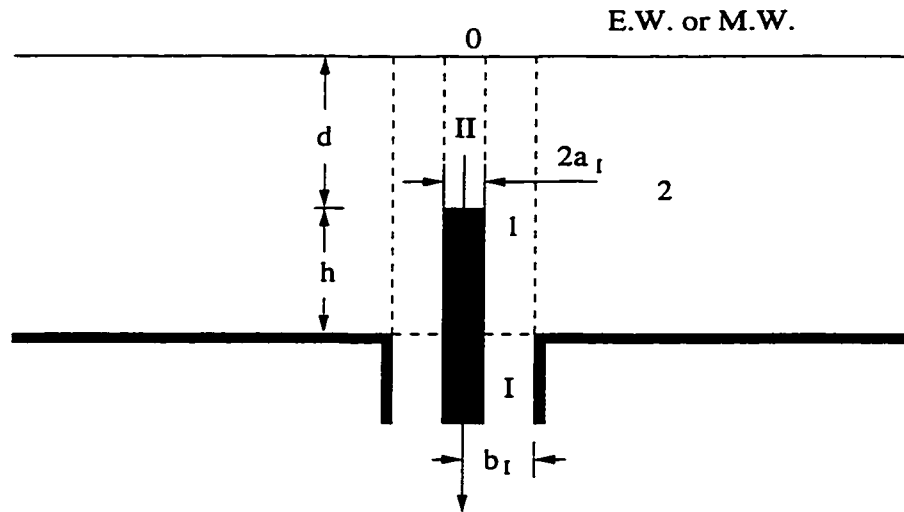


Figure 3.1: Geometry of a conventional monopole antenna.

First, the convergence behavior of the impedance with respect to the truncation numbers N_I and N_{II} is checked. Following the well-known convergence criterion for the mode-matching method [59], we choose $N_I = N_{II}(1 + d/h)$ for properly convergent results. Table 3.1 shows the convergence of the input impedance of a monopole with respect to the number of modes N_I considered in the coaxial-feed

waveguide. It is seen that the result obtained by taking only the dominant TEM mode into account is quite good. This phenomenon is due to the relatively small electrical dimensions of the coaxial-feed waveguide. Table 3.2 gives the convergence characteristic of the input impedance of the same antenna with respect to N_{II} . We see that $N_{II} = 80$ is enough to get a convergent result for the antenna's impedance. It should be mentioned here that the value of N_{II} varies with the distance d , as expected. The bigger the distance d , the larger the number N_{II} would be. The results given in Table 3.2 are obtained for $d = \sqrt{2}\lambda_0$, which will be shown later to be large enough to get very good results. The choice of $N_I = 2$ and $N_{II} = 80$ is adopted in the later computations.

Table 3.1: Convergence of the admittance (Millimhos) of a quarter-wavelength monopole with respect to N_I ($a_I = 0.05985\lambda_0$, $b_I = 1.187a_I$).

N_I	Conductance	Susceptance
1	19.4	6.4
2	19.4	6.3
5	19.4	6.3

The effect of the important parameter d on the monopole's admittance is examined in Figure 3.2, where the height of the monopole is a quarter of a wavelength. The assertion that the assumed PMB does not have much influence on the admittance of the monopole antenna is affirmed. From Figure 3.2, we note that the effect of the introduced PMB is negligible when the distance d is more than $1.3\lambda_0$. The choice of $d = \sqrt{2}\lambda_0$ is used in what follows.

Table 3.2: Convergence of the admittance (Millimhos) of a quarter-wavelength monopole with respect to N_{II} ($a_I = 0.05985\lambda_0$, $b_I = 1.187a_I$).

N_{II}	Conductance	Susceptance
5	14.8	26.0
10	18.9	12.5
20	19.2	8.4
40	19.4	6.8
80	19.4	6.3
160	19.5	6.2

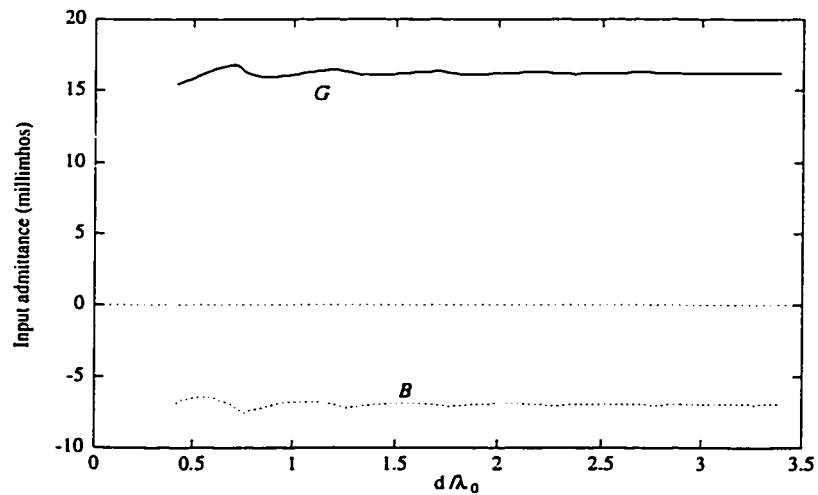


Figure 3.2: Variation of the input admittance of a monopole with respect to the distance d from the assumed PMB to the end of the monopole ($k_0a_I = 0.05985$).

3.1.1 Comparison with Others' Data

Numerical results for the surface current distribution over a monopole antenna and the input admittance of the monopole antenna, obtained by our modal-expansion method, are shown in Figures 3.3 and 3.4, respectively. Also given in these figures are the results obtained by King [4]. It can be seen that the agreement between our modal expansion results and King's accurate data is excellent. It should be noted that our modal expansion method applies to both thin and thick monopole antennas. Moreover, the modal expansion formulation presented in the previous chapter can characterize the effect of the junction between the monopole antenna and its feed line, which will be studied in the next subsection.

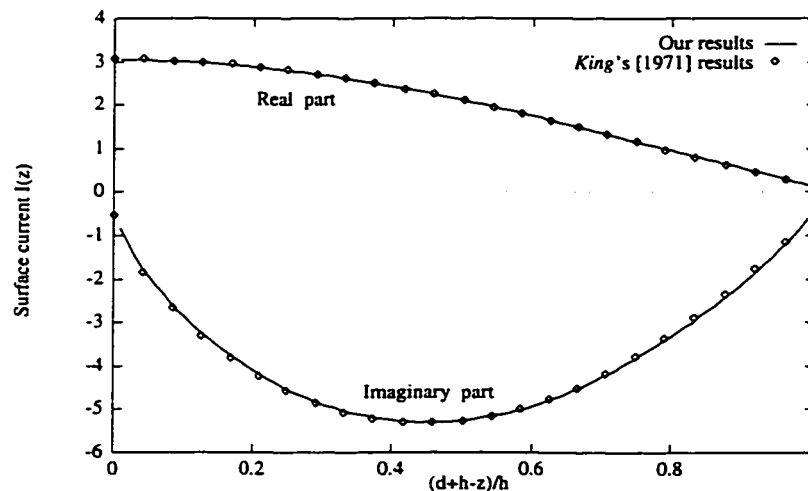


Figure 3.3: Surface current on a monopole antenna ($k_0 a_I = 0.04412$, $k_0 h = 0.75\pi$).

Radiated field pattern of a quarter-wavelength monopole antenna is shown in Figure 3.5. Also plotted in the figure are the measured results in [4]. Very good agreement between our computed results and experimental data is observed. It is seen that the main radiation occurs in the horizontal direction, while the radiation is null in the vertical direction where the electric and magnetic walls are placed.

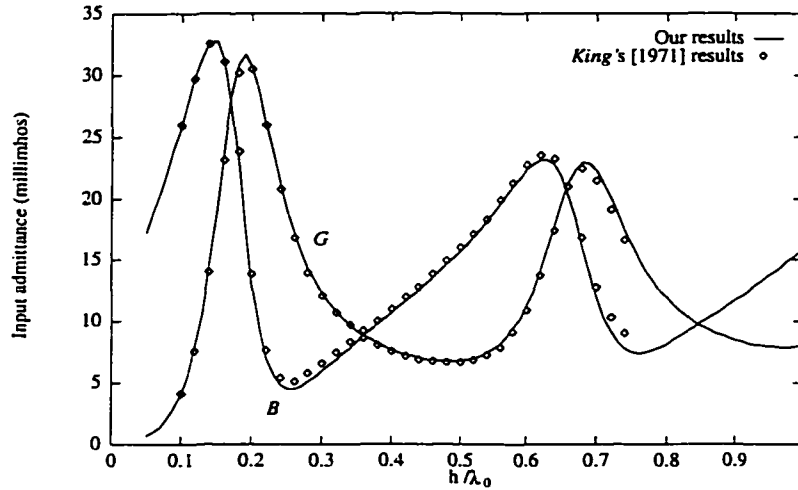


Figure 3.4: Input admittance of a monopole fed through an infinite ground plane by a coaxial line ($a_I = 0.0509\lambda_0$).

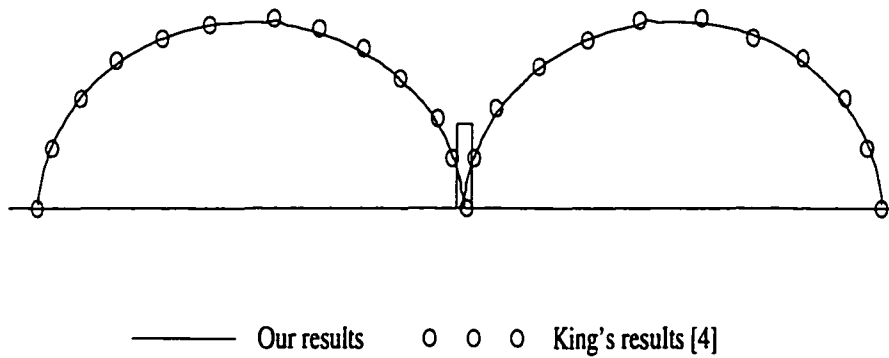


Figure 3.5: Radiated field pattern of a quarter-wavelength monopole antenna ($a_I = 0.0509\lambda_0$).

3.1.2 Junction Effects

This subsection studies the effect of the junction between the monopole antenna and the feed coaxial line. There are three different types for the connection of a monopole and its feed line, as illustrated in Figure 3.6; they will be individually studied in the following.

For the first type of junction (Figure 3.6(a)), there is a simple radial step junction between the monopole and the feed line. Numerical results for the input impedance ($R + jX$) of this type of monopole antenna are given in Figure 3.7, where the measured results by Hartig [60] for the same monopole antenna with a hemispherical cap are also shown for comparison. A small difference in their resonant lengths is observed. Our resonant length for the monopole with a flat end is a little shorter than that with a hemispherical cap, which is expected.

We also wish to examine the effect of the junction between the feed line and the monopole on the input admittance of the monopole antenna. Figure 3.8 gives the input admittance of a monopole antenna for different radii of the inner conductor of the feed line, while the radius of the monopole is fixed. It is seen that the junction between the feed line and the monopole has a significant influence on the imaginary part (susceptance B) of the admittance, while it has little effect on the real part (conductance G). The step junction provides a parallel capacitance or positive susceptance at the base of the monopole, which shifts the curve of input susceptance upward when the junction step increases.

The parallel capacitance generated by a step discontinuity in the inner conductor of a coaxial line is given by the following simple formula [61]:

$$C_s = 2b_I \left[\epsilon_0 \frac{\alpha^2 + 1}{\alpha} \ln \frac{1 + \alpha}{1 - \alpha} - 2\epsilon_0 \ln \frac{4\alpha}{1 - \alpha^2} + 3.487 \times 10^{-13} (1 - \alpha)(b_I/a_I - 1) \right] \quad (3.1)$$

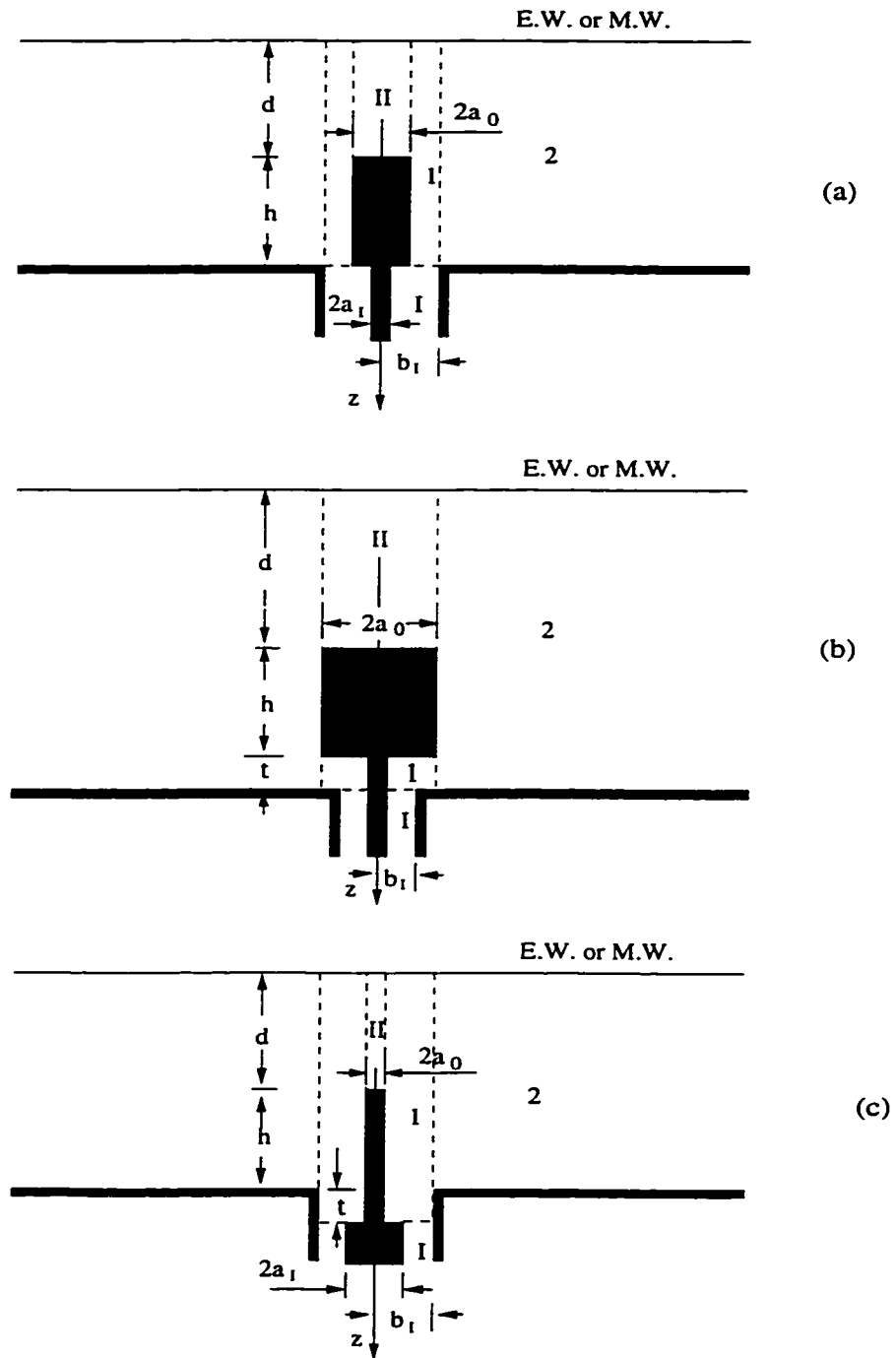


Figure 3.6: Three types of junction between the monopole and the feed line.

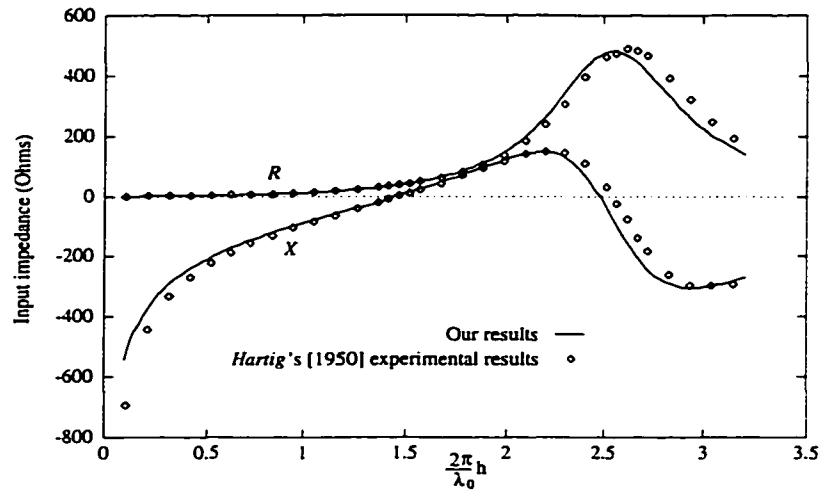


Figure 3.7: Input impedance of a monopole antenna shown in Figure 3.6(a) ($a_0 = 0.00397\lambda_0$, $a_0 = 1.33a_I$, $b_I = 1.67a_0$).

where $\alpha = (b_I - a_0)/(b_I - a_I)$. After subtracting this parallel capacitance from the susceptance of the monopole with a step at its base, the results will agree very well with that of the monopole without any step discontinuity. Therefore (3.1) provides a good approximation of the parallel capacitance characterizing the step discontinuity at the base of a monopole.

The second type shown in Figure 3.6(b) is usually adopted when the radius of the monopole is greater than the inner radius of the outer conductor of the feed line. Calculated results for the input admittance of the structure shown in Figure 3.6(b) are presented in Figure 3.9, where results for the admittance of a monopole in Figure 3.1 are also given for comparison.

It is well known [3] that the thicker the monopole, the shorter is the resonant length of the antenna, as seen from Figure 3.9. It can also be seen that the terminal condition at the base of the monopole is very important in determining the antenna's admittance. The vertical gap between the monopole's bottom surface

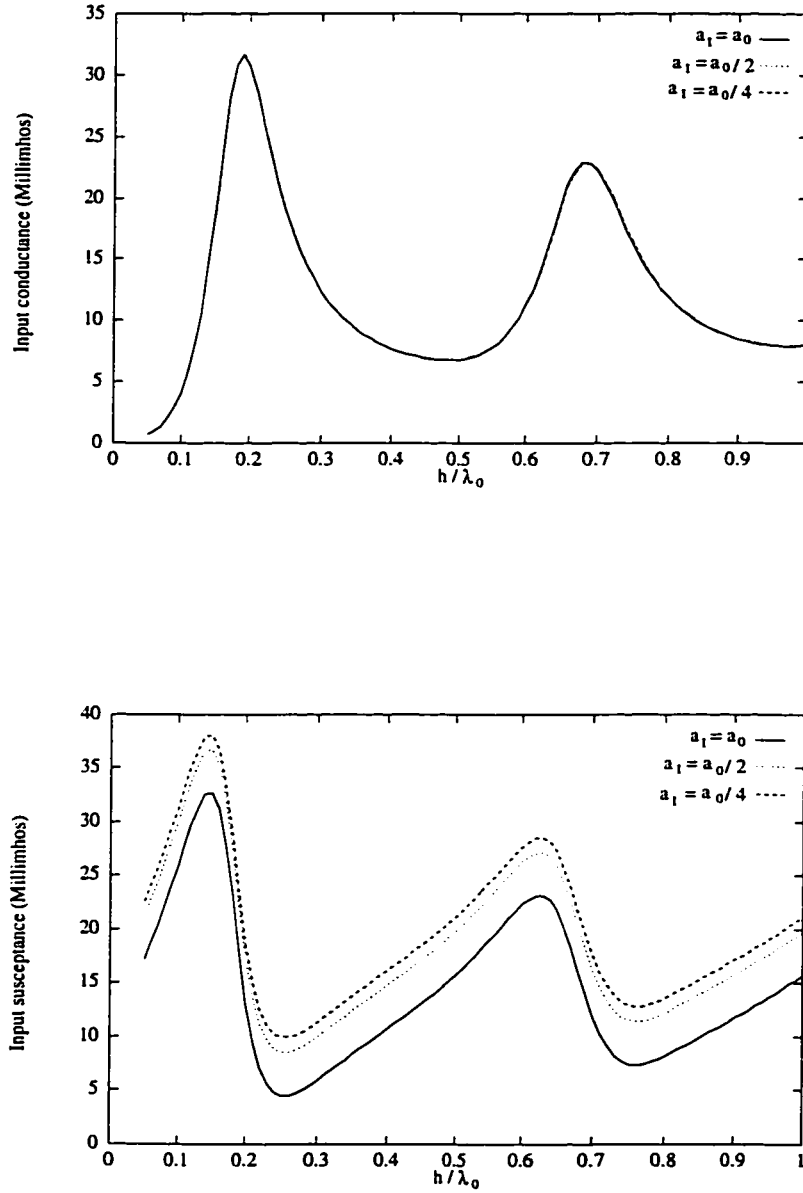


Figure 3.8: Effect of the junction between the feed line and the monopole on the antenna's admittance ($a_0 = 0.0509\lambda_0$, $b_I = 1.187a_I$).

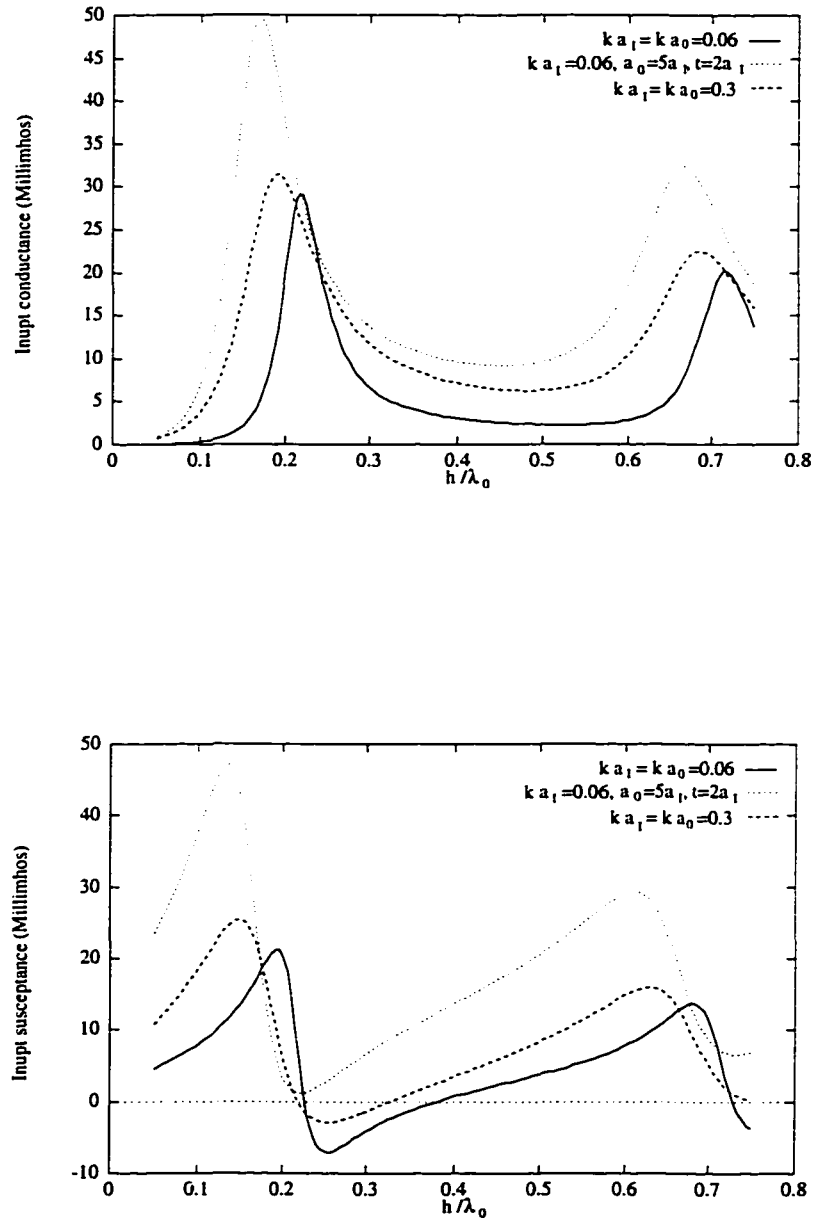


Figure 3.9: Admittance of the monopole shown in Figure 3.6(b) ($b_I = 2.301a_I$).

and the ground plane not only provides a positive susceptance but also increases the conductance.

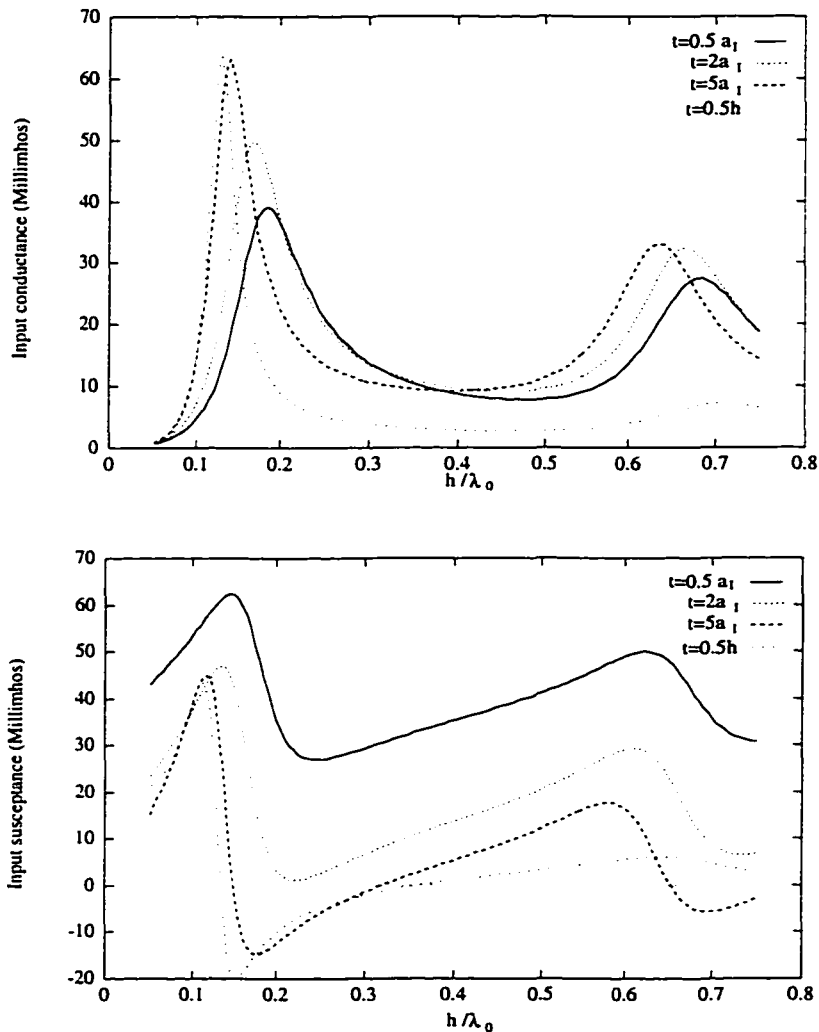


Figure 3.10: Effect of the gap length t between the bottom of the monopole and the ground plane on the antenna's admittance ($a_I = 0.0509\lambda_0$, $b_I = 2.301a_I$, $a_0 = 3b_I$).

The effect of the gap length t between the bottom of the monopole and the ground plane is examined in Figure 3.10. It is seen that the gap length has a significant effect on the antenna's admittance: both the conductance G and the

susceptance B , especially for B when the gap length is small. It is also found that its effect becomes stronger when the monopole is much thicker than the inner conductor of the feed line, as is expected. The fact that increasing the gap length t decreases the antenna's bandwidth is understandable, since increasing the length of the antenna's thin part increases the system's Q value.

The last type of junction between a monopole antenna and its feed line is shown in Figure 3.2(c). Since the step discontinuity in the inner conductor of a coaxial waveguide is characterized by a parallel capacitance expressed in (3.1), the input admittance Y_{in} of the monopole looking from the feed coaxial line can be calculated from the equivalent circuit shown in Figure 3.11, where Y'_{in} is the admittance of the monopole at $z = d + h + t$, i.e., without the junction effect.

$$Y_{in} = j\omega C_s + [Z'_0 Y'_{in} + j \tan(k_1 t)] / [Z'_0 + j(Z'_0)^2 Y'_{in} \tan(k_1 t)] \quad (3.2)$$

where Z'_0 is the characteristic impedance of the coaxial line whose inner and outer radii are a_I and a_1 , respectively.

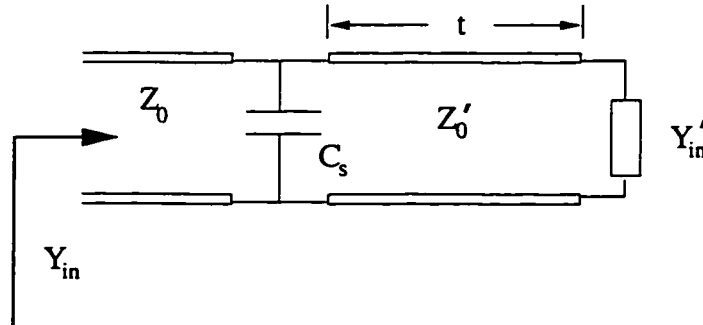


Figure 3.11: Equivalent circuit for characterizing the junction effect of the third type shown in Figure 2.6 (c).

In order to appreciate the effect of the step junction at the monopole base on the antenna's input admittance, we give a comparison between Y'_{in} and Y_{in} , as

illustrated in Figure 3.12. It is found that the step junction has a noticeable effect on the antenna's admittance. It is obvious that the influence strength depends on the size of the step junction and the length t . It is found that the admittance calculated by this expression agrees very well with the full-wave solution obtained by our modal expansion method presented in the preceding chapter. Since the electrical dimensions of the feed line and the step discontinuity are relatively small, the low-frequency circuit model (equations (3.1) and (3.2)) provides a good estimate of the junction effect.

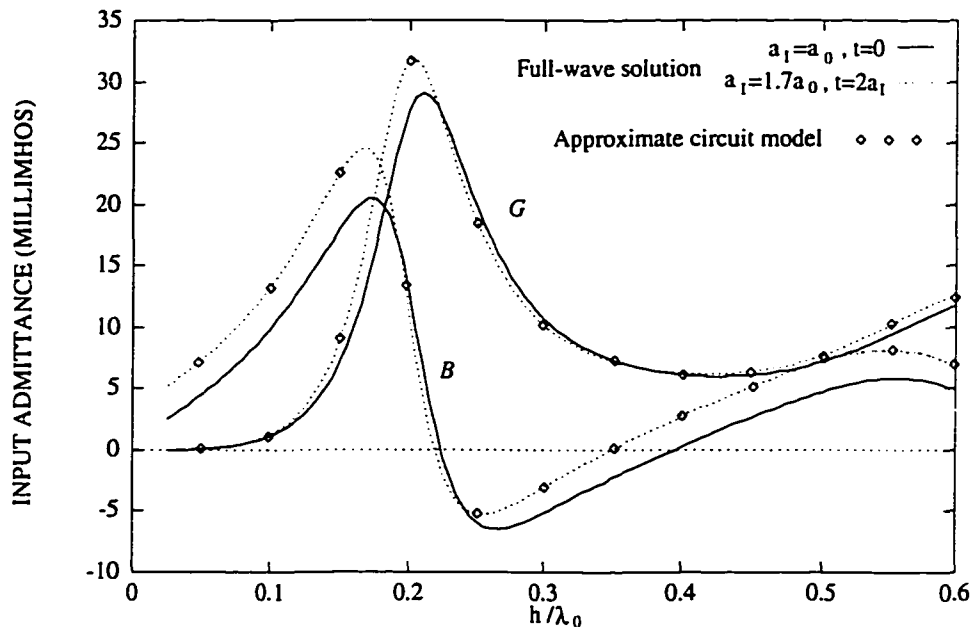


Figure 3.12: Effect of the step junction between the monopole and the feed line on the antenna's admittance ($a_I = 0.0509\lambda_0$, $b_I = 2.301a_I$).

3.2 The Sleeve Monopole

The structure of a sleeve monopole antenna [62] is shown in Figure 2.3, where the electrical dimensions of the feed line are often relatively small. The values of $k_0 a_I = 0.02$ and $k_0 b_I = 0.09$ are assumed in this section. The sleeve is also assumed to be electrically thin ($k_0(a_1 - b_I) = 0.005$). As in the case of the conventional monopole, the convergence behavior of the impedance with respect to the truncation numbers N_I and N_{II} is examined. Tables 3.3 and 3.4 show the convergence of the input impedance of a sleeve monopole with respect to N_I and N_{II} , respectively. It is seen that the choice of $N_I = 2$ and $N_{II} = 80$ is enough to get convergent results for the antenna's impedance.

Table 3.3: Convergence of the impedance (Ohms) of a quarter-wavelength sleeve monopole with respect to N_I ($h = 0.25\lambda_0$, $l = 0.5\lambda_0$).

N_I	Resistance	Reactance
1	61.64	24.98
2	61.60	25.06
4	61.59	25.08

The effect of the distance d on the input impedance of the sleeve monopole is shown in Figure 3.13, where the two dotted lines are for electric wall (EW) and magnetic wall (MW), while the solid line is for the combination of both, i.e., the PMB. It is seen that the assumed EW and MW do not have much effect on the input impedance when $d > 3\lambda_0$. This property is expected since the main radiation of the sleeve monopole occurs in the radial direction. We can also see that the results obtained with the PMB converge much faster than with either the EW alone or the

Table 3.4: Convergence of the impedance (Ohms) of a quarter-wavelength sleeve monopole with respect to N_{II} ($h = 0.25\lambda_0$, $l = 0.5\lambda_0$).

N_{II}	Resistance	Reactance
5	143.92	84.43
10	71.80	48.77
20	65.84	34.12
40	62.85	27.42
80	61.86	25.52
120	61.60	25.06

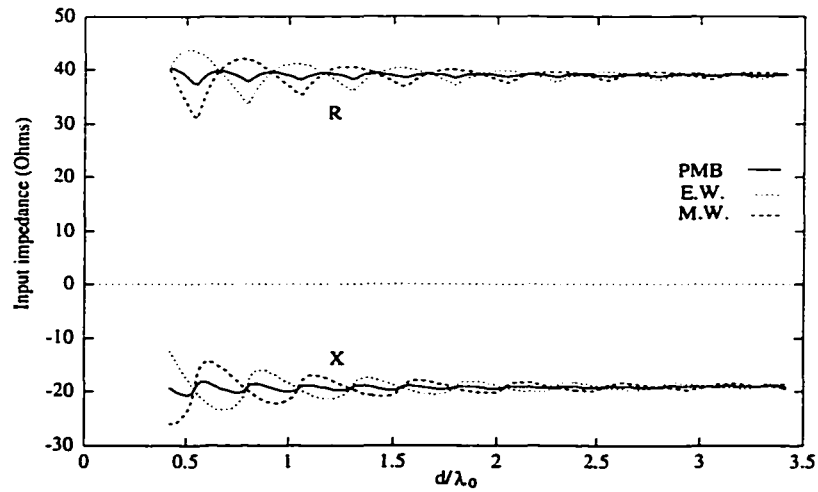


Figure 3.13: Variation of a sleeve monopole's impedance with respect to the distance d ($l = 0.45\lambda_0$, $h = 0.25\lambda_0$).

MW alone. The result obtained with $d = \sqrt{2}\lambda_0$ is seen to be fairly good, which is adapted in the later computations.

To verify the validity of our method, we compute the current distribution and the input impedance of a sleeve-monopole antenna for which results are available in the literature. Figure 3.14 shows our modal-expansion results for the surface-current distribution along both the monopole and the sleeve. The results given in Figure 3.14 have been fitted to the experimental ones [10] at the driving point, $z = d + h$. It is seen that the agreement between our modal-expansion results and Taylor's experimental data is quite good. Figure 3.15 gives the comparison of our computed results with Taylor's experimental values [10] and the theoretical results in [11] for the input impedance of a sleeve-monopole antenna. We can see that our results agree very well with Taylor's measured data, better than those obtained by Rispin and Chang [11]. This is expected since our modal-expansion analysis is formally exact and takes into account all the effects (junction-end effect, effect of the finite thickness of the sleeve, and effect of the feed line) which were ignored in the previous theoretical work.

Figure 3.16 shows the input resistance and reactance of a sleeve-monopole antenna for different sleeve lengths. Since the sleeve itself acts as a cylindrical antenna, a significant influence of the sleeve's length on the input impedance of a sleeve-monopole antenna is expected. Moreover, the change in the length of the sleeve is equivalent to the change of the feed position of an asymmetric linear antenna, which would have a great effect on the antenna's impedance. The far-zone radiated field pattern of a sleeve monopole is illustrated in Figure 3.17 for different values of the sleeve length l . It can be seen that the sleeve length has a remarkable influence on the radiation field pattern. When $l = 0$, the sleeve monopole reduces to the conventional-monopole antenna whose radiation pattern is well understood.

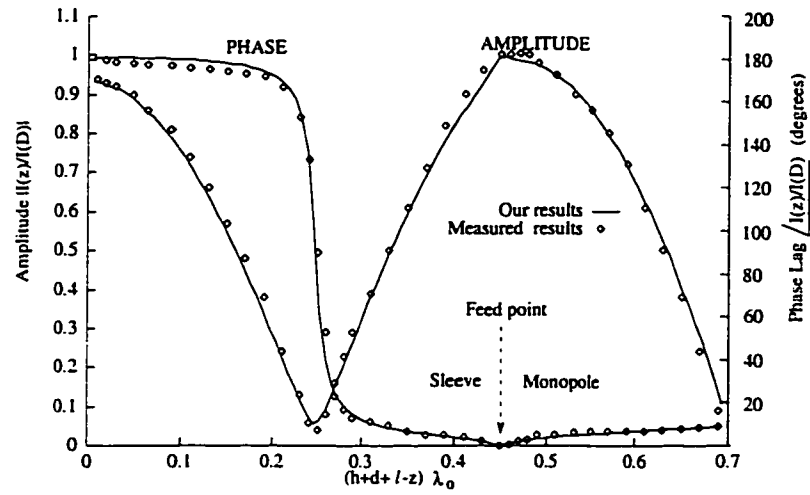


Figure 3.14: Surface current on a sleeve monopole antenna ($l = 0.45\lambda_0$, $h = 0.25\lambda_0$).

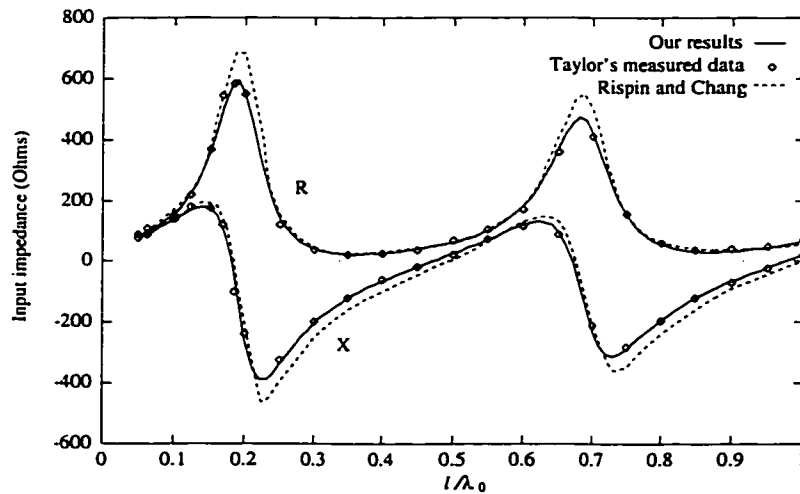


Figure 3.15: Comparison of our results for the impedance of a sleeve monopole with those obtained by others ($h = 0.25\lambda_0$).

It is expected that the number of side-lobes is strongly dependent upon the lengths of l and $l + h$.

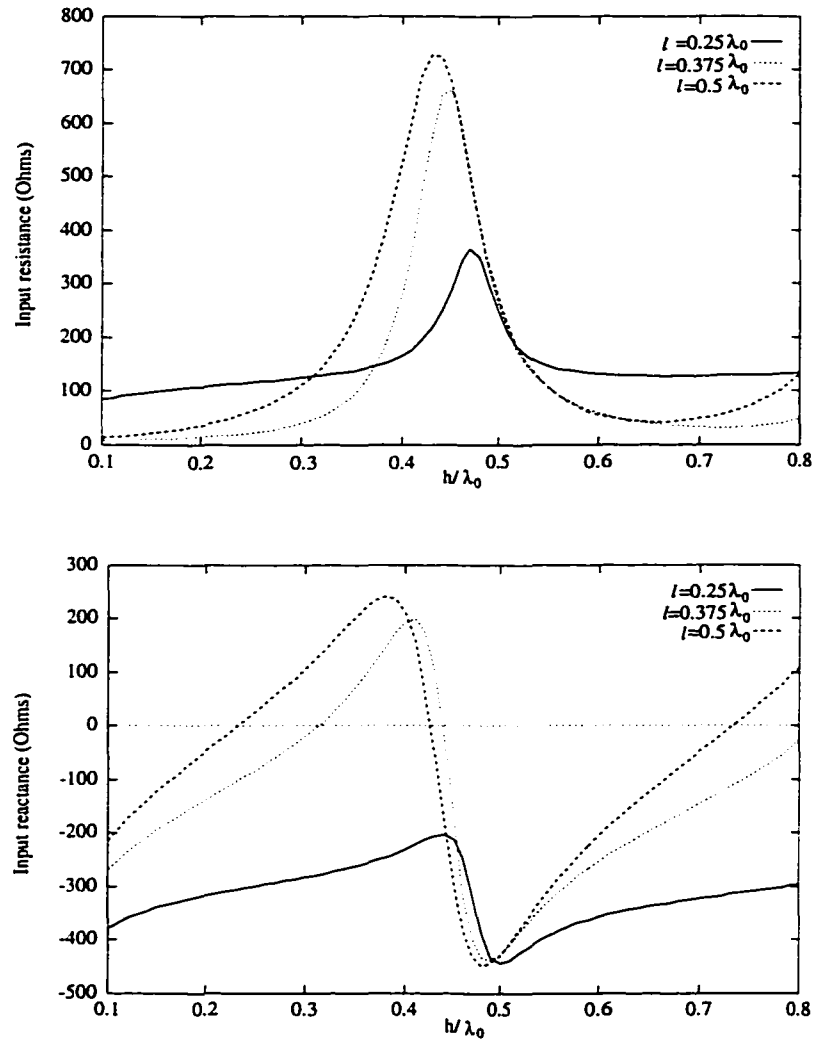


Figure 3.16: Input impedance of a sleeve monopole for different sleeve lengths.

It is found that the relative permittivity of the dielectric in the coaxial feed line has little effect on the input impedance of the sleeve antenna while, of course, it can change the characteristic impedance of the feed line significantly. The characteristic impedance of the coaxial feed line has the form of $Z_0 = 60/\sqrt{\epsilon_r} \ln(b_I/a_I)$. As seen

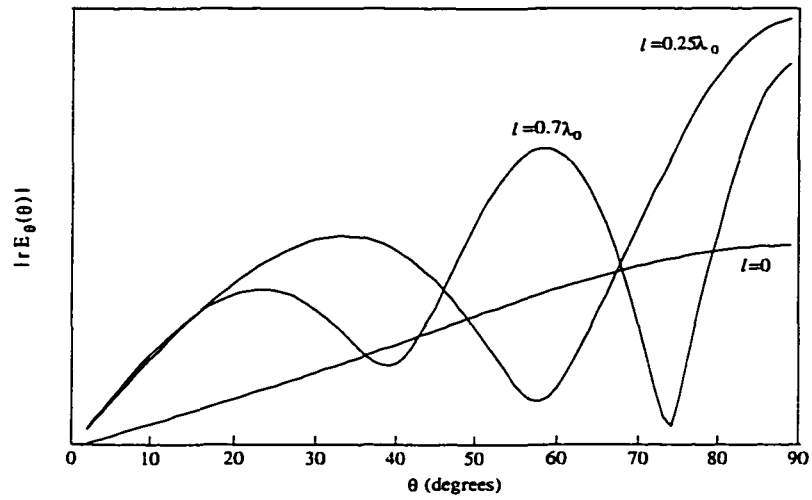


Figure 3.17: Radiation pattern of a sleeve monopole for different sleeve lengths ($h = 0.25\lambda_0$).

Table 3.5: Impedance of a sleeve monopole for different values of relative permittivity of the dielectric in the feed line ($h = l = 0.25\lambda_0$).

Relative permittivity ϵ_{rI}	Characteristic impedance of the feed line (Ohms)	Resistance (Ohms)	Reactance (Ohms)
1.0	90.2	136.9	-335.1
2.2	60.8	135.8	-334.1
3.8	46.3	135.1	-333.5
5.6	38.1	134.9	-333.2
9.6	29.1	134.6	-332.9

from Table 3.3, when the relative permittivity of the dielectric in the feed line changes from 1 to 9.6, the characteristic impedance of the feed line decreases from 90.2 to 29.1 while the input impedance of the sleeve monopole does not change much. The reason for this can be explained by the fact that the input impedance of a wire antenna is mainly determined by its current distribution.

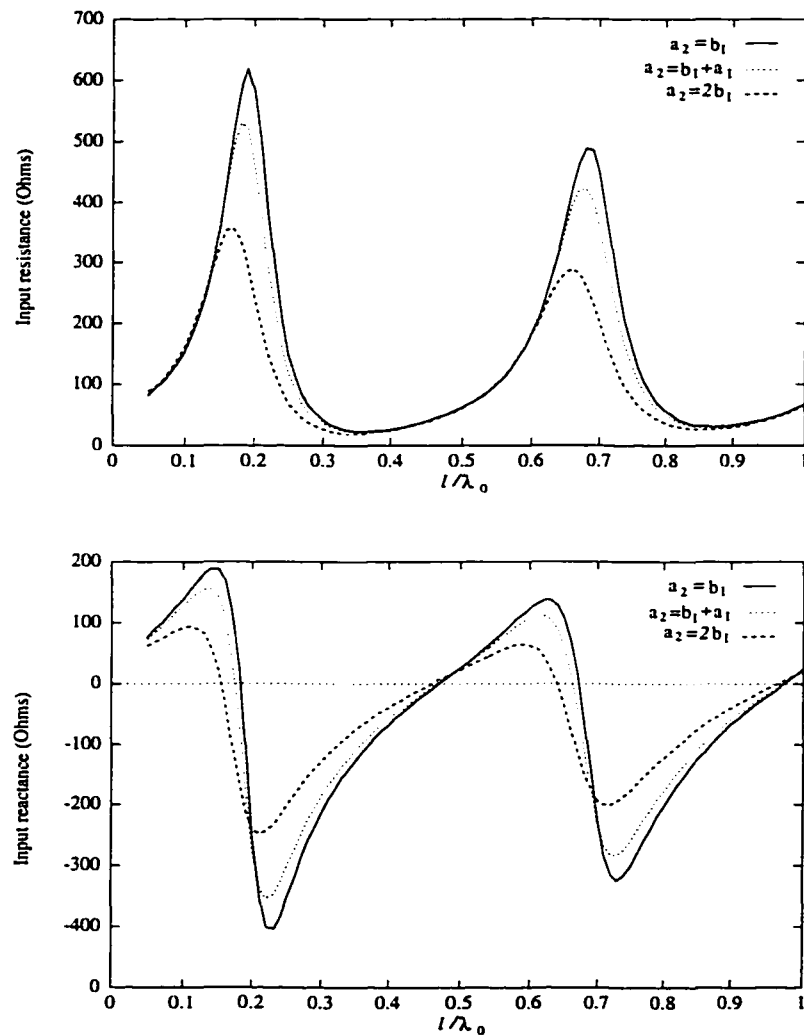


Figure 3.18: Input impedance of a sleeve monopole for different thicknesses of the sleeve.

The effect of the sleeve's finite thickness is illustrated in Figure 3.18. It is seen that increasing the thickness of the sleeve smooths the variations by lowering the magnitude of the resistance and reactance at resonant peaks. This lowers the Q factor and increases the bandwidth of the sleeve antenna. It is also seen that increasing the thickness of the sleeve decreases the antenna's resonant length.

3.3 Dielectric-Coated and Buried Monopoles

It is well known that the performance of a monopole antenna is greatly affected by the environment in which it resides. This section considers two cases involving dielectric: one is the dielectric-coated monopole and the other is the dielectric-buried monopole.

3.3.1 Dielectric-Coated Monopole

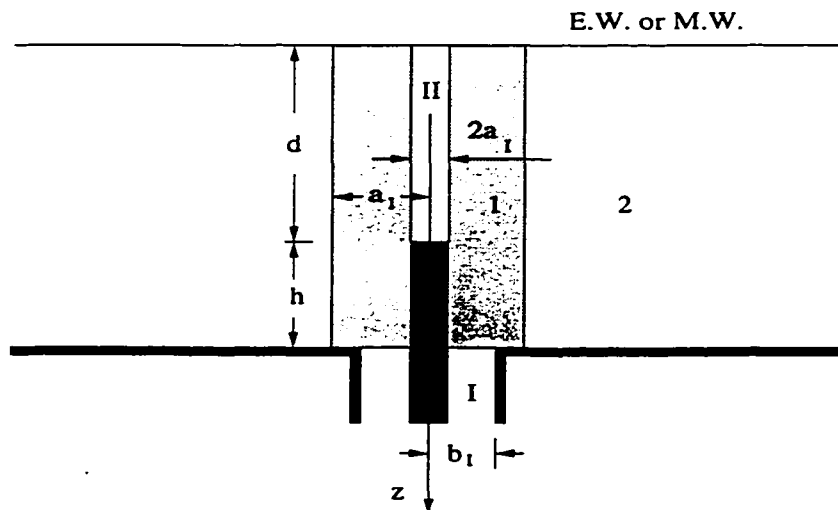


Figure 3.19: Geometry of a dielectric-coated monopole antenna.

The geometry of a monopole antenna coated by a dielectric sheath is shown in Figure 3.19. The monopole of radius $a_I = 3.175\text{mm}$ is coated with an isotropic material of dielectric constant 3.2. A simple check on the effect of the assumed PMB on the antenna's input admittance is given in Figure 3.20. It is seen that the postulated boundary has negligible influence on the antenna's admittance.

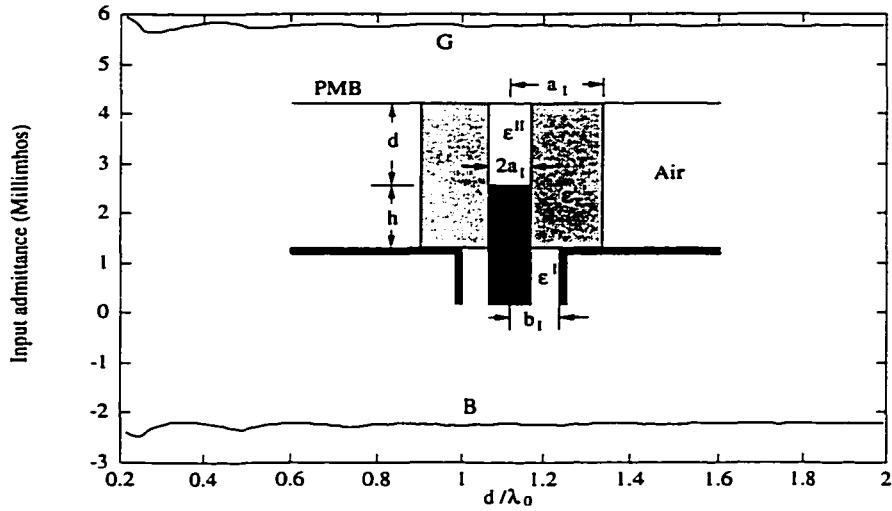


Figure 3.20: Variation of the admittance of a dielectric-coated monopole with respect to d ($b_I = 3a_I$, $a_I = 11.43\text{mm}$, $h = 0.25\lambda_0$, $f = 600\text{MHz}$).

As before, a comparison between our results and experimental ones available in [13] is given in Figure 3.21 for the input admittance of a dielectric-coated monopole antenna. We can see that the agreement is quite good for both the conductance G and the susceptance B . It is obvious that the monopole's resonant conductance increases and its resonant length decreases as the diameter of the cylindrical dielectric coating increases. Similarly, increasing the dielectric constant of the coating cylinder decreases the antenna's resonant length and bandwidth. It should be pointed out here that for a large permittivity of the dielectric coating, our results for the input conductance G of a dielectric-coated monopole agree very well with the ex-

perimental data measured by Lamensdorf [13], while the agreement between our modal expansion results and experimental ones deteriorates for the antenna's susceptance B . A similar disagreement between the moment method solution [15] and the measured data in [13] occurred for coating dielectrics with high permittivity or large diameter.

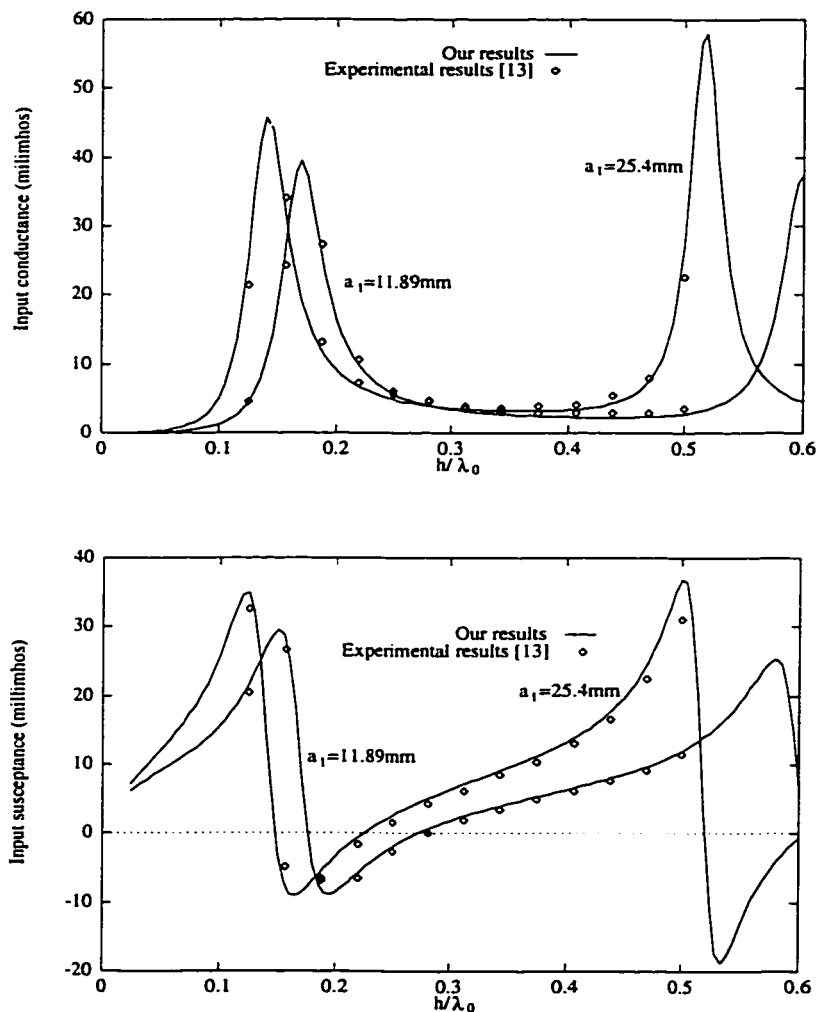


Figure 3.21: Admittance of a dielectric-coated monopole ($b_I = 3a_I$, $f = 0.6\text{GHz}$).

3.3.2 Dielectric-Buried Monopole

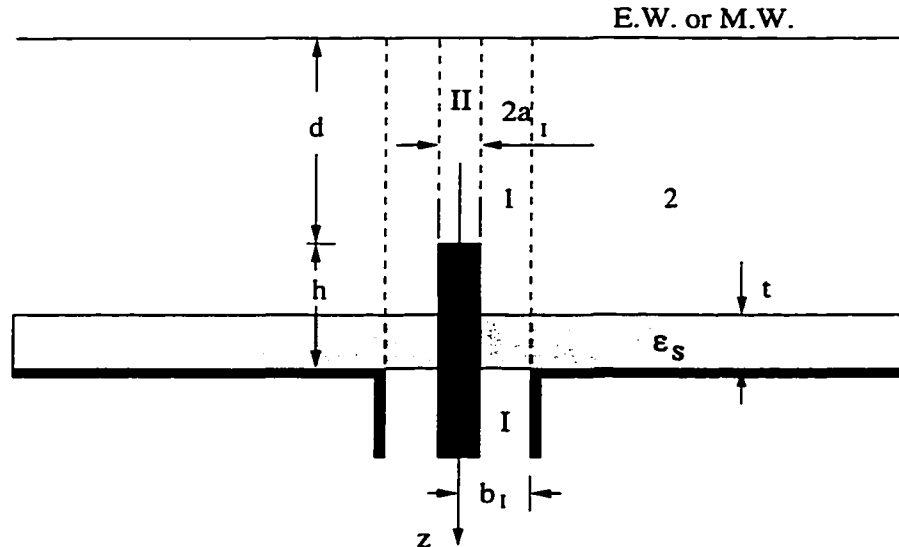


Figure 3.22: Geometry of a monopole antenna partially buried in a grounded substrate.

A vertical monopole antenna partially buried in an infinite substrate [63] is geometrically shown in Figure 3.22. Figure 3.23 shows a Smith chart comparison of our modal expansion results with the experimental values given in [17] for the impedance loci of a half-buried monopole. The substrate is $t = 6.35\text{mm}$ long and its dielectric constant is $\epsilon_{r,s} = 2.2$. The characteristic impedance of the coaxial feed line is 50 Ohms. It is seen that the agreement is quite good.

The power radiated by the monopole antenna can be decomposed into two parts: one is associated with the power carried by surface waves (P_{SW}) and the other is related to radiation waves (P_{RW}). It is known that the field of the surface wave has exponential decay outside and perpendicular to the dielectric substrate, while the field of the radiation wave in the presence of the E.W. or M.W. is a standing wave outside the substrate. The variations of these two parts of the radiated power

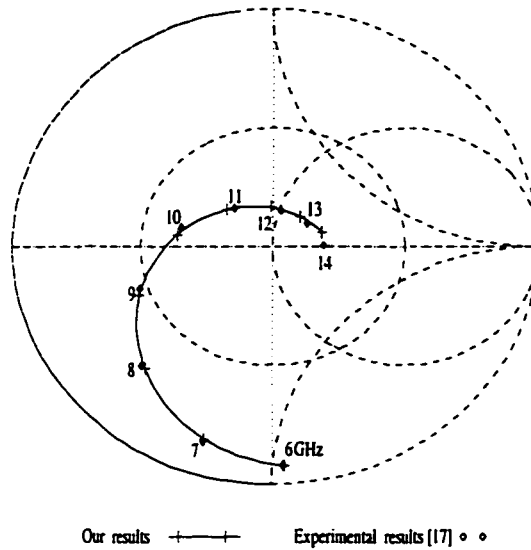


Figure 3.23: Input impedance loci of a monopole partially buried in a grounded dielectric substrate ($a_I = 6.35mm$, $b_I = 3.24a_I$).

with respect to the dielectric's relative permittivity and the substrate thickness are, respectively, illustrated in Figures 3.24 and 3.25, where P_r is the total radiated power. It should be mentioned here that Figures 3.24 and 3.25 are obtained by letting d be several free-space wavelengths to accurately simulate the actual half space. When $\epsilon_{r,s} = 1$, which corresponds to the unloaded free-space case, it is obvious that no surface wave can be excited. However, when $\epsilon_{r,s}$ increases the power carried by the surface waves (only one surface wave mode is excited when $\epsilon_{r,s} < 17$) increases dramatically and the power associated with the radiation waves decreases accordingly. For the half-buried case ($t = 0.5h$) when $\epsilon_{r,s}$ is about 5.4, almost all the power will be radiated in the form of surface waves. From these figures we can also see that increasing the substrate thickness may increase the excitation efficiency of surface waves.

The effect of the substrate's permittivity on the resonant length and input

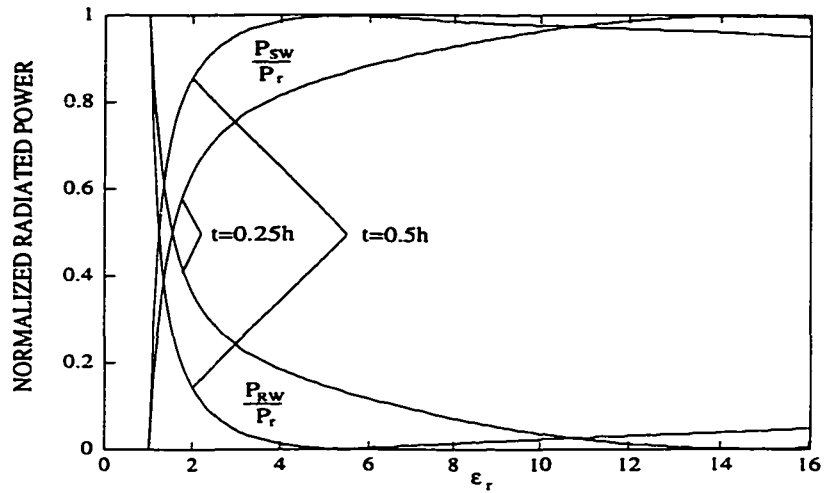


Figure 3.24: Normalized radiated power vs. relative dielectric constant ϵ_r , for a buried quarter-wavelength monopole ($k_0 a_I = 0.05985$, $b_I = 2.301 a_I$).

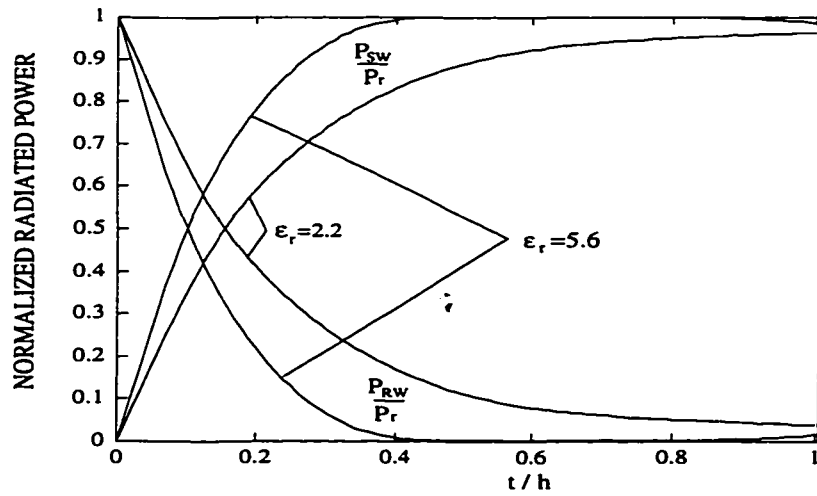


Figure 3.25: Normalized radiated power vs. substrate thickness t/h for a buried quarter-wavelength monopole ($k_0 a_I = 0.05985$, $b_I = 2.301 a_I$).

impedance of a buried monopole antenna is examined in Figures 3.26 and 3.27. As we expect, the existence of the dielectric substrate has a significant effect on the monopole's radiation. Since more energy is coupled into guided waves inside the substrate, the antenna's resonant length decreases greatly when the dielectric permittivity increases as illustrated in Figure 3.26 where the curve $l_r/\lambda_0 = 0.23/\sqrt{\epsilon_{rs}}$ is also given for the resonant length of the monopole antenna immersed in a dielectric half-space ($t = \infty$). It is seen that the thickness of the dielectric substrate has a noticeable effect on the antenna's resonant length when t is small; the effect becomes very weak when $t > h$. When $\epsilon_{es} = 1$, the problem considered here reduces to the conventional monopole problem. In Figure 3.27, King's results [4] for this simplified case are also shown for comparison; very good agreement is observed. Another interesting property of the buried monopole is that the impedance's variation, with respect to the monopole's length, is significantly smoothed when the substrate's permittivity increases.

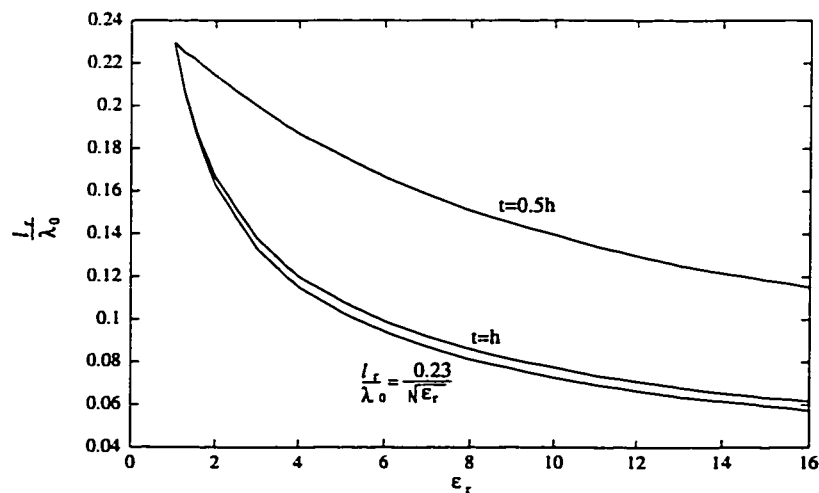


Figure 3.26: Resonant length vs. relative dielectric constant ϵ_{rs} for the buried monopole ($a_I = 0.00635\lambda_0$, $b_I = 2.301a_I$).

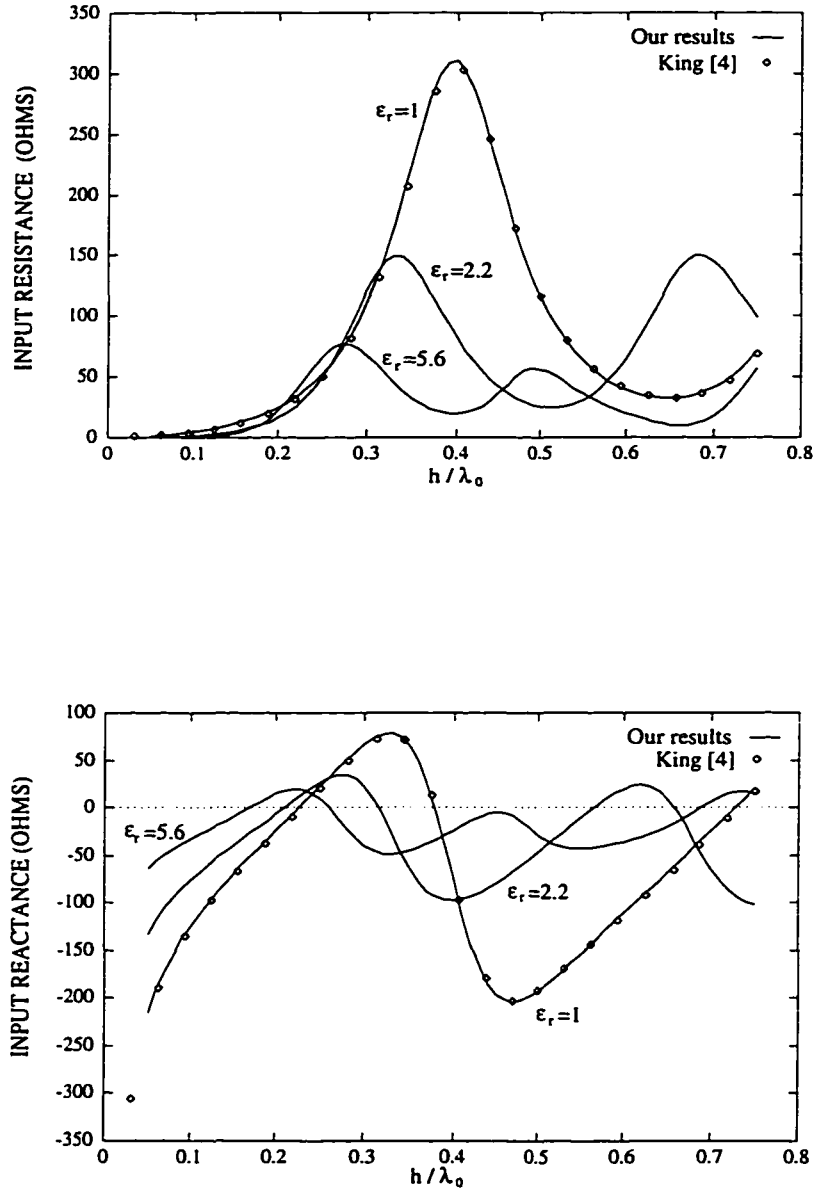


Figure 3.27: Input impedance of a monopole half-buried in a grounded dielectric substrate for different dielectric permittivities ($k_0 a_I = 0.05985$, $b_I = 2.301 a_I$).

3.4 Insulated Monopoles

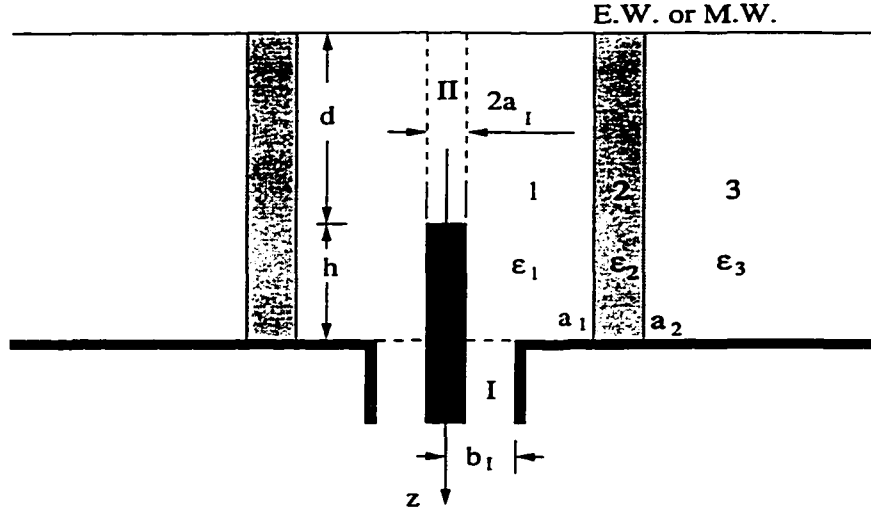


Figure 3.28: Geometry of an air-insulated monopole antenna.

Figure 3.28 illustrates the geometry of an air-insulated monopole antenna [64]. The effect of the assumed PMB on the input admittance of an air-insulated quarter-wavelength monopole in sand ($\epsilon_{r3} = 3.8$) is examined in Figure 3.29. It can be seen that the effect is negligible even when the distance d from the PMB to the end of the monopole is fairly small. Since more energy is stored in the external medium, the effect caused by the assumed PMB becomes weaker.

Figure 3.30 presents our modal expansion results for the input admittance of an air-insulated monopole antenna in lake water ($\epsilon_{r3} = 80$) at $f_0 = 380MHz$. Figures 3.31 and 3.32 illustrate the current distribution and input admittance of the same monopole antenna in sand ($\epsilon_{r3} = 3.8$); also given in these figures are the theoretical and experimental data obtained by Lee et al. [23], [24]. It is noted that $exp(j\omega t)$ is used as the time-harmonic factor in this thesis, rather than $exp(-i\omega t)$ which was employed in the previous work; this explains the reason why $-Arg[I(z)]$ is used in

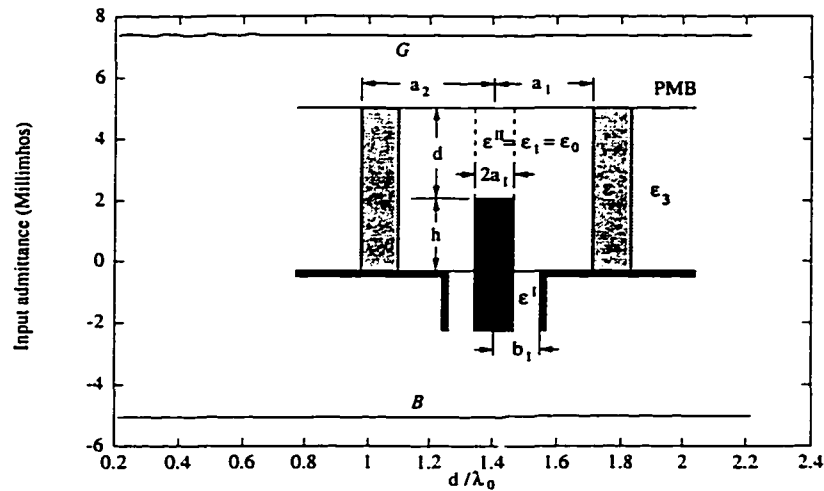


Figure 3.29: Variation of the admittance of an air-insulated quarter-wavelength monopole in sand with respect to d ($a_I = 3.175mm$, $b_I = 3a_I$, $a_1 = 4a_I$, $f = 380MHz$).

Figure 3.31. Our results agree very well with those computed by Lee et al. [23], while there is a difference between both our calculated results and the theoretical results and experimental ones in [24]. This small disagreement can be attributed to the differences between our theoretical model and the actual antenna structure. There is a junction between the feed line and the insulated monopole [21], whose effect studied in the first section is not taken into account in the theoretical analysis. Another difference between the theoretical model and the actual antenna structure is that the thickness of the insulating layer can never be zero; its effect will be examined later. After taking these differences into account, we may say that the agreement between our modal expansion results and experimental ones is fairly good.

Figure 3.33 shows the variation of the input admittance of an air-insulated monopole with respect to the radius of the insulating layer whose thickness is still

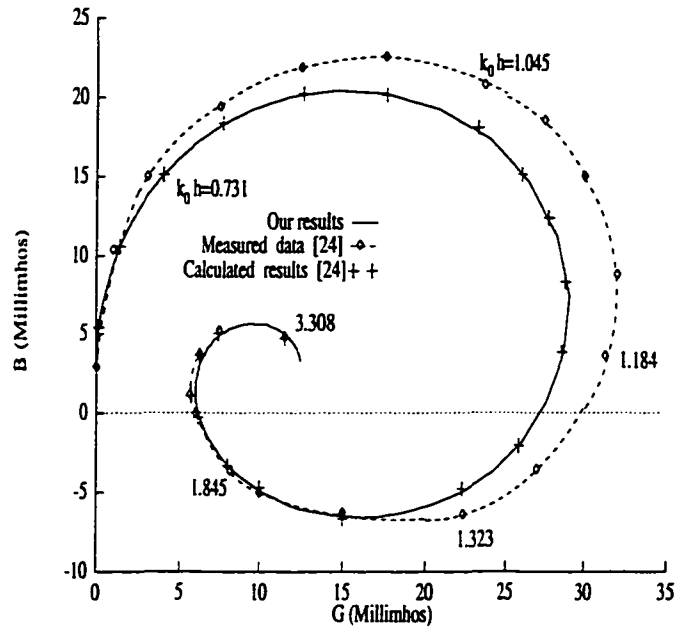


Figure 3.30: Input admittance of an air-insulated monopole in lake water ($a_I = 3.175\text{mm}$, $b_I = 3a_I$, $a = 2 = a_1 = 4a_I$).

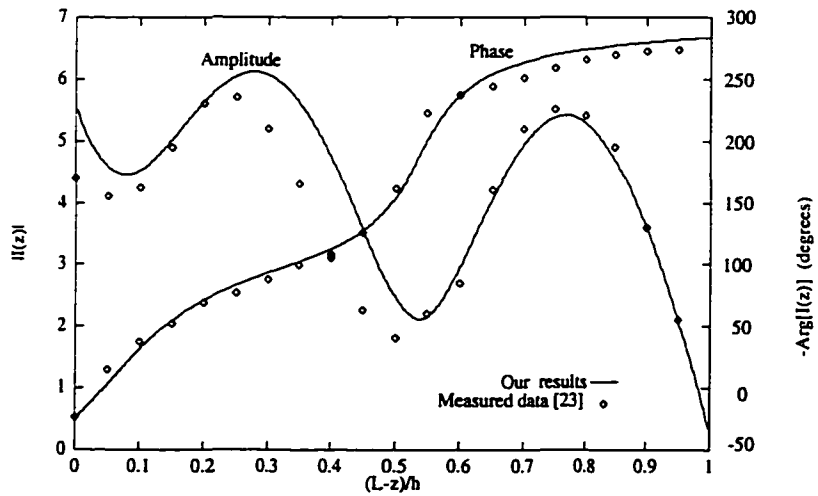


Figure 3.31: Current distribution on an air-insulated monopole antenna in sand ($a_I = 3.175\text{mm}$, $b_I = 3a_I$, $a_2 = a_1 = 4a_I$).

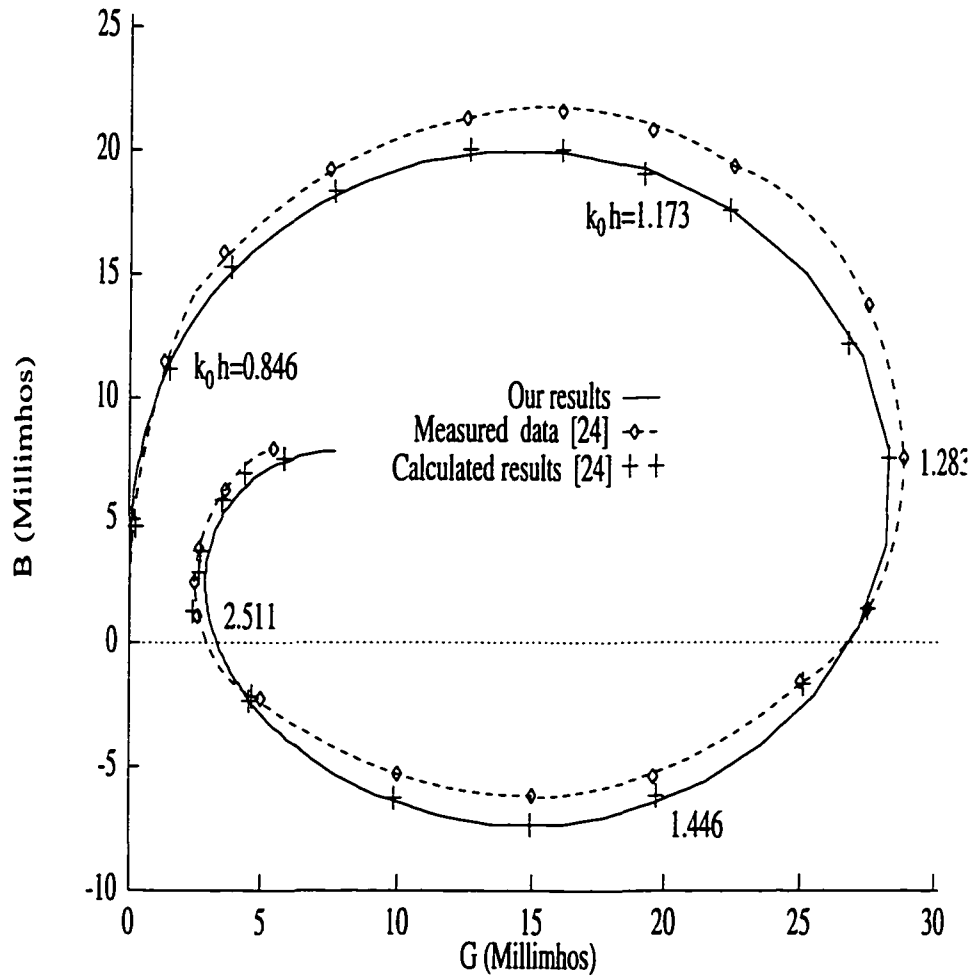


Figure 3.32: Input admittance of an air-insulated monopole antenna in sand ($a_I = 3.175mm$, $b_I = 3a_I$, $a_2 = a_1 = 4a_I$).

assumed to be zero. Since for the insulated monopole antenna most of the power is radiated in the radial direction, the effect of the permittivity discontinuity between the insulating air and its ambient medium is very similar to a step discontinuity in characteristic impedance of a lossy transmission line. Meanwhile, the radial line is non-uniform; its characteristic impedance decreases very rapidly as the radius increases. Therefore, the curve of the input admittance versus a_2/a_I , is somewhat like a fast-decaying standing wave, as illustrated in Figure 3.33. Furthermore, since the admittance of an antenna in an infinite homogeneous medium is proportional to $\sqrt{\epsilon_r}$ [3], its magnitude variation is expected to be bigger for higher permittivity of the ambient medium, as seen in Figure 3.33.

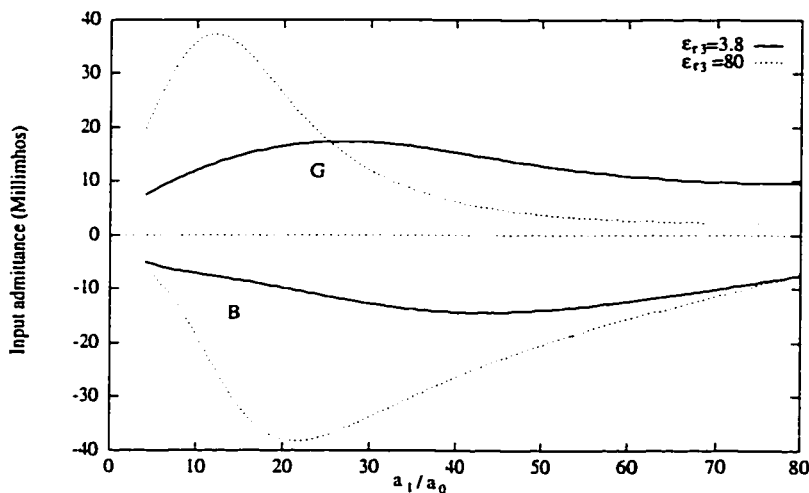


Figure 3.33: Variation of the admittance of an air-insulated quarter-wavelength monopole with respect to a_1/a_I ($a_I = 3.175mm$, $b_I = 2.301a_I$, $f_0 = 380MHz$).

Figure 3.34 gives the input admittance with respect to the relative dielectric constant of the external medium. It is expected that when ϵ_{r3} increases, the reflection coefficient at the interface between the insulating layer and the external medium and the antenna's admittance (absolute value) will also increase. Figure 3.34 ver-

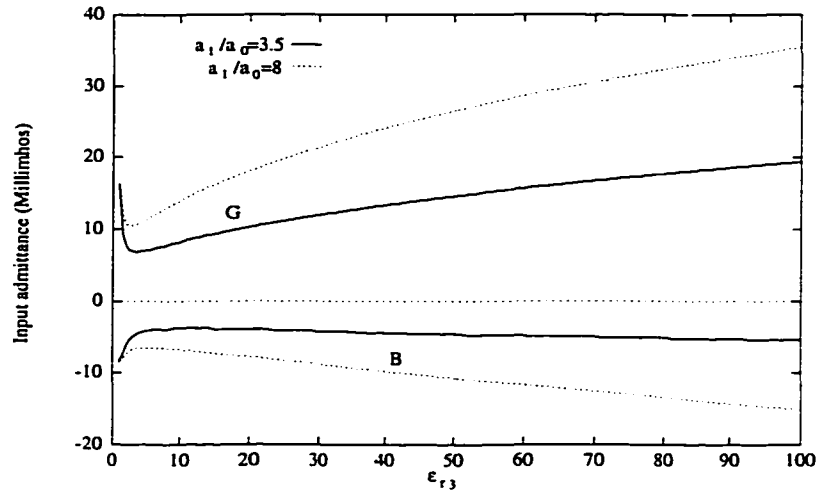


Figure 3.34: Variation of the admittance of an air-insulated quarter-wavelength monopole with respect to the dielectric constant ϵ_{r3} of the external medium ($a_I = 3.175mm$, $b_I = 2.301a_I$, $f_0 = 380MHz$).

ifies this prediction except the very small ϵ_{r3} for which the reflection coefficient is not large enough to dominate the variation.

Finally, we take an air-insulated monopole antenna with an insulating glass layer ($\epsilon_{r3} = 4.82$) of finite thickness as an example of a multilayer insulated monopole in lake water. Figure 3.35 shows the input admittance of the insulated monopole for different thicknesses of the insulating layer. The thickness has a significant effect on both the conductance and the susceptance. This is expected since a big difference exists in the relative permittivities of the insulating glass and lake water and this difference changes the equivalent radius of the insulating layer which has a noticeable effect on the antenna's admittance (see Figure 3.33). The effect becomes negligible for the case of an air-insulated monopole immersed in sand since the difference in the permittivities of glass ($\epsilon_{r3} = 4.82$) and sand ($\epsilon_{r3} = 3.8$) is relatively small.

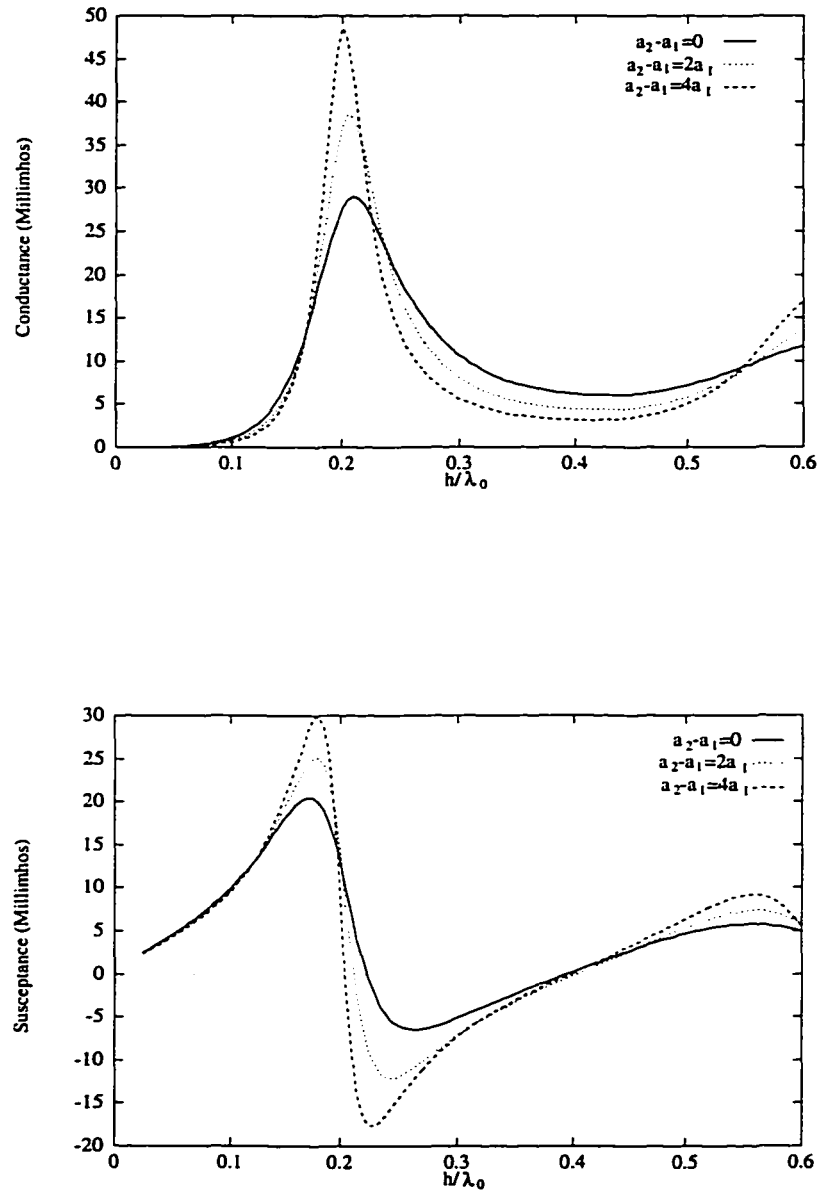


Figure 3.35: Effect of the finite thickness of the insulating layer on a monopole's admittance ($a_I = 3.175\text{mm}$, $b_I = 2.301a_I$, $a_1 = 4a_I$).

3.5 Monopole on a Finite Ground-Plane

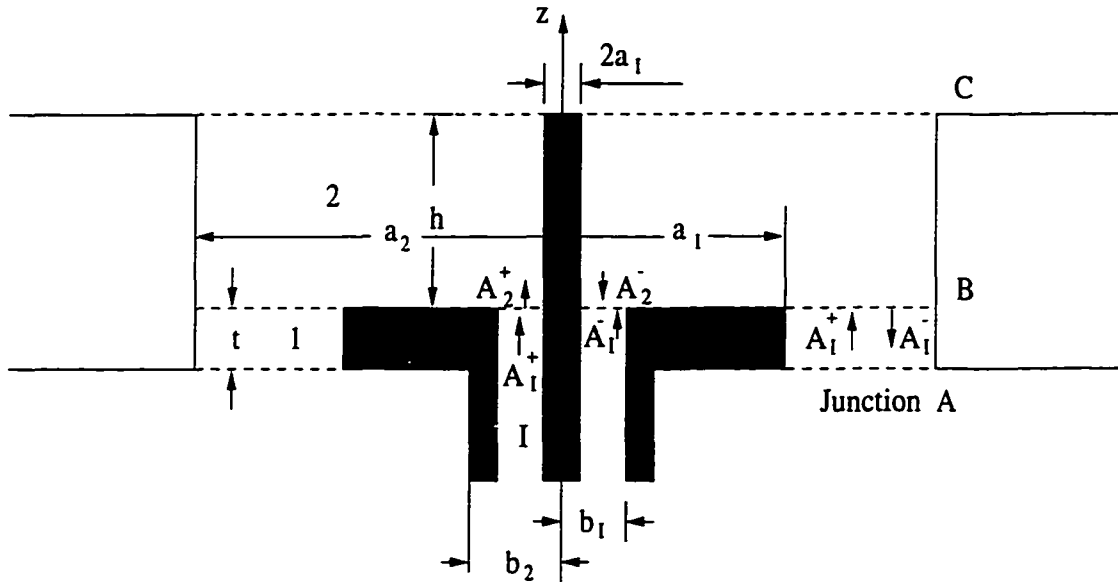


Figure 3.36: Theoretical model for a monopole over a finite ground plane.

Figure 3.36 shows the theoretical model employed to analyze the problem of a monopole antenna fed through a circular ground plane by a coaxial line. After properly introducing an outer coaxial cylindrical wall of radius a_2 , the structure reduces to a cascaded coaxial-to-coaxial waveguide junction problem. The radius and length of the monopole antenna are a_I and h , respectively. The ground plane is of radius a_1 and of thickness t . From Figure 3.36, we identify three coaxial waveguides (guide I, guide 1, and guide 2); their inner and outer radii are, respectively, (a_I, b_I) , (a_1, a_2) , and (a_I, a_2) . There are also three waveguide junctions (A, B, C) in Fig.3.36. Junction A is actually an infinitely long monopole fed by coaxial waveguide 1. The radius of this infinitely long monopole is b_2 , as shown in Fig. 3.36. Junction C is basically an open-ended coaxial line with infinite flange. The reflection matrices of junctions A and C are computed by using the complexifica-

tion and extrapolation technique [65], [66], which will be introduced in the next chapter.

Since the structure considered and the incident TEM mode in the feed line are axi-symmetric ($\frac{\partial}{\partial\phi} = 0$), only the dominant TEM mode and TM_{0n} in these waveguides can be excited. The numbers of modes considered in three coaxial waveguides are assumed to be N_I , N_1 , and N_2 , respectively. As also illustrated in Fig.3.36, A_I^+ , A_I^- are incident and reflected modal amplitude column vectors in feed waveguide at $z = 0$. A_1^+ , A_1^- and A_2^+ , A_2^- are similarly defined for the modal amplitude column vectors in guides 1 and 2 at $z = 0$, respectively. The following two relations are obvious

$$A_1^+ = L_1 S_{A11} L_1 A_1^- \quad (3.3)$$

$$A_2^- = L_2 S_{C11} L_2 A_2^+ \quad (3.4)$$

where S_{A11} and S_{C11} are the reflection matrices of Junctions A and C, which are obtained by the complexification and extrapolation technique [65], [66]. L_1 and L_2 are the diagonal transmission matrices of guides 1 and 2 with

$$L_{1,n,n} = \exp(-j\beta_{1,n}t) \quad (3.5)$$

$$L_{2,n,n} = \exp(-j\beta_{2,n}h) \quad (3.6)$$

as their diagonal elements, respectively.

Application of the conservation of complex power technique (CCPT) [67], [68] to Junction B at $z = 0$ results in

$$A_2^+ + A_2^- = M_{2I}(A_I^+ + A_I^-) + M_{21}(A_1^+ + A_1^-) \quad (3.7)$$

$$Y_I(A_I^+ - A_I^-) = M_{2I}^T Y_2(A_2^+ - A_2^-) \quad (3.8)$$

$$Y_1(A_1^+ - A_1^-) = M_{21}^T Y_2(A_2^+ - A_2^-) \quad (3.9)$$

where \mathbf{Y}_i , for $i = I, 1$, and 2 , is the modal admittance matrix for the i th waveguide, \mathbf{M}_{2I} and \mathbf{M}_{21} are the E-field mode-matching matrices between guides 2 and I and between guides 2 and 1, respectively; their detailed expressions can be found in Appendix B.

Substituting (3.3) and (3.4) into the above three equations, one can obtain after some manipulations

$$\mathbf{A}_I^- = \Gamma_{in} \mathbf{A}_I^+ = [2(\mathbf{I} + \mathbf{Y}_I^{-1} \mathbf{Y}_{L0})^{-1} - \mathbf{I}] \mathbf{A}_I^+ \quad (3.10)$$

where

$$\mathbf{Y}_{L0} = \mathbf{Y}_p - \mathbf{Y}_q \mathbf{W} [\mathbf{Y}_1 (2\mathbf{I} - \mathbf{W}) + \mathbf{Y}_s \mathbf{W}]^{-1} \mathbf{Y}_q^T \quad (3.11)$$

with

$$\mathbf{Y}_p = \mathbf{M}_{2I}^T \mathbf{V} \mathbf{M}_{2I} \quad (3.12)$$

$$\mathbf{Y}_q = \mathbf{M}_{2I}^T \mathbf{V} \mathbf{M}_{21} \quad (3.13)$$

$$\mathbf{Y}_s = \mathbf{M}_{21}^T \mathbf{V} \mathbf{M}_{21} \quad (3.14)$$

$$\mathbf{W} = \mathbf{I} + \mathbf{L}_1 \mathbf{S}_{A11} \mathbf{L}_1 \quad (3.15)$$

and

$$\mathbf{V} = \mathbf{Y}_2 (\mathbf{I} - \mathbf{L}_2 \mathbf{S}_{C11} \mathbf{L}_2) (\mathbf{I} + \mathbf{L}_2 \mathbf{S}_{C11} \mathbf{L}_2)^{-1}. \quad (3.16)$$

From (3.10) one can extract the reflection coefficient Γ_{I0} for the dominant TEM mode in the coaxial feed waveguide. Then the input impedance of the monopole antenna is calculated from (2.58).

For most practical applications, the length of a monopole is taken as $h = 0.25\lambda_0$ or slightly less; this choice of h makes most of the diagonal elements of the transmission matrix \mathbf{L}_2 decay very rapidly; only the upper-left corner of matrix \mathbf{V} contributes significantly to the final results. Thus, \mathbf{Y}_p , \mathbf{Y}_q , and \mathbf{Y}_s in (3.12) and

(3.15) can be decomposed into two parts: one is the matrix-product part involving matrices of small size; the other can be put into a single summation form to save computer time and memory.

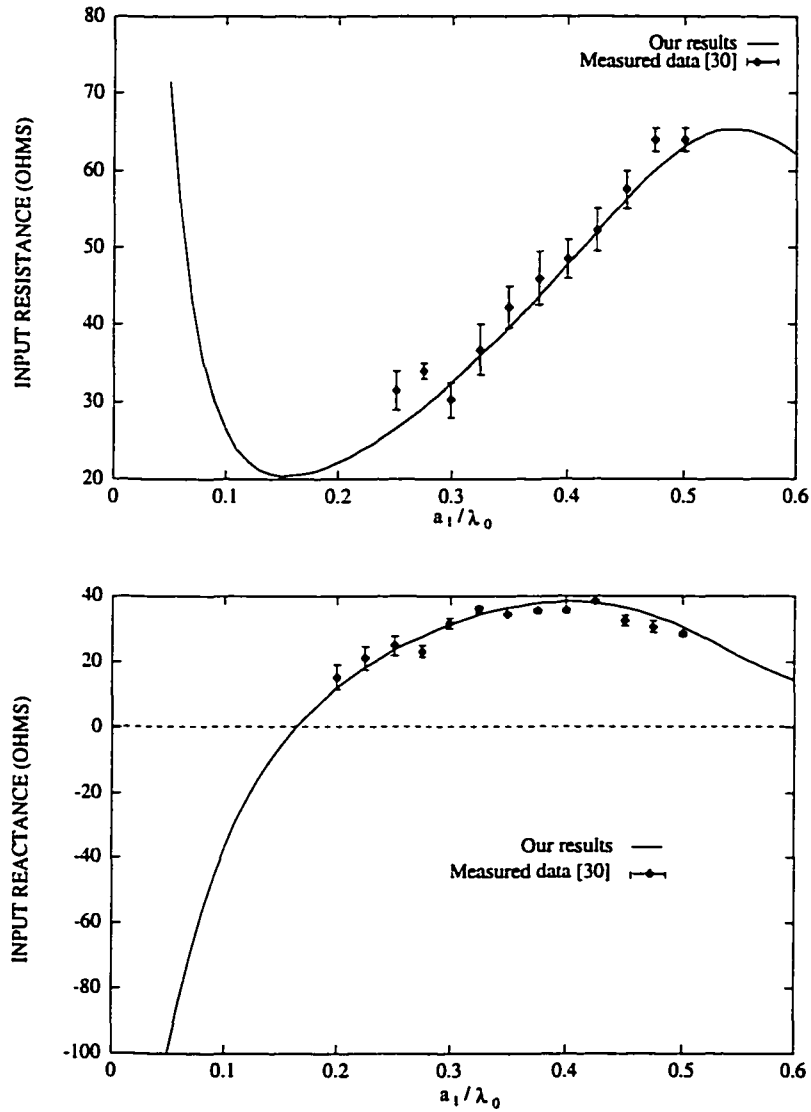


Figure 3.37: Variation of the impedance of a monopole with respect to a_1/λ_0 ($a_I = 1.588mm$, $b_I = 5.2mm$, $a_1 = 75mm$).

In order to verify the validity of the proposed waveguide modal analysis, a comparison between our calculated results and experimental ones measured by Thiele and Newhouse [30] is shown in Figure 3.37. It can be seen that the agreement is very good for both the input resistance R and the input reactance X . Shown in Table 3.6 is another independent comparison of our calculated results with those carefully measured by Weiner et al. [34], wherein MM denotes the moment method solution available in [33]. It is noted that the agreement is also quite good.

The input impedance of a thin quarter-wave monopole is plotted in Figure 3.38 as a function of the radius of the circular ground plane for a larger range of the ground plane's radius. Also shown in Figure 3.38 is the impedance of the same monopole over an infinitely large ground plane [4]. It is obvious that the effect of the radius of the finite ground plane becomes weaker and weaker when it increases though the convergence rate is slow.

The effect of the finite thickness of the circular ground plane on the input impedance of a quarter-wave monopole antenna is illustrated in Figure 3.39. It is expected that a monopole over a thick ground plane will exhibit a lower effective Q and is somewhat equivalent to a ground plane of bigger radius. Therefore, increasing the thickness of the circular ground plane decreases the magnitude of the variation, but maintains the curve shape, as seen from Figure 3.39.

It should be pointed out that the thickness $b_2 - b_1$ of the coaxial feed line has a negligible effect on the antenna's input impedance. This is understandable since only a very small amount of power can reach the down-side of the ground-plane. The value of $b_2 - b_1 = a_1$ is used in the above computations.

Table 3.6: Input impedance of 0.5in diameter monopole elements on an 8ft diameter ground plane.

f (MHz)	h (in)	Resistance (Ohms)			Reactance (Ohms)		
		Ours	MM	Measured	Ours	MM	Measured
30.0	94.26	17.37	17.76	17.62	-38.59	-35.97	-30.92
36.0	78.55	16.77	18.35	18.57	-26.48	-25.48	-13.59
43.0	65.46	16.97	18.77	19.05	-18.43	-19.33	-16.38
54.0	52.07	18.64	19.93	20.15	-7.95	-12.11	-5.92
62.4	45.00	20.32	20.80	22.82	-2.49	-4.73	-0.48
75.0	37.36	23.44	22.95	23.23	3.71	-0.43	1.60
86.0	32.48	26.71	25.35	27.63	7.15	3.34	7.39
89.7	31.13	28.05	26.59	28.16	8.35	4.99	-1.05
97.5	28.60	31.13	29.41	31.22	10.09	7.29	11.05
117.0	23.76	40.36	39.27	40.50	10.34	8.27	15.21
136.5	20.34	46.54	45.76	46.23	2.83	0.84	7.18
156.0	17.75	41.79	40.39	38.59	-5.14	-8.16	-1.09
175.5	15.77	34.97	34.00	30.94	-3.94	-7.45	-1.91
195.0	14.14	31.88	30.54	25.58	0.21	-4.36	0.51
214.5	12.82	32.78	30.33	28.28	4.66	-0.18	4.87
234.0	11.74	36.82	33.69	31.44	7.56	3.64	5.56
253.5	42.38	42.28	40.25	41.13	7.29	3.91	6.57

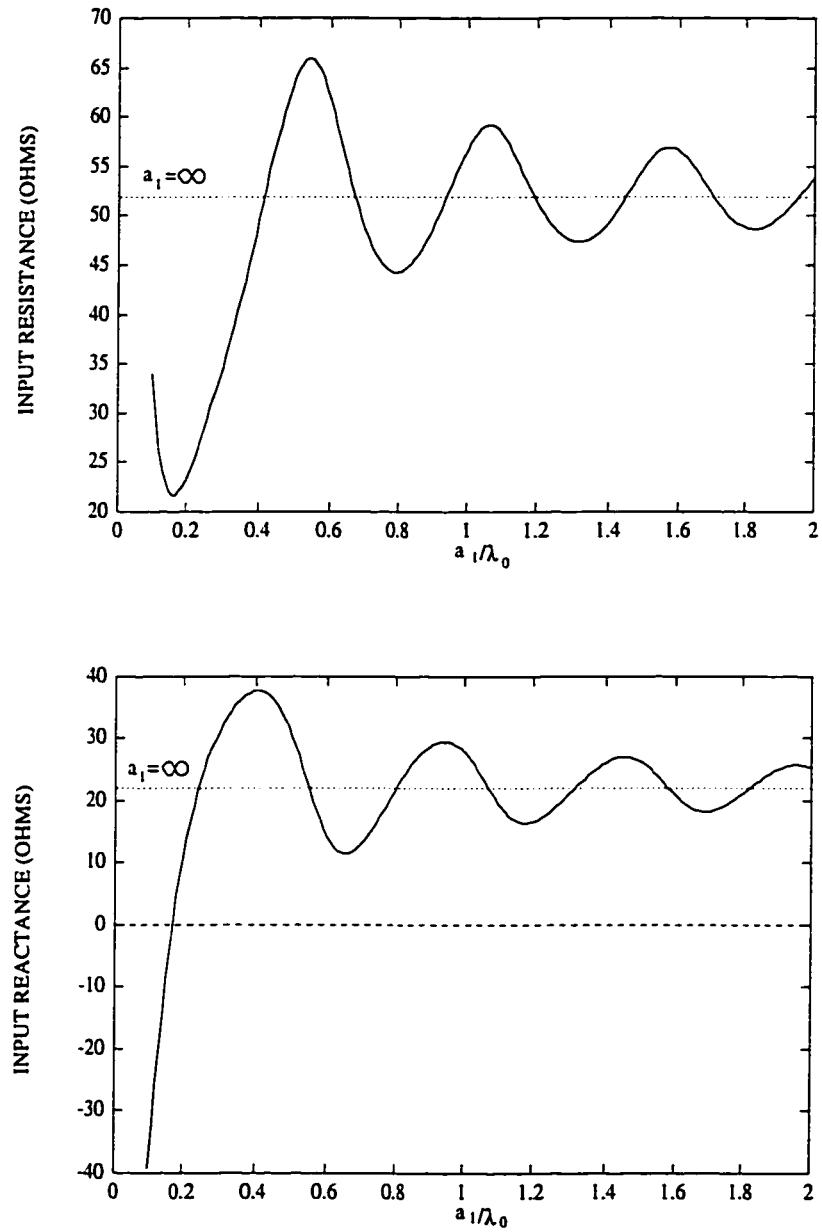


Figure 3.38: Variation of the impedance of a monopole with respect to the normalized radius a_1/λ_0 of the ground plane (same parameters as Figure 3.37).

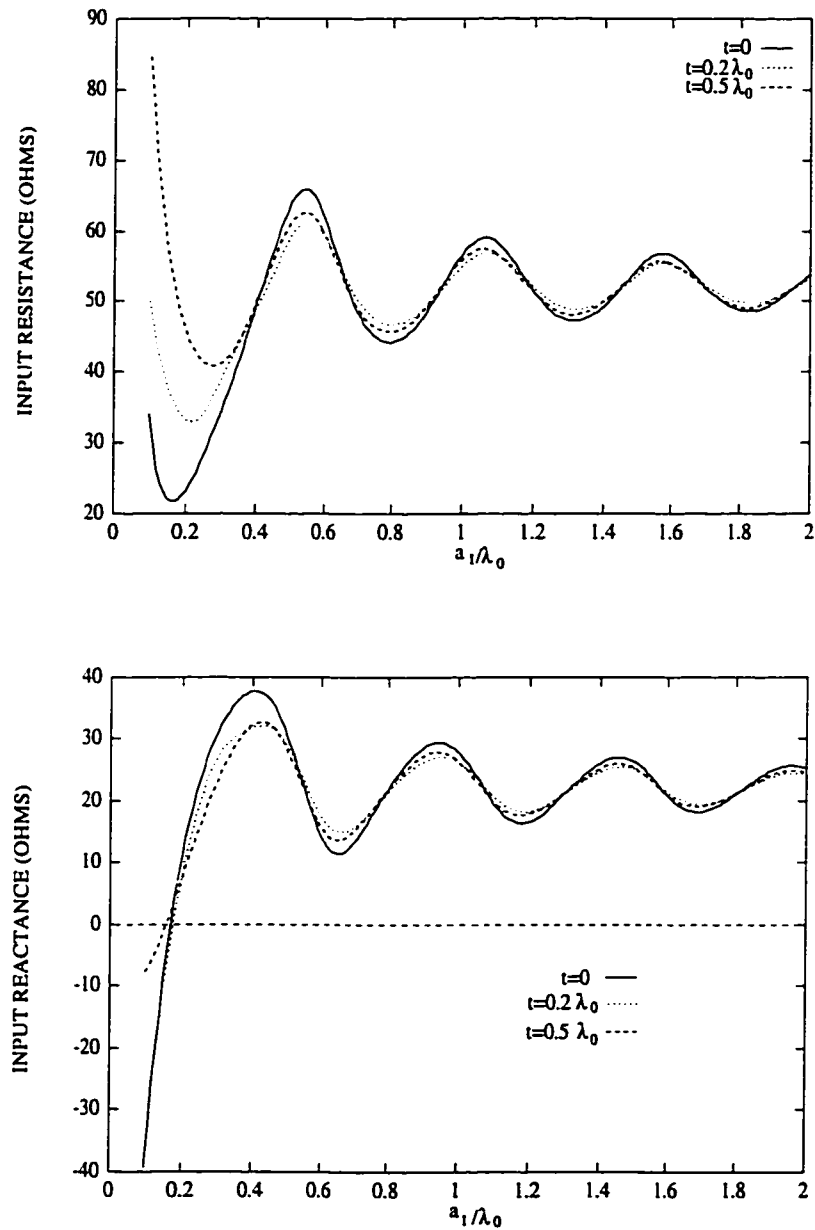


Figure 3.39: Impedance of a monopole as a function of a_1/λ_0 with its thickness as a parameter (same parameters as Figure 3.37).

Chapter 4

Theoretical Formulation for Circular Microstrip Antennas

This chapter presents a general formulation for analyzing single and stacked microstrip patch antennas with circular geometries. Similar to the basic idea used for modeling the monopole antennas in Chapter 2, an outer cylindrical wall is introduced to enclose the patch antenna. It is expected that the assumed cylindrical wall will not have significant effect on the antenna's impedance computation. After assuming this enclosure cylinder, the open-region antenna problem is again transformed into a "closed-region" waveguide junction cascading problem, which is then solved by the modal-expansion method. In order to facilitate the formulation and save computation time involved in the waveguide modal expansion analysis, two useful techniques are introduced in the first two sections of this chapter. The first technique is an improved formulation for waveguide cascaded junctions; while the other is for calculating the reflection coefficient of open-ended waveguides. After introducing these two techniques, a detailed formulation for the analysis of a gen-

eral circular microstrip antenna is presented in Section 4.3. Considered in this category of circular microstrip antennas are: single circular patch fed by a centered or an off-centered coaxial cable, single annular-ring microstrip antenna, an annular-ring-loaded circular patch antenna, and a stacked circular disk antenna. Numerical results for all these practical microstrip antenna structures will be given in the next chapter to demonstrate the versatility and accuracy of this waveguide modal expansion technique.

4.1 New Formulation for Cascaded Junctions

This section introduces an improved modal expansion method for cascaded waveguide junctions. The basic idea is to consider the two junctions *at once* by the modal expansion method, which directly yields the overall scattering matrix for the whole cascaded network. This improved scattering matrix formulation is formally exact and completely eliminates the numerical overflow problem [69], [70], from which the transmission matrix formulation suffers and can also avoid the inversion of two matrices.

There are basically three types of two cascaded waveguide junctions, as elucidated in Figure 4.1. The following subsection will give the detailed formulation for the first type of connection between two waveguide junctions (one is enlargement and the other is reduction). Derived formulas for this type of connection will be employed in the analysis of circular microstrip patch antennas. Sample numerical tests will also be provided for this type to show the great reduction in computer time and memory gained by this improved formulation. Application of this formulation to the analysis of waveguide cavity filters is demonstrated in [66]. The derived expressions for the other two types of cascaded junctions will be given in

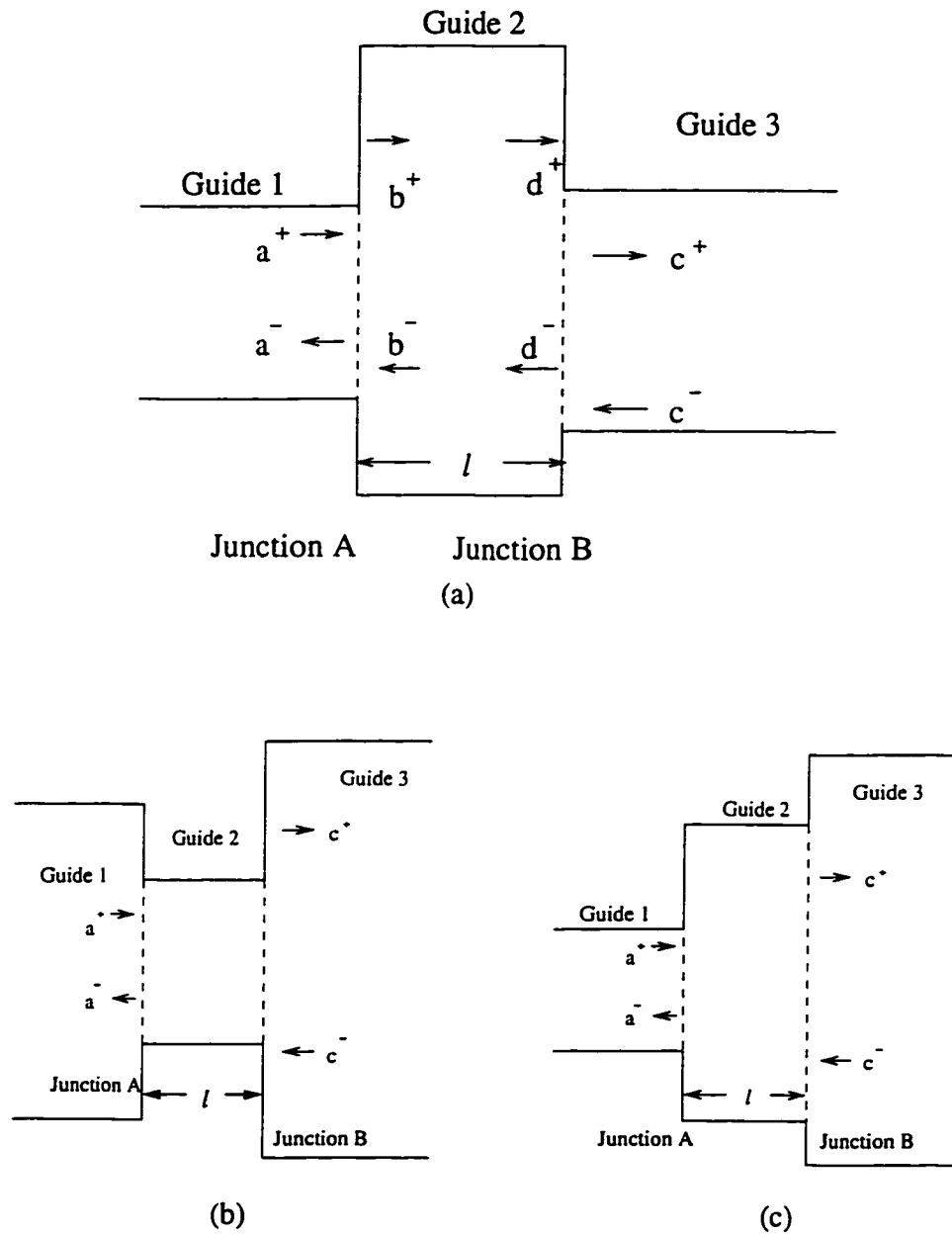


Figure 4.1: Three types of two cascaded waveguide junctions.

the second subsection.

4.1.1 Enlargement-Reduction Cascaded Junctions

As illustrated in Figure 4.1(a), the length of the sandwiched large waveguide is assumed to be l . a^+ and a^- are the incident and reflected modal amplitude column vectors in Guide 1 at Junction A, and similarly c^+ and c^- are the incident and reflected modal amplitude vectors in Guide 3 at Junction B. b^+ , b^- , d^+ , and d^- are defined in the same way for Guide 2. Application of the boundary conditions for tangential electric and magnetic fields at the interfaces of Junction A yields:

$$b^+ + b^- = \mathbf{M}_1(a^+ + a^-) \quad (4.1)$$

$$\mathbf{Y}_1(a^+ - a^-) = \mathbf{M}_1^T \mathbf{Y}_2(b^+ - b^-) \quad (4.2)$$

where \mathbf{Y}_i , for $i = 1, 2$, and 3 , is the modal admittance matrix for the i th waveguide. \mathbf{M}_1 is the E -field mode-matching matrix of Junction A [66], whose size is of N_2 by N_1 , where N_1 and N_2 are the numbers of modes considered in Guides 1 and Guide 2, respectively. Similar operation for Junction B leads to

$$d^+ + d^- = \mathbf{M}_2(c^+ + c^-) \quad (4.3)$$

$$\mathbf{Y}_3(c^+ - c^-) = \mathbf{M}_2^T \mathbf{Y}_2(d^+ - d^-) \quad (4.4)$$

where \mathbf{M}_2 is the E -field mode-matching matrix of Junction B, whose size is of N_2 by N_3 , where N_3 is the number of modes considered in Guide 3. From Fig.4.1(a), we know that $d^+ = \mathbf{L}b^+$ and $b^- = \mathbf{L}d^-$, where \mathbf{L} is the diagonal transmission matrix of the sandwiched large waveguide with $L_{n,n} = \exp(-j\beta_{2,n}l)$ as its n -th diagonal element. Here $\beta_{2,n}$ is the propagation constant of the n -th mode in Guide

2. Substituting these relations into (4.1)-(4.4), and eliminating b^+ , b^- , d^+ , and d^- , one can obtain

$$\mathbf{Y}_1(a^+ - a^-) = -\mathbf{Y}_p(a^+ + a^-) + \mathbf{Y}_q(c^+ + c^-) \quad (4.5)$$

$$\mathbf{Y}_3(c^+ - c^-) = -\mathbf{Y}_q^T(a^+ + a^-) + \mathbf{Y}_s(c^+ + c^-) \quad (4.6)$$

where

$$\begin{aligned} \mathbf{Y}_p &= \mathbf{M}_1^T \mathbf{D}_1 \mathbf{M}_1, & \mathbf{Y}_q &= \mathbf{M}_1^T \mathbf{D}_2 \mathbf{M}_2, & \mathbf{Y}_s &= \mathbf{M}_2^T \mathbf{D}_2 \mathbf{M}_2, \\ \mathbf{D}_1 &= \mathbf{Y}_2(\mathbf{L}^2 + \mathbf{I})(\mathbf{L}^2 - \mathbf{I})^{-1}, & \mathbf{D}_2 &= 2\mathbf{Y}_2\mathbf{L}(\mathbf{L}^2 - \mathbf{I})^{-1}. \end{aligned} \quad (4.7)$$

where \mathbf{D}_1 and \mathbf{D}_2 are diagonal matrices with imaginary elements for lossless waveguides. Therefore, the right-hand sides of (4.7) may be put into single summation form. Matrices \mathbf{Y}_p and \mathbf{Y}_s are symmetric. The expressions (4.5) and (4.6) for this enlargement-reduction type (Figure 4.1(a)) of cascaded waveguide junctions will be used in the formulation for circular micorstrip antennas. From (4.5) and (4.6) and after some manipulation, we can derive the overall scattering matrices of the two cascaded junctions as follows

$$\mathbf{S}_{11} = 2 \left[\mathbf{Y}_1 - \mathbf{Y}_p + \mathbf{Y}_q(\mathbf{Y}_s - \mathbf{Y}_3)^{-1} \mathbf{Y}_q^T \right]^{-1} \mathbf{Y}_1 - \mathbf{I} \quad (4.8)$$

$$\mathbf{S}_{21} = (\mathbf{Y}_s - \mathbf{Y}_3)^{-1} \mathbf{Y}_q^T (\mathbf{I} + \mathbf{S}_{11}) \quad (4.9)$$

$$\mathbf{S}_{12} = \mathbf{Y}_1^{-1} \mathbf{S}_{21}^T \mathbf{Y}_3 \quad (4.10)$$

$$\mathbf{S}_{22} = (\mathbf{Y}_s - \mathbf{Y}_3)^{-1} (\mathbf{Y}_q^T \mathbf{S}_{12} - 2\mathbf{Y}_3) - \mathbf{I}. \quad (4.11)$$

It is noted that only *two small matrices* of sizes N_1 by N_1 and N_3 by N_3 need to be inverted. Compared with the traditional generalized scattering matrix technique [59] for the problem considered here, we can see that it not only reduces the number of matrix inversions (from inverting four matrices to inverting two matrices), but also avoids the inversion of two large matrices of size N_2 by N_2 . In some cases when

the ratios of areas of Guide 2 to that of Guide 1 and Guide 2 to Guide 3 are very large [59], [66], we should take N_2 to be very large to get a convergent solution.

Table 4.1: Comparison of computation time of our improved formulation and the generalized scattering matrix technique ($f = 11GHz$, $l = 15mm$).

Number of modes		Computation time (seconds)	
N_1 for iris guide	N_2 for Guide 2	Our method	GSMT
20	20	0.036	0.060
20	42	0.042	0.138
20	72	0.057	0.379
20	110	0.064	1.006
20	156	0.079	3.062
20	210	0.097	9.210
20	272	0.111	20.34
20	342	0.141	
20	420	0.164	
20	930	0.382	
20	1640	0.622	

To compare our improved modal-expansion method with the traditional generalized scattering matrix technique, we consider a waveguide filter consisting of only one rectangular cavity. It is well known that for a junction between two waveguides, one should take many more modes in the larger waveguide into account when the area ratio of the larger waveguide to the smaller one is very large. As for the problem of a waveguide cavity filter, the smaller the size of the iris waveguide, the larger will be the number of modes in the larger waveguide. We may fix the size

of the iris waveguide and compare the computation time for different number of modes considered in the larger waveguide.

Table 4.1 shows the comparison of computation time for a single-cavity rectangular waveguide filter by our new formulation and the generalized scattering matrices technique [59]. The waveguide is standard WR90 (X-band, $a = 22.86mm$, $b = 10.16mm$) and the central rectangular iris waveguide ($a_1 = 3.86mm$, $b_1 = 1.66mm$, $t = 0.1mm$) has 2.76 percent of its cross-section area. When the number N_2 of modes considered in the larger waveguide increases, the computation time of the traditional GSMT increases dramatically since the number of multiplication operations involved in LU factorization of a matrix is proportional to the cube of its size. For our improved formulation, however, the computation time increase is less than linear with respect to N_2 . Moreover, there is a great reduction in computer memory requirements in our new method. For the traditional GSMT it was impossible to carry out the calculations when N_2 was more than 300 due to huge consumption of computer memory while our improved method easily treated more than 1000 modes.

4.1.2 Derived Expressions for the Other Two Types

Following the same procedures as introduced in the previous subsection for the enlargement-reduction type (Figure 4.1(a)) of cascaded junctions, one can derive the following expressions for the other two types of cascaded waveguide junctions.

For the second type (Figure 4.1(b)), we get:

$$\mathbf{S}_{11} = 2\mathbf{M}_1 \mathbf{Y}_p^T \mathbf{Y}_{L2} \mathbf{Y}_2^{-1} \mathbf{L}^{-1} (\mathbf{I} - \mathbf{L}^2) \mathbf{M}_1^T \mathbf{Y}_1 - \mathbf{I} \quad (4.12)$$

$$\mathbf{S}_{12} = 4\mathbf{M}_1 \mathbf{Y}_p^T \mathbf{M}_2^T \mathbf{Y}_3 \quad (4.13)$$

$$\mathbf{S}_{21} = \mathbf{Y}_3^{-1} \mathbf{S}_{12}^T \mathbf{Y}_1 \quad (4.14)$$

$$\mathbf{S}_{22} = 2\mathbf{M}_2 \mathbf{Y}_p \mathbf{Y}_{L1} \mathbf{Y}_2^{-1} \mathbf{L}^{-1} (\mathbf{I} - \mathbf{L}^2) \mathbf{M}_2^T \mathbf{Y}_3 - \mathbf{I} \quad (4.15)$$

where

$$\mathbf{Y}_p = \left[\mathbf{Y}_{L1} \mathbf{Y}_2^{-1} \mathbf{L}^{-1} (\mathbf{I} - \mathbf{L}^2) \mathbf{Y}_{L2} - 4\mathbf{Y}_2 \mathbf{L} (\mathbf{I} - \mathbf{L}^2)^{-1} \right]^{-1} \quad (4.16)$$

$$\mathbf{Y}_{L1} = \mathbf{M}_1^T \mathbf{Y}_1 \mathbf{M}_1 + \mathbf{Y}_2 (\mathbf{I} + \mathbf{L}^2) (\mathbf{I} - \mathbf{L}^2)^{-1} \quad (4.17)$$

$$\mathbf{Y}_{L2} = \mathbf{M}_2^T \mathbf{Y}_3 \mathbf{M}_2 + \mathbf{Y}_2 (\mathbf{I} + \mathbf{L}^2) (\mathbf{I} - \mathbf{L}^2)^{-1}. \quad (4.18)$$

It should be noted that only one matrix $\mathbf{Y}_{L1} \mathbf{Y}_2^{-1} \mathbf{L}^{-1} (\mathbf{I} - \mathbf{L}^2) \mathbf{Y}_{L2} - 4\mathbf{Y}_2 \mathbf{L} (\mathbf{I} - \mathbf{L}^2)^{-1}$ needs to be inverted to obtain the overall scattering matrices of two cascaded junctions of this type. A waveguide with a thin or thick diaphragm belongs to this type of connection, which has been widely used in waveguide cavity filters.

For the third type (Figure 4.1(c)), we derive the following scattering submatrices for these cascaded junctions:

$$\mathbf{S}_{11} = 2 \left[\mathbf{I} + \mathbf{Y}_1^{-1} \mathbf{Y}_{L1} - 2\mathbf{Y}_1^{-1} \mathbf{M}_1^T \mathbf{Y}_2 \mathbf{L} \mathbf{Y}_p \right]^{-1} - \mathbf{I} \quad (4.19)$$

$$\mathbf{S}_{21} = \mathbf{M}_2 \left[\mathbf{L} \mathbf{M}_1 + (\mathbf{I} - \mathbf{L}^2) \mathbf{Y}_p \right] (\mathbf{I} + \mathbf{S}_{11}) \quad (4.20)$$

$$\mathbf{S}_{12} = (\mathbf{I} + \mathbf{S}_{11}) \mathbf{Y}_1^{-1} \mathbf{M}_1^T \mathbf{Y}_2 \mathbf{L} \mathbf{Y}_q \quad (4.21)$$

$$\mathbf{S}_{22} = [\mathbf{S}_{21} \mathbf{Y}_1^{-1} \mathbf{M}_1^T \mathbf{Y}_2 \mathbf{L} + \mathbf{M}_2 (\mathbf{I} - \mathbf{L}^2)] \mathbf{Y}_q - \mathbf{I} \quad (4.22)$$

where

$$\mathbf{Y}_p = \left[(\mathbf{Y}_2 (\mathbf{I} + \mathbf{L}^2) + \mathbf{Y}_{L2}) (\mathbf{I} - \mathbf{L}^2) \right]^{-1} (\mathbf{Y}_2 - \mathbf{Y}_{L2}) \mathbf{L} \mathbf{M}_1 \quad (4.23)$$

$$\mathbf{Y}_q = 2 \left[(\mathbf{Y}_2 (\mathbf{I} + \mathbf{L}^2) + \mathbf{Y}_{L2}) (\mathbf{I} - \mathbf{L}^2) \right]^{-1} \mathbf{M}_2^T \mathbf{Y}_3 \quad (4.24)$$

$$\mathbf{Y}_{L1} = \mathbf{M}_1^T \mathbf{Y}_2 \mathbf{M}_1, \quad \mathbf{Y}_{L2} = \mathbf{M}_2^T \mathbf{Y}_3 \mathbf{M}_2. \quad (4.25)$$

It is seen that only two matrices need to be inverted to obtain the overall scattering matrices of two cascaded junctions of this type.

4.2 Simple Analysis of Open-Ended Waveguides

This section introduces a simple technique for calculation of the reflection coefficient of open-ended waveguides. The method is called the “complexification and extrapolation” [65] technique. Open-ended waveguides themselves have found wide applications in aeronautics, large phased array systems, thermography, diathermy and hyperthermia, and the measurement of material properties, etc. Theoretical and experimental studies of open-ended waveguides have occupied the attention of numerous researchers for several decades [71]. Variational method [72] and mode-matching techniques such as the correlation matrix method [73], Green’s function method [74], the transverse operator method [75], and the method of moments [76] were employed to compute the aperture admittance of open-ended coaxial line and rectangular waveguide with infinite flange.

This section presents a conceptually simple, numerically efficient and accurate method for calculating the reflection coefficient of open-ended waveguides. The idea of this method is as follows. Firstly, a large waveguide is introduced to approximate the half-space. As pointed out in [77] the size of this assumed waveguide should be very large when the medium in the half space is low-loss or lossless, which results in expensive computational effort since we must take a very large number of modes in the large waveguide into account to ensure convergent results. In order to overcome this drawback and to reduce the size of the introduced waveguide to save computer time, it is assumed to be filled with a homogeneous moderately lossy medium. The numerical results for lossy dielectric are then employed to calculate the solution to the actual lossless or low-loss half-space problem by an extrapolation technique [65].

Figure 4.2(a) shows the side view of an open-ended waveguide with an infinite

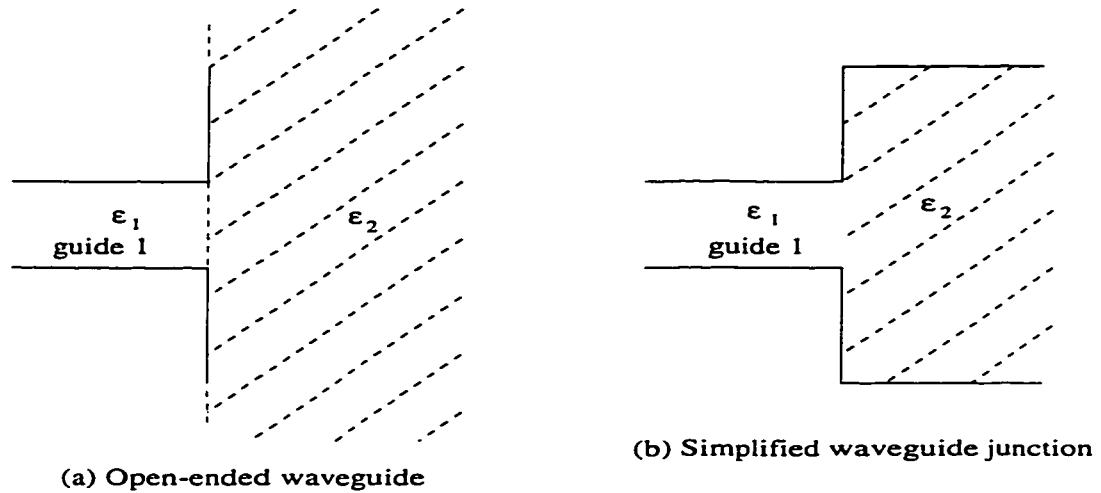


Figure 4.2: Side-view of an open-ended waveguide and its simplified waveguide junction model.

conducting flange, where the cross-section of the waveguide can be arbitrary. At first, we introduce a large waveguide to approximate the half space. Then the problem considered reduces to that of a waveguide junction as illustrated in Figure 4.2(b). The cross-section of the postulated large waveguide should be the same as or similar to that of the input waveguide (guide 1 in Figure 4.2) to simplify the analysis of the related waveguide junction. Meanwhile, symmetry may also be taken into account to reduce the computational complexity.

After obtaining the reflection coefficient or aperture admittance data for the waveguide junction for several different values of dielectric loss tangent, say three different values of loss tangent, an extrapolation technique (parabolic extrapolation) is employed to calculate the solution to the lossless or low-loss half-space problem in the following way. Suppose the imaginary parts of three complexified ϵ_{r2} values are ϵ''_{r21} , ϵ''_{r22} , and ϵ''_{r23} and the corresponding reflection coefficients are Γ_1 , Γ_2 , and Γ_3 , respectively. We compute the quadratic Lagrange interpolation polynomial through

the points $(\epsilon''_{r21}, \Gamma_1)$, $(\epsilon''_{r22}, \Gamma_2)$, and $(\epsilon''_{r23}, \Gamma_3)$ as follows:

$$\Gamma(\epsilon''_{r2}) = \frac{p_1 \Gamma_1 + p_2 \Gamma_2 + p_3 \Gamma_3}{(\epsilon''_{r21} - \epsilon''_{r22})(\epsilon''_{r22} - \epsilon''_{r23})(\epsilon''_{r21} - \epsilon''_{r23})} \quad (4.26)$$

where

$$p_1 = (\epsilon''_{r22} - \epsilon''_{r23})(\epsilon''_{r2} - \epsilon''_{r22})(\epsilon''_{r2} - \epsilon''_{r23})$$

$$p_2 = (\epsilon''_{r23} - \epsilon''_{r21})(\epsilon''_{r2} - \epsilon''_{r21})(\epsilon''_{r2} - \epsilon''_{r23})$$

$$p_3 = (\epsilon''_{r21} - \epsilon''_{r22})(\epsilon''_{r2} - \epsilon''_{r21})(\epsilon''_{r2} - \epsilon''_{r22})$$

and then set ϵ''_{r2} equal to zero, or to the actual small loss tangent, to yield the desired reflection coefficient of a waveguide terminated by an infinite flange.

Figure 4.3 shows the variation of the reflection coefficient of an open-ended coaxial line with infinite flange with respect to the radius b_2 of the large waveguide for different values of loss tangent. The inner and outer radii of the coaxial line are $a_1 = 1.4364mm$ and $b_1 = 4.725mm$. It is seen that the lower the loss tangent of the medium retained in the large waveguide the larger is its size to obtain convergent results. For the very lossy medium, for example, $\epsilon_{r2} = 2.05 - j$, the result obtained with $b_2/b_1 = 7$ is quite satisfactory, The number of modes assumed in the large waveguide depends on the size of the waveguide according to the relation $N_2 = N_1 b_2 / (b_1 - a_1)$, where N_1 and N_2 are the numbers of modes considered in the input coaxial and large circular waveguides. Results presented in Figure 4.3 are obtained by fixing $N_1 = 10$ (the dominant TEM mode plus 9 TM_{0n} modes).

Figure 4.4 shows the comparison of results obtained by our proposed method and data given in [74] for the reflection coefficients of an open-ended coaxial line. It is seen that the agreement is excellent. The results shown in Figure 4.4 are obtained by extrapolating three values of the reflection coefficient for $\epsilon_{r2} = 2.05 - j0.2$, $\epsilon_{r2} = 2.05 - j0.4$, and $\epsilon_{r2} = 2.05 - j0.6$ back to the real axis of the relative permittivity ϵ_{r2} .

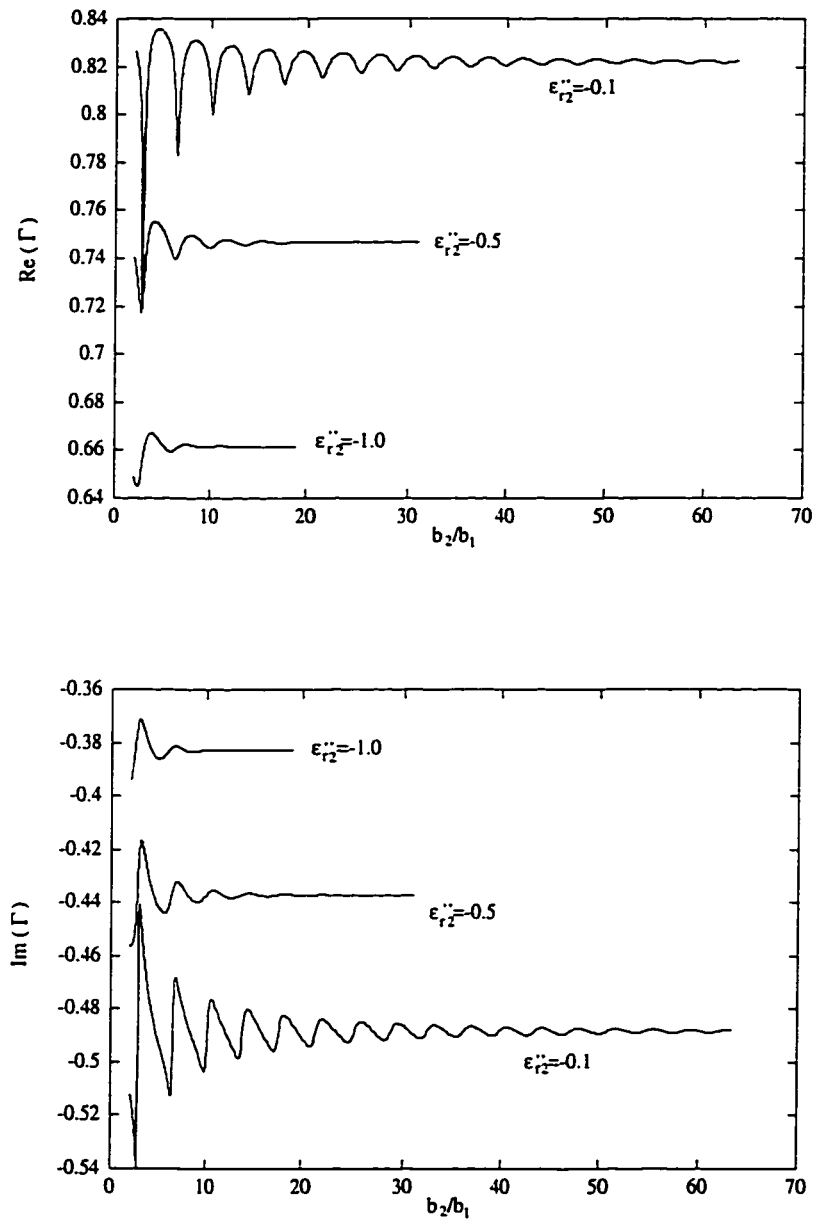


Figure 4.3: Variation of the reflection coefficient of an open-ended coaxial line with respect to the radius of the large circular waveguide for different values of loss tangent ($f = 6GHz$).

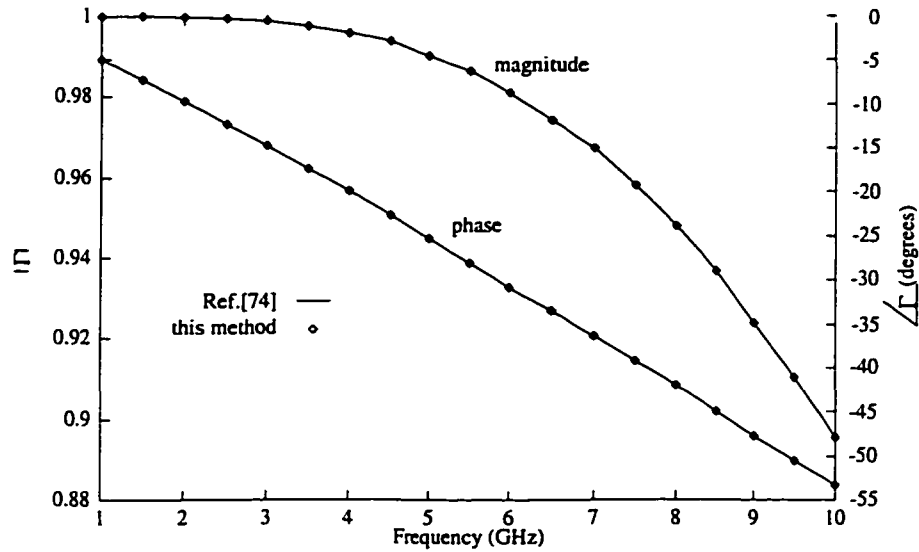


Figure 4.4: Magnitude and phase of the reflection coefficient of a coaxial line terminated by an infinite flange ($a_1 = 1.4364mm$, $b_1 = 4.725mm$, $\epsilon_{r1} = \epsilon_{r2} = 2.05$).

The effect of different reference data used for extrapolation on the resultant reflection coefficient is examined in Table 4.2, where the results, obtained by extrapolating three groups of data, are compared. We can see that the maximum error between the results for Case 1 and Case 2 is less than 0.1%, and the maximum difference of the absolute values of the reflection coefficients between Case 1 and Case 3 is less than 1%. The loss tangents assumed in Case 3 are quite big, which makes the size of the large circular waveguide only about ten times that of the coaxial line, while the accuracy of the resultant reflection coefficient is still quite satisfactory. This shows that the method described in this section is computationally efficient, very easy to implement and also very accurate for the open-ended waveguide problems.

Before concluding this section, we present some results for the aperture admittance of an open-ended rectangular waveguide with infinite flange. For this

Table 4.2: Magnitude and phase of the reflection coefficient of an open-ended coaxial line with infinite flange. Case 1: using $\epsilon''_{r2} = -0.1, -0.2, -0.3$ three points for extrapolation; Case 2: using $\epsilon''_{r2} = -0.2, -0.4, -0.6$ three points; Case 3: using $\epsilon''_{r2} = -0.5, -1.0, -1.5$ three points

Frequency GHz	Magnitude			Phase (degrees)		
	Case 1	Case 2	Case 3	Case 1	Case 2	Case 3
1.0	0.99997	0.99998	1.00003	-4.8692	-4.8689	-4.8663
2.0	0.99976	0.99972	0.99972	-9.8005	-9.7978	-9.7921
3.0	0.99874	0.99860	0.99840	-14.812	-14.834	-14.827
4.0	0.99570	0.99568	0.99508	-20.000	-20.012	-20.004
5.0	0.98984	0.98997	0.98868	-25.344	-25.344	-25.331
5.5	0.98604	0.98576	0.98402	-28.057	-28.064	-28.048
6.0	0.98062	0.98049	0.97824	-30.829	-30.817	-30.796
6.5	0.97420	0.97408	0.97128	-33.590	-33.597	-33.570
7.0	0.96685	0.96646	0.96308	-36.405	-36.400	-36.365
7.5	0.95779	0.95760	0.95362	-39.226	-39.219	-39.175
8.0	0.94786	0.94747	0.94292	-42.048	-42.048	-41.994
8.5	0.93651	0.93609	0.93098	-44.892	-44.881	-44.815
9.0	0.92387	0.92350	0.91787	-47.716	-47.710	-47.633
9.5	0.91025	0.90973	0.90365	-50.538	-50.530	-50.440
10.0	0.89534	0.89487	0.88841	-53.346	-53.333	-53.233

problem the introduced large waveguide is assumed to be of rectangular shape and collinear with the input waveguide. The aperture admittance is defined as $Y = G + jB = Y_{0,10}(1 - \Gamma_{10})/(1 + \Gamma_{10})$, here $Y_{0,10}$ and Γ_{10} are the characteristic admittance and the reflection coefficient of the dominant TE_{10} mode. In Figure 4.5 our results are compared with available data obtained by the correlation matrix method [73]. Our results shown in Figure 4.5 are obtained by extrapolating three values of the aperture admittance for $\epsilon_{r2} = 1 - j0.1$, $\epsilon_{r2} = 1 - j0.2$, and $\epsilon_{r2} = 1 - j0.3$ to that for real ϵ_{r2} . It is noted that the agreement between them is very good, which also verifies the validity of the method presented here.

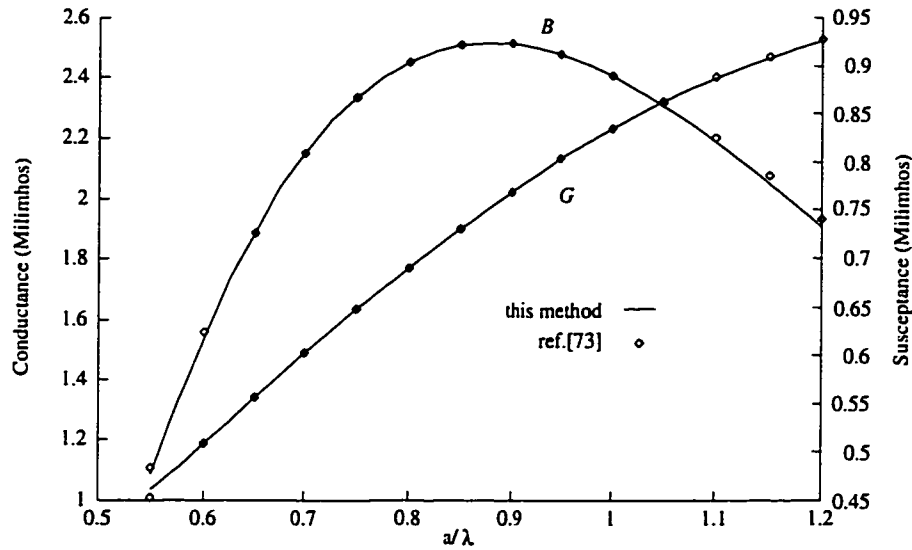


Figure 4.5: Aperture admittance of an open-ended rectangular waveguide with infinite flange ($a = 2.25b$).

The simple and yet efficient technique presented in this section for open-ended waveguides will be used in the analysis of circular microstrip antennas in the next section. In Section 3.5, we already employed this technique to predict the input impedance of a monopole over a finite ground plane.

4.3 General Formulation for Circular Microstrip Antennas

Figure 4.6 shows the side-view of an annular-ring-loaded stacked circular microstrip antenna fed by an off-centered coaxial line [78]. The radius of the driven circular patch is c_1 ; the inner and outer radii of the loading annular-ring are, respectively, d_1 and a_1 . As illustrated in Figure 4.6, the loading annular-ring is located in the same plane as the driven circular patch; their thickness is assumed to be t_1 . The parasitic circular patch is of radius a_2 and of thickness t_2 . The distance between the position of the feeding probe and the circular patch's center is d . The inner and outer radii of the coaxial feed line are a_0 and b_0 , respectively. The uniaxial substrate and superstrate are of thickness h and s_2 , respectively, and are described by the following permittivity and permeability

$$\bar{\epsilon}_i = \epsilon_0 \begin{bmatrix} \epsilon_{i1} & 0 & 0 \\ 0 & \epsilon_{i1} & 0 \\ 0 & 0 & \epsilon_{i2} \end{bmatrix}, \quad \bar{\mu}_i = \mu_0 \begin{bmatrix} \mu_{i1} & 0 & 0 \\ 0 & \mu_{i1} & 0 \\ 0 & 0 & \mu_{i2} \end{bmatrix} \quad (4.27)$$

where $i = b, p$ represents substrate and superstrate, respectively. The sandwiched dielectric is of thickness s_1 and of permittivity $\epsilon_r \epsilon_0$.

The problem shown in Figure 4.6 is quite general and will reduce to many special cases under certain circumstances. With the loading annular-ring removed ($d_1 = c_1$), the structure reduces to a stacked circular microstrip antenna. When $s_1 = t_2 = 0$ and $a_2 = c_1$, the parasitic patch will disappear, and the problem will reduce to an annular-ring-loaded circular microstrip antenna. Similarly, when $s_1 = t_2 = a_2 = c_1 = 0$, the structure will be simplified to an annular-ring microstrip antenna. With both the loading annular-ring and parasitic circular patch removed,

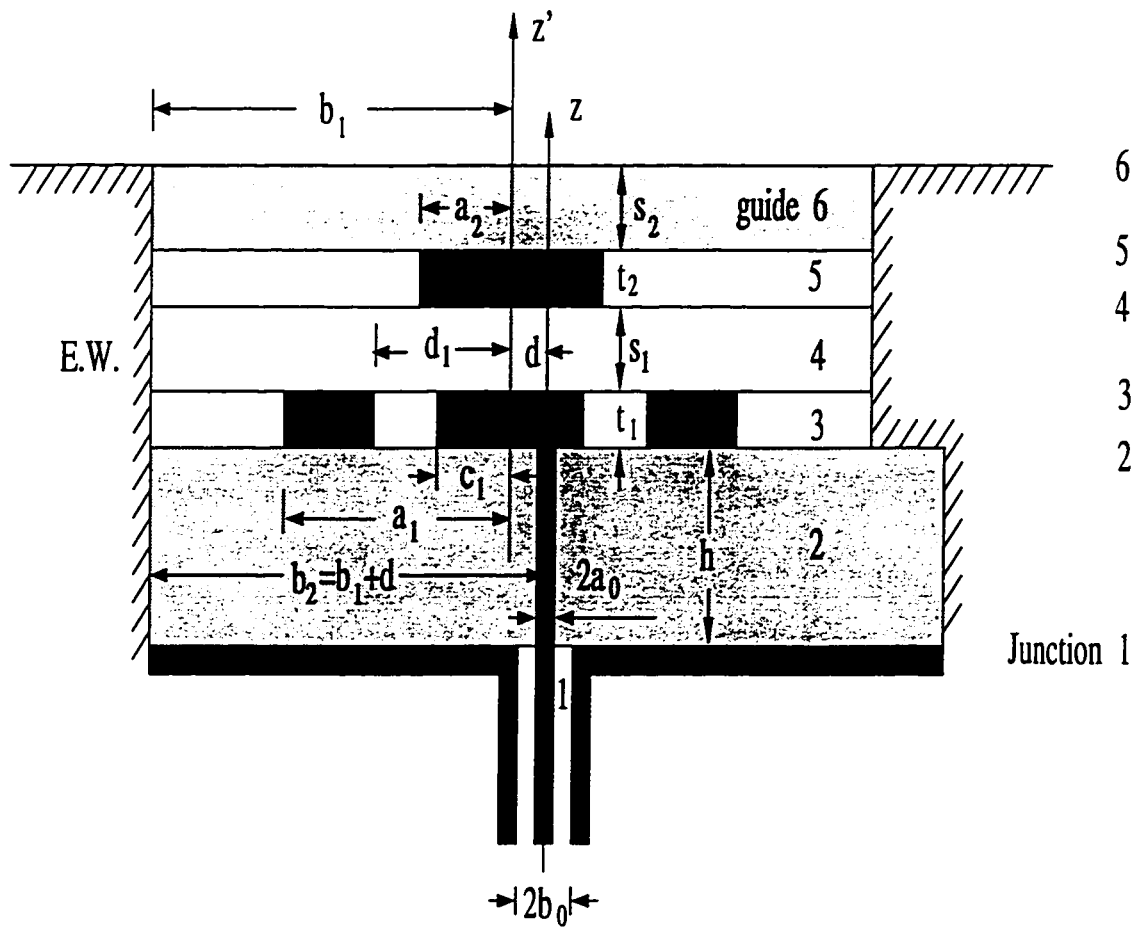


Figure 4.6: Analysis model of an annular-ring-loaded stacked circular microstrip patch antenna.

the structure is simply a circular microstrip antenna on a uniaxial substrate and covered by a uniaxial superstrate. Therefore, all these problems: single and stacked circular patches, annular-ring microstrip, annular-ring-loaded circular microstrip, are included in the present model.

As illustrated in Figure 4.6, the whole antenna structure is enclosed by an assumed outer cylindrical wall, which facilitates the use of the waveguide modal-expansion method. The radius of the assumed outer wall is $b_2 = b_1 + d$ for the substrate waveguide section and b_1 elsewhere. Referring to Figure 4.6, we identify four coaxial waveguides (guides 1,2,3, and 5) and two circular waveguides (guides 4 and 6). The third waveguide is, in fact, a compound waveguide which is comprised of two coaxial waveguides; their inner and outer radii are, respectively, a_1 and b_1 , and c_1 and d_1 . There are six waveguide junctions involved in the problem, as indicated in Figure 4.6. The first junction is the one between two coaxial waveguides which have the same inner conductor. The second one is the junction between two coaxial waveguides with their axes having a shift d . Junctions 3, 4, and 5 are simply the coaxial-to-circular abrupt discontinuity. The last junction is actually an open-ended circular waveguide with infinite flange and radiating into the half space. The following subsection details the application of CCPT to the resultant waveguide junction cascading problem.

Unlike the symmetrical case of a circular patch antenna fed by a centered coaxial line [79], all the possibly existing modes, including the dominant TEM mode, TE modes and TM modes, can be excited for the problem of a circular or annular-ring patch antenna fed by an off-centered coaxial line. It is well known that the modal functions for a cylindrical waveguide homogeneously filled with uniaxial dielectric are exactly the same as those for the corresponding empty waveguide, while their modal admittances and propagation constants may change. The modal functions

for the transverse electric and magnetic fields in coaxial and circular waveguides are elucidated in Appendix A. For a coaxial waveguide filled with the uniaxial medium characterized by (4.27), the modal admittance is as follows:

$$Y_T = \frac{1}{\eta_0} \sqrt{\epsilon_{i1}/\mu_{i1}} \quad \text{for } TEM \text{ mode} \quad (4.28a)$$

$$Y_{Hn} = \frac{\sqrt{\mu_{i1} k_{hn}^2 / \mu_{i2} - k_0^2 \epsilon_{i1} \mu_{i1}}}{j\omega \mu_0 \mu_{i1}} \quad \text{for } TE \text{ modes} \quad (4.28b)$$

$$Y_{En} = \frac{j\omega \epsilon_0 \epsilon_{i1}}{\sqrt{\epsilon_{i1} k_{en}^2 / \epsilon_{i2} - k_0^2 \epsilon_{i1} \mu_{i1}}} \quad \text{for } TM \text{ modes} \quad (4.28c)$$

where $\eta_0 = \sqrt{\mu_0/\epsilon_0}$, $k_0^2 = \omega^2 \mu_0 \epsilon_0$, k_{hn} and k_{en} are the cutoff wavenumbers of the n -th TE and TM modes in the corresponding empty waveguide, respectively. Similarly, the propagation constants of the modes considered in the coaxial waveguide are

$$\beta_T = k_0 \sqrt{\mu_{i1} \epsilon_{i1}} \quad \text{for } TEM \text{ mode} \quad (4.29a)$$

$$\beta_{Hn} = \sqrt{k_0^2 \epsilon_{i1} \mu_{i1} - \mu_{i1} k_{hn}^2 / \mu_{i2}} \quad \text{for } TE \text{ modes} \quad (4.29b)$$

$$\beta_{En} = \sqrt{k_0^2 \epsilon_{i1} \mu_{i1} - \epsilon_{i1} k_{en}^2 / \epsilon_{i2}} \quad \text{for } TM \text{ modes.} \quad (4.29c)$$

Let \mathbf{A}_1^+ and \mathbf{A}_1^- be the incident and reflected modal amplitude vectors in the first feed waveguide at $z = 0$. The forward- and backward-wave modal amplitude vectors in the sixth circular waveguide at $z = h + t_1 + t_2 + s_1$ are assumed to be \mathbf{A}_6^+ and \mathbf{A}_6^- , respectively. The reflection coefficient matrix Γ_6 at the last open-ended circular waveguide junction is obtained by using the complexification and extrapolation technique [65], [66], which has been introduced in the previous section. Then we have:

$$\mathbf{A}_6^- = \mathbf{L}_6 \Gamma_6 \mathbf{L}_6 \mathbf{A}_6^+ \quad (4.30)$$

where \mathbf{L}_6 is the diagonal transmission matrix of guide 6 with

$$L_{6,n,n} = \exp(-j\beta_{6,n}s_2) \quad (4.31)$$

as its n -th diagonal element and $\beta_{6,n}$ is the propagation constant of the n -th mode in guide 6.

Let \mathbf{A}_3^+ and \mathbf{A}_3^- be the forward- and backward-wave modal amplitude vectors in the third compound waveguide at $z = h$, and \mathbf{A}_5^+ and \mathbf{A}_5^- be the forward- and backward-wave modal amplitude vectors in the fifth coaxial waveguide at $z = h + t_1 + s_1$. Application of the CCPT [67] and the improved modal expansion formulation for cascaded junctions [66] to junctions 1, 2, 3, and 4 yields

$$\mathbf{Y}_1(\mathbf{A}_1^+ - \mathbf{A}_1^-) = -\mathbf{Y}_o(\mathbf{A}_1^+ + \mathbf{A}_1^-) + \mathbf{Y}_p(\mathbf{A}_3^+ + \mathbf{A}_3^-) \quad (4.32)$$

$$\mathbf{Y}_3(\mathbf{A}_3^+ - \mathbf{A}_3^-) = -\mathbf{Y}_p^T(\mathbf{A}_1^+ + \mathbf{A}_1^-) + \mathbf{Y}_q(\mathbf{A}_3^+ + \mathbf{A}_3^-) \quad (4.33)$$

$$\mathbf{Y}_3(\mathbf{L}_3\mathbf{A}_3^+ - \mathbf{L}_3^{-1}\mathbf{A}_3^-) = -\mathbf{Y}_r(\mathbf{L}_3\mathbf{A}_3^+ + \mathbf{L}_3^{-1}\mathbf{A}_3^-) + \mathbf{Y}_s(\mathbf{A}_5^+ + \mathbf{A}_5^-) \quad (4.34)$$

$$\mathbf{Y}_5(\mathbf{A}_5^+ - \mathbf{A}_5^-) = -\mathbf{Y}_s^T(\mathbf{L}_3\mathbf{A}_3^+ + \mathbf{L}_3^{-1}\mathbf{A}_3^-) + \mathbf{Y}_t(\mathbf{A}_5^+ + \mathbf{A}_5^-) \quad (4.35)$$

where

$$\mathbf{Y}_o = \mathbf{M}_{21}^T \mathbf{R}_1 \mathbf{M}_{21}, \quad \mathbf{Y}_p = \mathbf{M}_{21}^T \mathbf{R}_2 \mathbf{M}_{23}, \quad \mathbf{Y}_q = \mathbf{M}_{23}^T \mathbf{R}_1 \mathbf{M}_{23} \quad (4.36)$$

$$\mathbf{Y}_r = \mathbf{M}_{43}^T \mathbf{R}_3 \mathbf{M}_{43}, \quad \mathbf{Y}_s = \mathbf{M}_{43}^T \mathbf{R}_4 \mathbf{M}_{45}, \quad \mathbf{Y}_t = \mathbf{M}_{45}^T \mathbf{R}_3 \mathbf{M}_{45} \quad (4.37)$$

$$\mathbf{R}_1 = \mathbf{Y}_2(\mathbf{L}_2^2 + \mathbf{I})(\mathbf{L}_2^2 - \mathbf{I})^{-1}, \quad \mathbf{R}_2 = 2\mathbf{Y}_2\mathbf{L}_2(\mathbf{L}_2^2 - \mathbf{I})^{-1} \quad (4.38)$$

$$\mathbf{R}_3 = \mathbf{Y}_4(\mathbf{L}_4^2 + \mathbf{I})(\mathbf{L}_4^2 - \mathbf{I})^{-1}, \quad \mathbf{R}_4 = 2\mathbf{Y}_4\mathbf{L}_4(\mathbf{L}_4^2 - \mathbf{I})^{-1} \quad (4.39)$$

and \mathbf{Y}_i for $i = 1, 2, 3, 4, 5$, and 6, is the modal admittance matrix for the i -th waveguide. \mathbf{L}_i for $i = 2, 3, 4, 5$, is the diagonal transmission matrix of the i -th waveguide and is defined in a similar way as (4.31). The superscript T denotes the transpose operation. $\mathbf{M}_{i,j}$ for $i = 2, 4$ and $j = 1, 3, 5$, is the E-field mode-matching matrix [67], [80] for the junction between guide i and guide j . \mathbf{M}_{21} , \mathbf{M}_{43} , and \mathbf{M}_{45} can be easily derived, while \mathbf{M}_{23} for the second junction is obtained with an aid of a coordinate transformation. The addition theorem for cylindrical functions [56]

is employed to realize the transformation and to get the closed-form expression of \mathbf{M}_{23} . Appendix B elucidates all the needed E-field mode-matching matrices.

Application of the CCPT [67] to Junction 5 leads to

$$\mathbf{A}_6^+ + \mathbf{A}_6^- = \mathbf{M}_{65}(\mathbf{L}_5\mathbf{A}_5^+ + \mathbf{L}_5^{-1}\mathbf{A}_5^-) \quad (4.40)$$

$$\mathbf{Y}_5(\mathbf{L}_5\mathbf{A}_5^+ - \mathbf{L}_5^{-1}\mathbf{A}_5^-) = \mathbf{M}_{65}^T\mathbf{Y}_6(\mathbf{A}_6^+ - \mathbf{A}_6^-) \quad (4.41)$$

where \mathbf{M}_{65} is the E-field mode-matching matrix [67], [80] for a coaxial-to-circular waveguide junction (refer to Appendix B for derived expressions). Use of (4.30), (4.32)-(4.35), (4.40), and (4.41) results in the following results after some manipulations.

$$\mathbf{A}_1^- = \mathbf{S}_{11}\mathbf{A}_1^+ \quad (4.42)$$

$$\mathbf{A}_6^+ = \mathbf{T}_{61}\mathbf{A}_1^+ \quad (4.43)$$

where

$$\mathbf{S}_{11} = 2\mathbf{Y}_F - \mathbf{I} = 2(\mathbf{I} + \mathbf{Y}_1^{-1}\mathbf{Y}_{L1})^{-1} - \mathbf{I} \quad (4.44)$$

$$\mathbf{T}_{61} = 8\mathbf{Y}_A\mathbf{Y}_D\mathbf{L}_5\mathbf{Y}_B\mathbf{Y}_E\mathbf{L}_3\mathbf{Y}_C\mathbf{Y}_F \quad (4.45)$$

$$\mathbf{Y}_{L1} = -\mathbf{Y}_o - \mathbf{Y}_p(\mathbf{I} + \mathbf{\Gamma}_3)\mathbf{Y}_C \quad (4.46)$$

$$\mathbf{Y}_C = [\mathbf{Y}_3(\mathbf{I} - \mathbf{\Gamma}_3) - \mathbf{Y}_q(\mathbf{I} + \mathbf{\Gamma}_3)]^{-1}\mathbf{Y}_p^T \quad (4.47)$$

$$\mathbf{Y}_E = (\mathbf{I} + \mathbf{Y}_3^{-1}\mathbf{Y}_{L3})^{-1}, \quad \mathbf{\Gamma}_3 = \mathbf{L}_3[2\mathbf{Y}_E - \mathbf{I}]\mathbf{L}_3 \quad (4.48)$$

$$\mathbf{Y}_{L3} = -\mathbf{Y}_r - \mathbf{Y}_s(\mathbf{I} + \mathbf{\Gamma}_5)\mathbf{Y}_B \quad (4.49)$$

$$\mathbf{Y}_B = [\mathbf{Y}_5(\mathbf{I} - \mathbf{\Gamma}_5) - \mathbf{Y}_t(\mathbf{I} + \mathbf{\Gamma}_5)]^{-1}\mathbf{Y}_s^T \quad (4.50)$$

$$\mathbf{Y}_D = (\mathbf{I} + \mathbf{Y}_5^{-1}\mathbf{Y}_{L5})^{-1} \quad (4.51)$$

$$\mathbf{\Gamma}_5 = \mathbf{L}_5[2\mathbf{Y}_D - \mathbf{I}]\mathbf{L}_5 \quad (4.52)$$

$$\mathbf{Y}_A = (\mathbf{I} + \mathbf{L}_6\mathbf{\Gamma}_6\mathbf{L}_6)^{-1}\mathbf{M}_{65} \quad (4.53)$$

$$\mathbf{Y}_{L5} = \mathbf{M}_{65}^T \mathbf{Y}_6 (\mathbf{I} - \mathbf{L}_6 \mathbf{\Gamma}_6 \mathbf{L}_6) \mathbf{Y}_A \quad (4.54).$$

From (4.42), (4.43) and (4.30) one can calculate the reflected modal amplitude vector \mathbf{A}_1^- in the feed waveguide and the forward and backward modal amplitude vectors \mathbf{A}_6^+ and \mathbf{A}_6^- in the last circular waveguide when the incident modal amplitude \mathbf{A}_1^+ is given (for example, $(1, 0, \dots, 0)^T$). From (4.39) one can extract the reflection coefficient S_{110} for the dominant TEM mode in the coaxial feed waveguide. Then the input impedance of the microstrip antenna is

$$Z_{in} = Z_{10} \frac{1 + S_{110}}{1 - S_{110}} \quad (4.55)$$

where Z_{10} is the incident TEM mode's impedance.

To calculate the far-region radiated field pattern of the circular patch antenna, the electric field components on the aperture at $z = h + t_1 + t_2 + s_1 + s_2$, which are related to the equivalent magnetic surface currents, need to be found. From (4.43) and (4.30), we can calculate the amplitude of each mode excited in the last waveguide. Based on this, one is able to determine the surface electric field or magnetic current on the aperture, and then find the far-zone radiated field. The equivalent magnetic current on the circular aperture of radius b_1 is:

$$\vec{M} = \vec{E}_{ap} \times \hat{z} = \sum_{m=1}^{N_6} C_m \vec{e}_{6,m} \times \hat{z} \quad (4.56)$$

where $C_m = L_{6,m} A_{6,m}^+ + L_{6,m}^{-1} A_{6,m}^-$, and N_6 is the number of modes considered in guide 6.

The far-zone radiated field due to the surface magnetic current \vec{M} [57] is

$$\vec{E} = \frac{jk_0 \exp(-jk_0 r)}{2\pi r} \int_{S_a} [\hat{r} \times \vec{M}(\vec{r}')] \exp[jk_0 \rho' \sin \theta \cos(\phi - \phi')] ds' \quad (4.57)$$

where $k_0 = \omega \sqrt{\mu_0 \epsilon_0}$, and $r \gg \rho'$. Substituting (4.56) into (4.57) and using the modal functions for the last circular waveguide [81], one can derive (see Appendix

D for detailed derivation)

$$\begin{aligned} \vec{E}_{H,ni} = & \frac{-n j^n \cos(n\phi) N_{6,ni}^h \exp(-jk_0 r)}{r \sin \theta} J_n(k_0 b_1 \sin \theta) J_n(x'_{6,ni}) \hat{\theta} \\ & + \frac{j^n \cos \theta \sin(n\phi) k_0 b_1 N_{6,ni}^h \exp(-jk_0 r)}{r [1 - (k_0 b_1 \sin \theta / x'_{6,ni})^2]} J_n(x'_{6,ni}) J'_n(k_0 b_1 \sin \theta) \hat{\phi} \end{aligned} \quad (4.58a)$$

due to the ni -th TE modes in the sixth waveguide;

$$\vec{E}_{E,ni} = \frac{-j^n \sin \theta \cos(n\phi) N_{6,ni}^e \exp(-jk_0 r)}{r [(x_{6,ni}/k_0 b_1)^2 - \sin^2 \theta]} x_{6,ni} J'_n(x_{6,ni}) J_n(k_0 b_1 \sin \theta) \hat{\theta} \quad (4.58b)$$

due to the ni -th TM modes in the last circular waveguide. In (4.58a) and (4.58b), $(x'_{6,ni}/b_1)$ and $(x_{6,ni}/b_1)$ are the cutoff wavenumbers of the ni -th TE and TM modes in guide 6, respectively. $N_{6,ni}^h$ and $N_{6,ni}^e$ are their normalization coefficients of TE and TM modes in the circular waveguide and are given in Appendix A. The total radiated electric field can be calculated by summing the contributions due to all the modes in guide 6 according to (4.56).

4.4 Conclusions

Two numerically efficient techniques have been presented in the first two sections of this chapter. Mathematical expressions for the overall scattering matrices of two cascaded waveguide junctions have been derived and their great saving in computational effort has been demonstrated. A simple technique based on the idea of complexification and extrapolation has been introduced in the second section. Numerical tests have revealed that this technique is conceptually simple, computationally efficient, and numerically accurate. A detailed formulation for a stacked annular-ring-loaded circular microstrip antenna fed by an off-centered coaxial line has been presented in Section 3. Many practical antenna structures can result from

this general model. The proposed waveguide modal analysis rigorously takes the effect of the feed line and the finite thickness of patches into account. Moreover, the analysis is valid for uniaxial substrate and superstrate. The next chapter will show the calculated results for various microstrip antennas with circular geometries.

Chapter 5

Numerical Results for Circular Microstrip Antennas

To validate the proposed waveguide modal-expansion analysis presented in the previous chapter and to show the versatility of this technique, five typical complex microstrip antennas with circular geometries are analyzed in this chapter. These are: the single circular patch antenna with a centered or off-centered coaxial feed line, the annular-ring microstrip antenna, the annular-ring-loaded circular microstrip antenna, and the stacked circular disk antenna. For most cases the calculated results are presented with measured data taken from the literature. Convergence behavior with respect to the numbers of modes considered in the resulting waveguides and effect of the assumed outer cylindrical wall are examined for all these structures, but only some typical results for a single circular microstrip antenna fed by a coaxial line will be provided in the following. Computed results for the input impedance of all these microstrip antennas are given to show the effect of various structural and material parameters on the antennas' performances.

5.1 Circular Patch Fed by a Centered Coaxial Line

The first example we considered is a single circular microstrip patch antenna fed by a coaxial cable, as shown in Figure 5.1. This is the simplest example because its structure is azimuthally symmetrical [79]. As in the case of monopole antennas, the convergence behavior with respect to the numbers of modes considered in the resulting waveguides is examined initially. Superstrate is removed for simplicity at the stage of checking convergence behavior; its effect will be studied later. Table 5.1 and Table 5.2 provides the convergence characteristics of the truncation numbers N_1 and N_3 . N_2 is chosen as $N_2 = N_3(b_2 - a_0)/(b_2 - a)$ to ensure proper convergence, where b_2 is the radius of the outer cylinder. It is found that the choice of $N_1 = 1$ and $N_3 = 60$ is good enough to get convergent results.

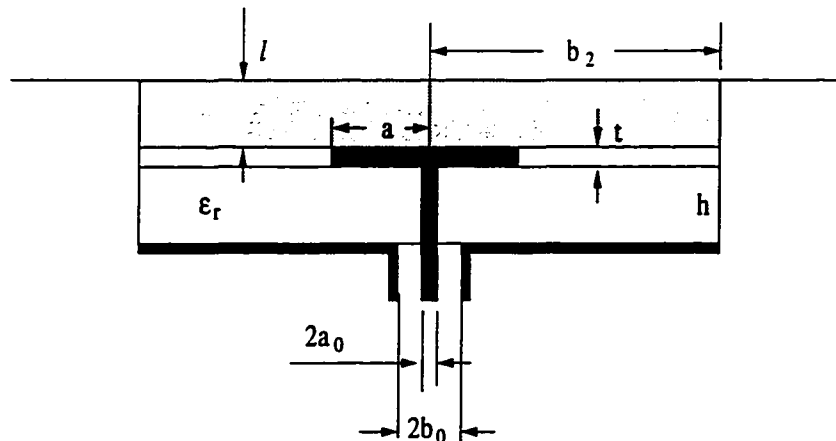


Figure 5.1: Geometry of a circular patch antenna fed by a centered coaxial line and covered by a superstrate.

The effect of the radius of the assumed outer circular waveguide on the antenna's input impedance is examined in Figure 5.2. It is seen that the size of the introduced

Table 5.1: Convergence of the impedance (Ohms) of a circular disk antenna with respect to N_1 ($a_0 = 0.6mm$, $a = 30mm$, $k_0a = 3.5$, $\epsilon_r = 1$, $h = 1.5mm$, $t = 0.1mm$).

N_1	Resistance	Reactance
1	70.1	132.7
4	69.9	132.5

Table 5.2: Convergence of the impedance (Ohms) of a disk antenna with respect to N_3 ($a_0 = 0.6mm$, $a = 30mm$, $k_0a = 3.5$, $\epsilon_r = 1$, $h = 1.5mm$, $t = 0.1mm$).

N_3	Resistance	Reactance
5	167.8	-85.9
10	145.3	141.7
30	78.1	136.0
60	69.9	132.5
120	68.7	131.6

cylindrical wall has a negligible influence on the input impedance when b_2 is larger than two wavelengths. This is expected since the main radiation occurs in the vertical direction and the introduced thin wall would not have significant effect on the antenna's radiation.

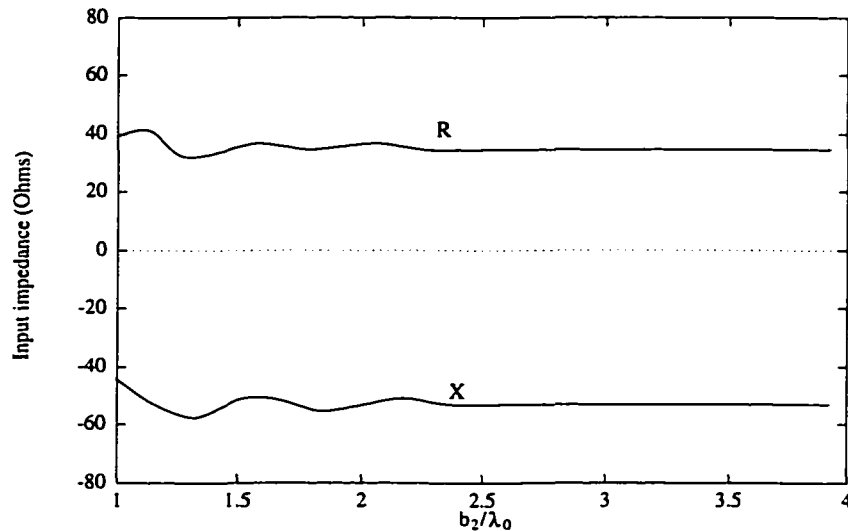


Figure 5.2: Variation of the input impedance of a circular patch with respect to the radius of the assumed boundary ($a_0 = 0.6mm$, $a = 30mm$, $f = 6GHz$, $\epsilon_r = 1$, $h = 1.5mm$, $t = 0.1mm$).

Figure 5.3 shows the comparison of our waveguide modal-expansion results with those obtained by the moment method [82] for the input impedance of a circular disk antenna. Both substrate and superstrate are assumed to be air in this case. It is seen that the agreement is excellent. In Table 5.3, a comparison between our computed results and the measured data in [82] is presented for the frequency where the reflection coefficient $10\log_{10}|S_{110}|^2$ attains its minimum value in the first resonance. We see that they agree very well.

Figure 5.4 illustrates the effect of a superstrate residing above a circular patch

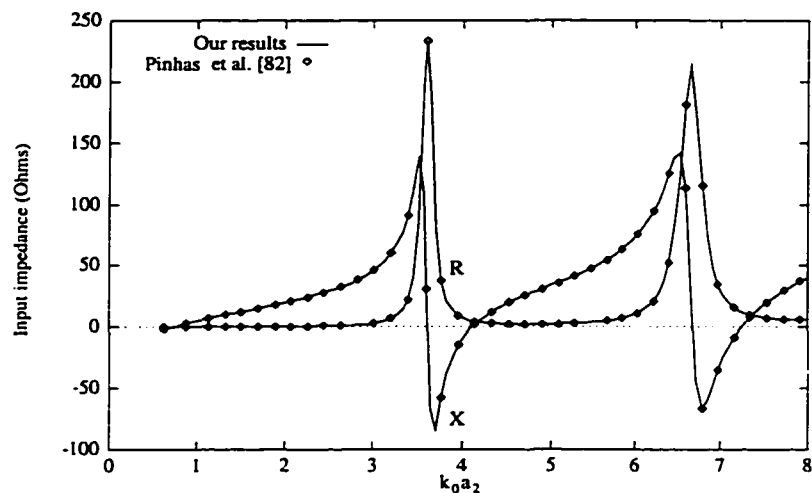


Figure 5.3: Input impedance of a circular patch antenna fed by a centered coaxial line ($a_0 = 0.6mm$, $a = 30mm$, $\epsilon_r = 1$, $h = 1.5mm$, $t = 0.1mm$).

Table 5.3: Comparison between our results and theoretical and experimental ones in [82] for the frequency (GHz) at minimum $10\log_{10}|S_{110}|^2$ ($a_0 = 0.6mm$, $a = 30mm$, $\epsilon_r = 1$, $t = 0.1mm$).

h(mm)	Our results	Theoretical results in [82]	Experimental data in [82]
1.6	6.02	6.01	6.17
2.0	6.04	6.04	6.14
4.0	6.04	6.05	6.02
5.0	5.98	5.97	5.93
7.5	5.77	5.77	5.63

on the antenna's input impedance, where l and ϵ_r^b are, respectively, the thickness and dielectric constant of the superstrate. It is expected that both the thickness and the dielectric constant have a significant effect on the antenna's performance. The fact that the superstrate reduces the resonant frequency is not surprising. It might be possible to widen the antenna's impedance bandwidth by properly choosing the parameters of the superstrate.

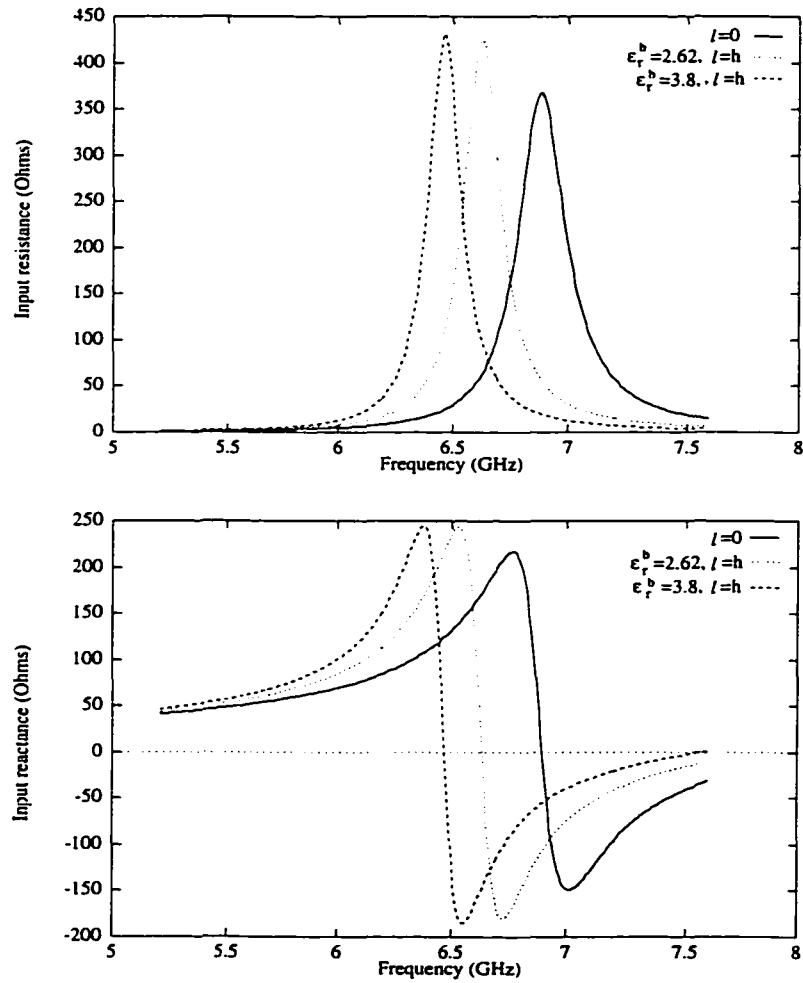


Figure 5.4: Effect of the superstrate on the circular patch antenna's impedance ($a_0 = 0.5mm$, $a = 30mm$, $a = 15mm$, $h = 1.6mm$, $t = 0.1mm$, $\epsilon_r^p = \epsilon_r^b$).

The effect of the finite thickness of the circular patch on the antenna's input impedance is illustrated in Figure 5.5. It is seen that a thicker patch exhibits a lower effective Q and that increasing the thickness of the microstrip patch smooths the impedance versus frequency variation by lowering the magnitude of the resistance and reactance peaks near resonance. It is also observed that increasing the patch's thickness decreases the resonant frequency of the antenna since a thicker microstrip disk is equivalent to a patch of larger radius, which results in a smaller resonant frequency.

The effect of the anisotropy of the substrate and superstrate on the impedance of a center-fed microstrip disk antenna is examined in Figure 5.6, where results are given for a disk of radius $a = 15mm$ on a substrate of thickness $h = 1.6mm$ and covered by a superstrate of the same parameters as the substrate. It is noted that the material's anisotropy decreases the antenna's resonant frequency because a negative uniaxial substrate/superstrate equivalently produces a large effective dielectric constant.

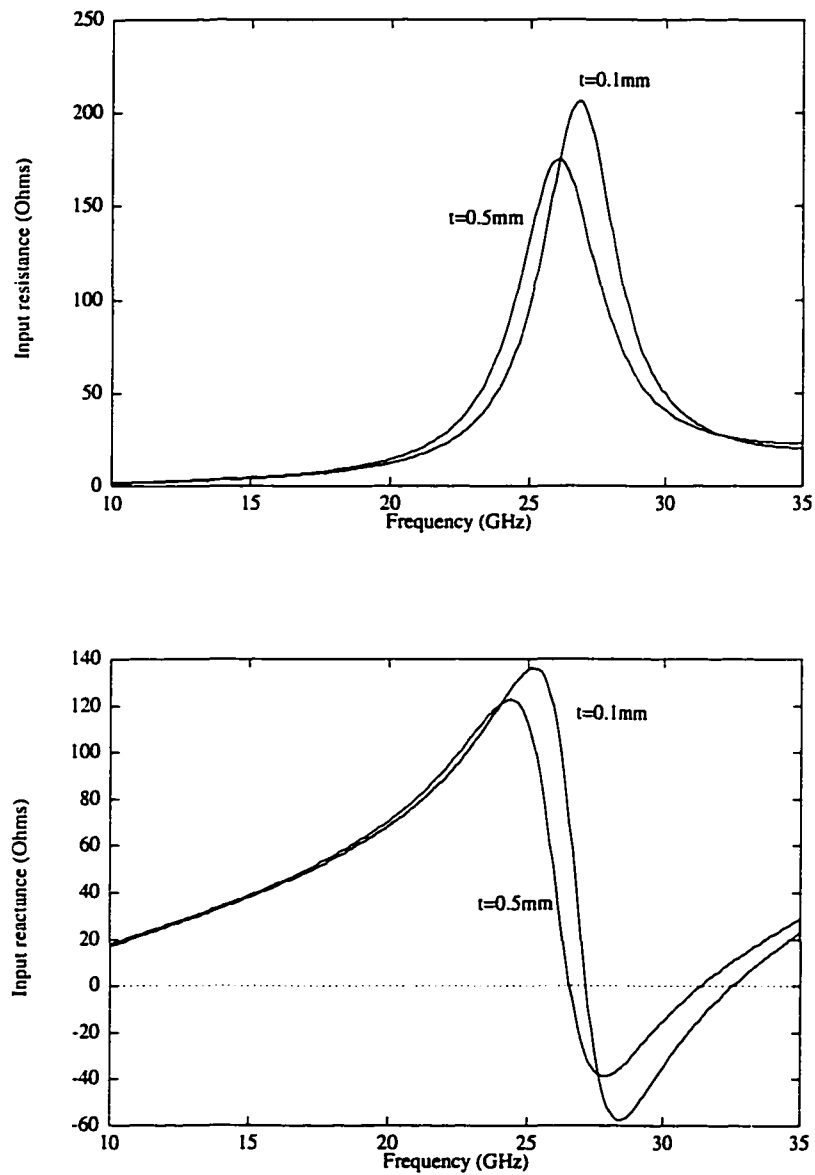


Figure 5.5: Effect of the finite thickness of the circular patch on the antenna's impedance ($a_0 = 0.5\text{mm}$, $a = 15\text{mm}$, $h = 1.6\text{mm}$, $t = 0.1\text{mm}$, $\epsilon_r = 1$).

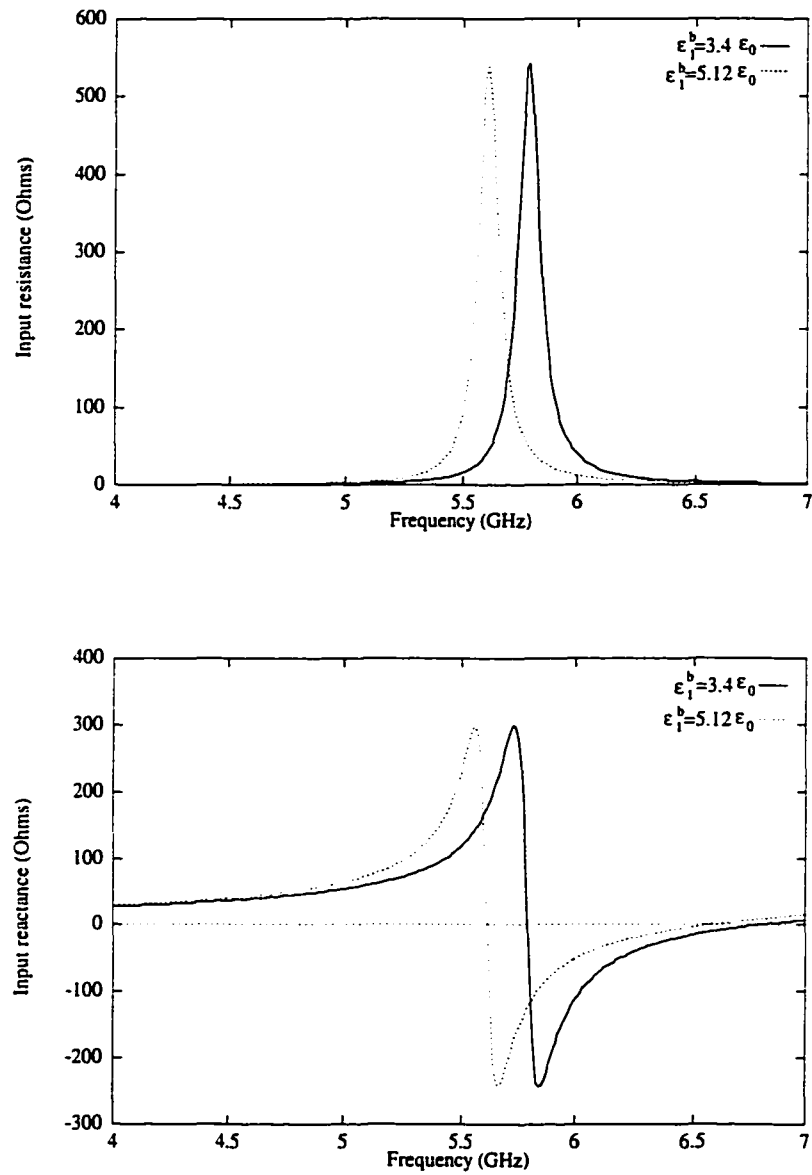


Figure 5.6: Effect of the anisotropy of the substrate and superstrate on a circular patch antenna's impedance ($a_0 = 0.5mm$, $l = h$, $t = 0.1mm$, $\epsilon_{r2}^p = \epsilon_{r2}^p = 3.4$).

5.2 Circular Patch Fed by an Off-Centered Cable

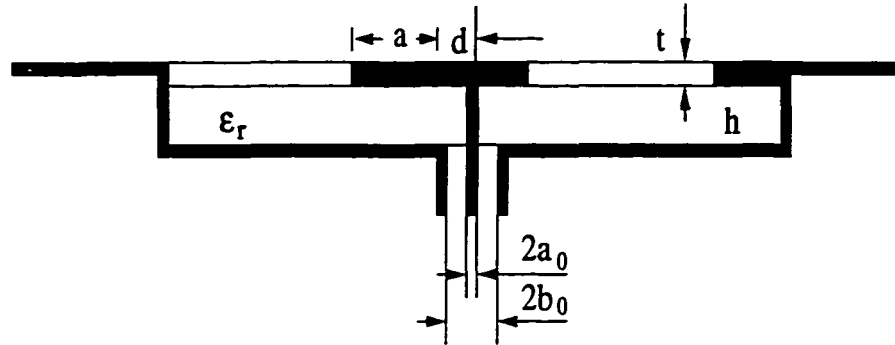


Figure 5.7: Geometry of a circular patch antenna fed by an off-centered coaxial line.

The second example is a more practical antenna—a single circular patch antenna fed by an off-centered coaxial line, which is illustrated in Figure 5.7. For this example, we set $s_1 = t_2 = a_2 = s_2 = 0$ and $c_1 = d_1$ in Figure 4.6 and are left with only three coaxial waveguides. Let the numbers of modes considered in these three waveguides be N_1 , N_2 , N_3 , respectively. The convergence behavior of the input impedance of a circular microstrip antenna with respect to the truncation numbers N_1 , N_2 , and N_3 is also checked initially. The circular patch considered in this section is of radius 30mm and of thickness 0.1mm. The substrate is of thickness 2.1844mm and its relative permittivity is 2.33. The patch is fed at $d = 7mm$ by a coaxial line with inner and outer conductors' radii being 0.45mm and 1.5mm. Table 5.4 shows the convergence of the input impedance with respect to the number N_1 of modes considered in the coaxial-feed waveguide. It is seen that the results obtained by taking only the dominant TEM mode into account is quite good. Table 5.5 gives the convergence characteristic of a circular patch antenna's impedance with respect to N_3 . It is seen that $N_3 = 211$ (1 TEM mode, 70 TM_{0n} modes, 70 TE_{1n}

and 70 TM_{1n}) is sufficient to get convergent results. Table 5.6 presents the relevant information on convergence behavior of impedance versus N_2 ; 2501 modes (1 TEM mode, 1200 TE modes and 1300 TM modes are needed to give an accurate result for the input impedance. The requirement that large number of modes should be retained in the second coaxial waveguide does not pose any serious computational problem since the size of the matrices to be inverted has nothing to do with the number N_2 [66].

Table 5.4: Convergence of a circular microstrip antenna's impedance (Ohms) with respect to N_1 ($f = 2.65GHz$).

N_1	Resistance	Reactance
1	51.4	68.6
2	51.3	68.5
5	51.2	68.4

Table 5.5: Convergence of a circular microstrip antenna's impedance (Ohms) with respect to N_3 ($f = 2.65GHz$).

N_3	Resistance	Reactance
61	75.5	-14.8
121	72.8	61.0
211	51.3	68.4
301	49.2	68.5

An important parameter in this waveguide modal analysis is the size b_1 of the

Table 5.6: Convergence of a circular microstrip antenna's impedance (Ohms) with respect to N_2 ($f = 2.65GHz$).

N_2	Resistance	Reactance
211	5.2	43.1
351	15.4	55.7
631	26.6	63.4
1361	35.8	66.8
2501	49.2	68.5
3721	51.3	68.4

assumed cylindrical wall. It is apparent that the larger b_1 is, the weaker is the effect of the wall on the performance of a microstrip antenna. For the dominant TM_{11} mode operation of circular microstrip antennas, the major radiation occurs in the normal z direction. Then the assumed outer cylindrical wall has no significant effect on the estimation of the antenna's impedance, as shown in Figure 5.8. When b_1 changes from $1.3\lambda_0$ to $2.5\lambda_0$, the impedance loci of a circular microstrip antenna has no noticeable change. For the results that follow, we choose $b_1 = 1.5\lambda_0$.

Figure 5.9 compares our waveguide modal results with the experimental ones of [44] for the impedance loci of a circular microstrip antenna fed by an off-centered coaxial probe. It can be seen that the agreement is excellent. Radiation patterns for a circular disk antenna at resonance (2.7GHz) and off-resonance (2.6GHz) are shown in Figure 5.10.

Figure 5.11 examines the variation of a circular microstrip antenna's impedance loci with respect to the radius of the feeding probe. It is seen that varying the radius of the probe mainly changes the input reactance, but antenna's input resistance is

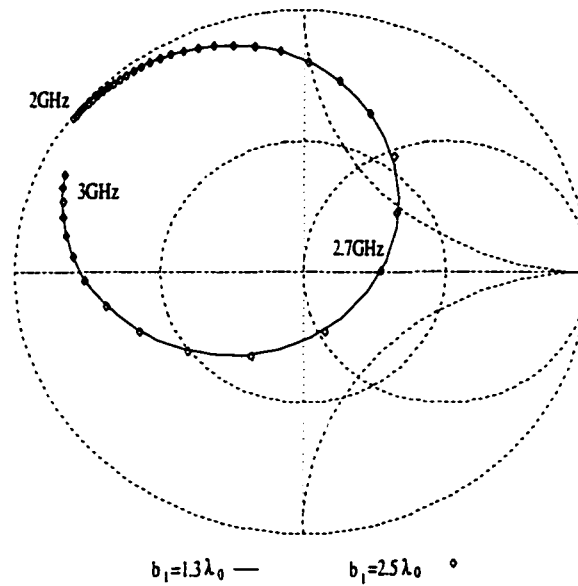


Figure 5.8: Impedance loci of a circular microstrip antenna for different values of b_1 , the size of the outer cylindrical wall ($a_0 = 0.45mm$).

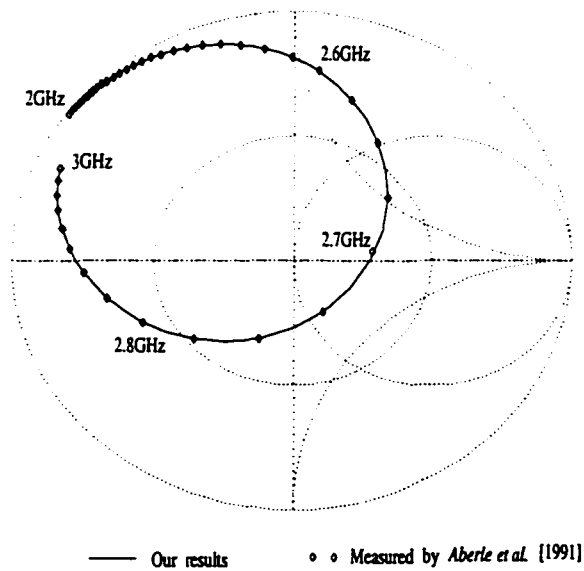


Figure 5.9: Impedance loci of a circular microstrip antenna fed by an off-centered coaxial line.

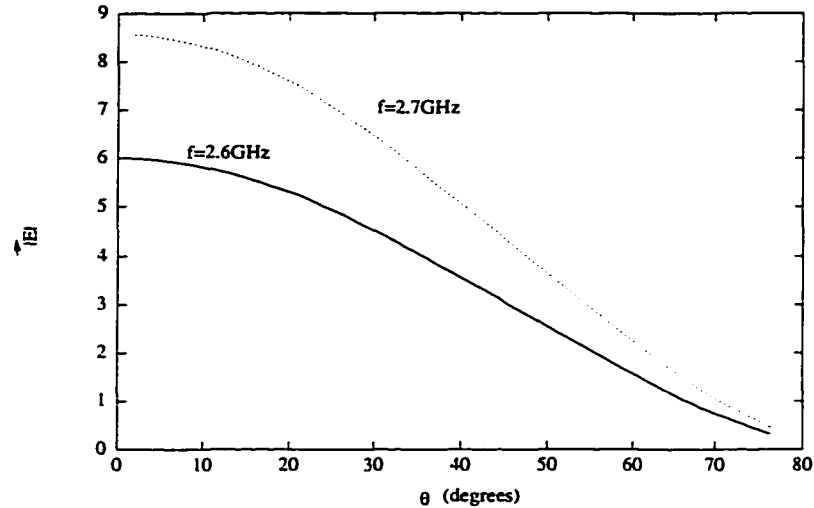


Figure 5.10: Radiated E-field patterns of a circular microstrip antenna at resonance and at off-resonance.

insensitive to the probe size since it is mainly determined by the magnetic surface current along the patch edge [36].

The position of the feeding probe has a significant effect on the impedance of a circular microstrip antenna, as shown in Figure 5.12. The eccentricity d determines the radius of the impedance loci in the Smith chart. It is seen that by properly selecting the eccentricity d one can adjust the impedance loci and a good matching point may then be achieved in the coaxial feed line for a circular microstrip antenna.

Figure 5.13 illustrates the effect of the substrate's thickness on the microstrip antenna's input impedance. We see that using a thicker substrate results in a significant increase in the antenna's bandwidth, as expected. Therefore, one way to widen the bandwidth of a microstrip antenna is to use a thick substrate. It is also observed that increasing the thickness of the substrate decreases the antenna's resonant frequency.

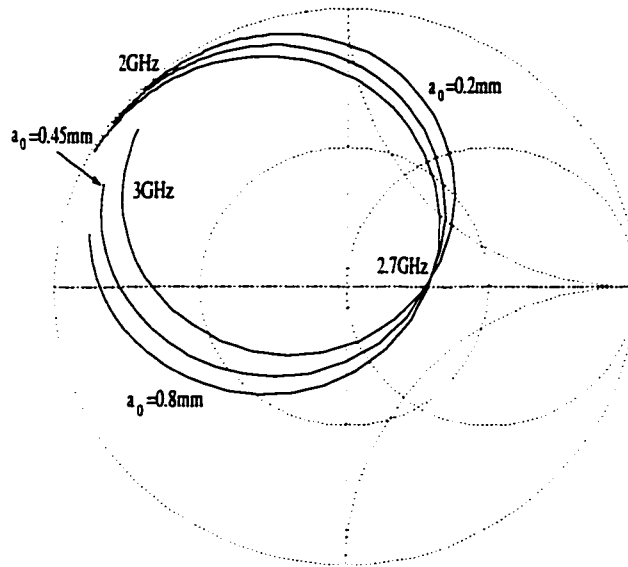


Figure 5.11: Impedance loci of a circular microstrip antenna for different values of a_0 .

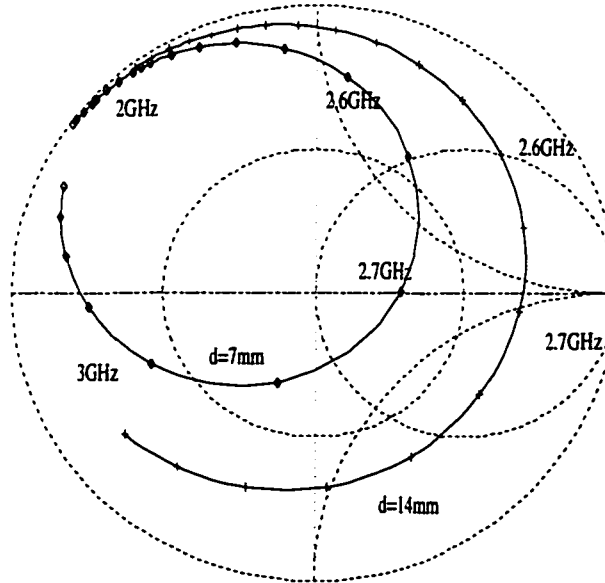


Figure 5.12: Impedance loci of a circular microstrip antenna for different values of d .

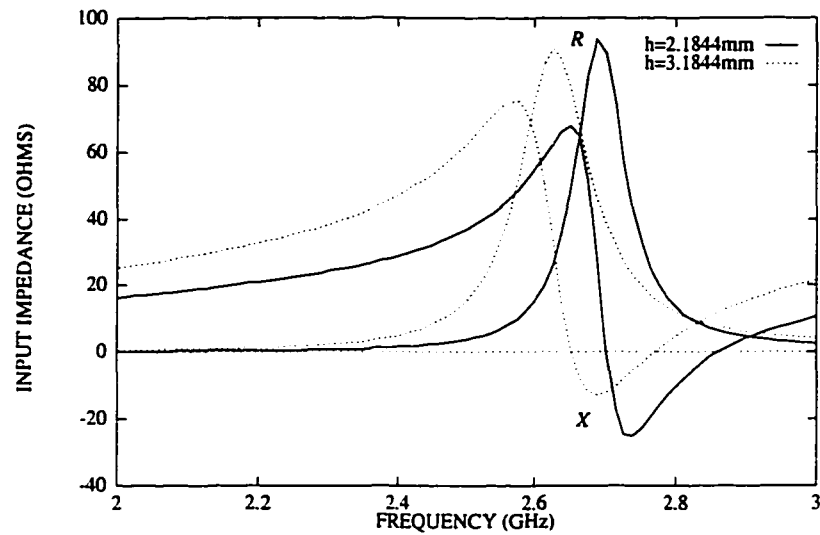


Figure 5.13: Input impedance of a circular microstrip antenna for different substrate thicknesses.

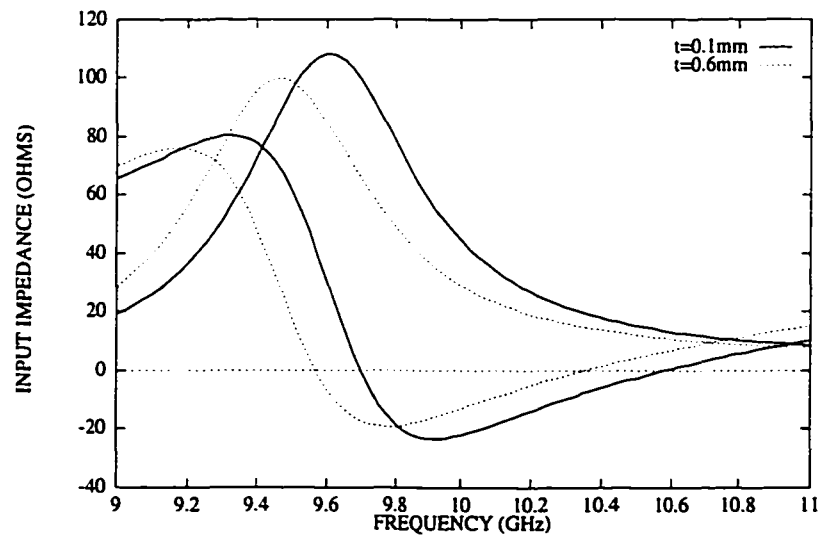


Figure 5.14: Effect of the finite thickness of the patch on the input impedance of a circular microstrip antenna ($a_0 = 0.32mm$, $b_0 = 2.301a_0$, $a_1 = 5mm$, $h = 1.2mm$, $d = 2mm$, $\epsilon_r = 2.6$).

The effect of the finite thickness of the circular patch on the antenna's input impedance is illustrated in Figure 5.14. As we know from the previous section, increasing the thickness of the microstrip patch smooths the impedance vs. frequency variation and using a thick patch can broaden the antenna's bandwidth. As before, increasing the patch's thickness slightly decreases the microstrip antenna's resonant frequency.

The effect of the substrate's anisotropy on a circular microstrip antenna's input impedance is examined in Figure 5.15. It is noted that dielectric anisotropy of the substrate has a noticeable influence on the antenna's resonant frequency. A bigger ϵ_{b1} results in a larger effective permittivity, which decreases the resonant frequency. A small decrease in μ_{b1} exhibits a significant increase in the antenna's resonant frequency. It is important to account for the effect of the substrate's anisotropy for the evaluation of a microstrip antenna's resonant frequency due to its narrow-bandwidth nature.

5.3 Annular-Ring Microstrip Antenna

The third example is an annular-ring microstrip antenna fed by a coaxial line, as shown in Figure 5.16. Computed results for the input impedance of an annular-ring microstrip antenna fed by an off-centered coaxial line and excited in the TM_{11} are shown in Figure 5.17, where the inner and outer radii of the ring patch are $d_1 = 7.5mm$ and $a_1 = 15mm$, respectively. The isotropic substrate is of relative permittivity 2.58 and of thickness $h = 1.6mm$. The coaxial feed line is connected to the annular-ring at $d = 9mm$. There is no superstrate assumed in this example.

It is noted that the resonant frequency of a ring patch is much lower than a

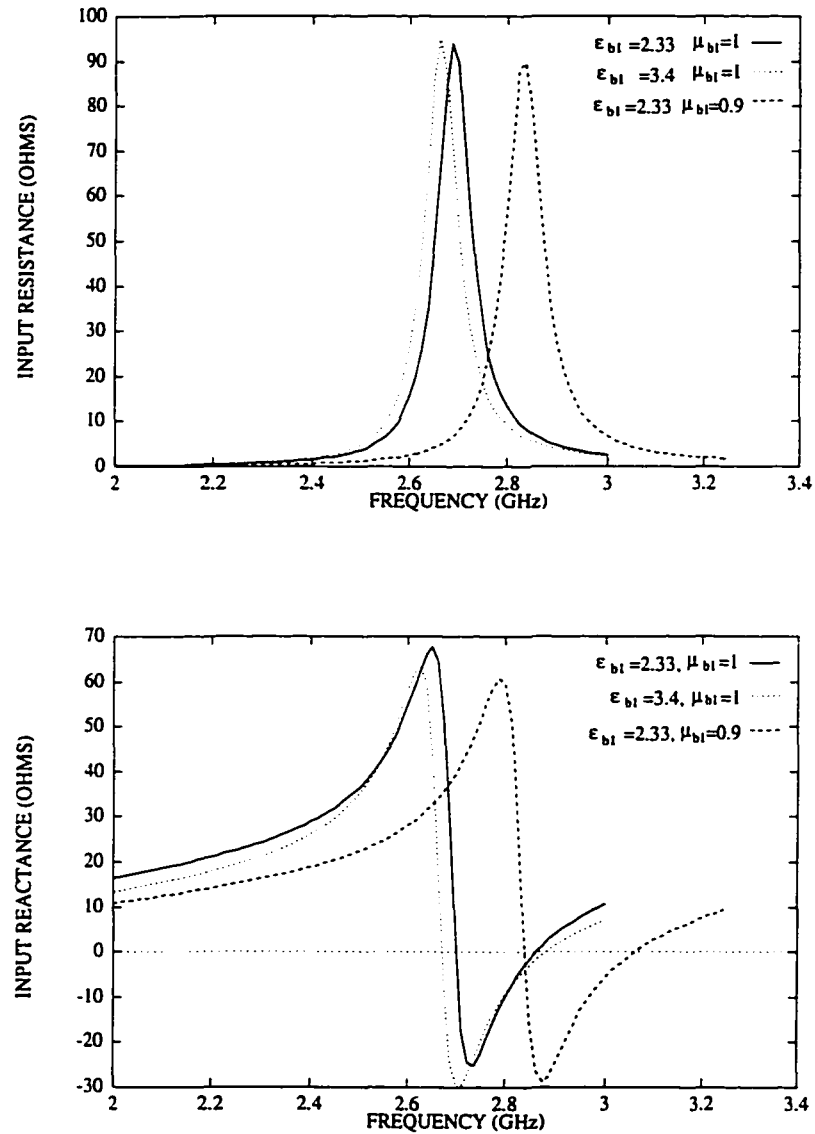


Figure 5.15: Effect of the substrate's anisotropy on the input impedance of a circular microstrip antenna ($a_0 = 0.8mm$, $b_0 = 2.301a_0$, $a_1 = 20mm$).

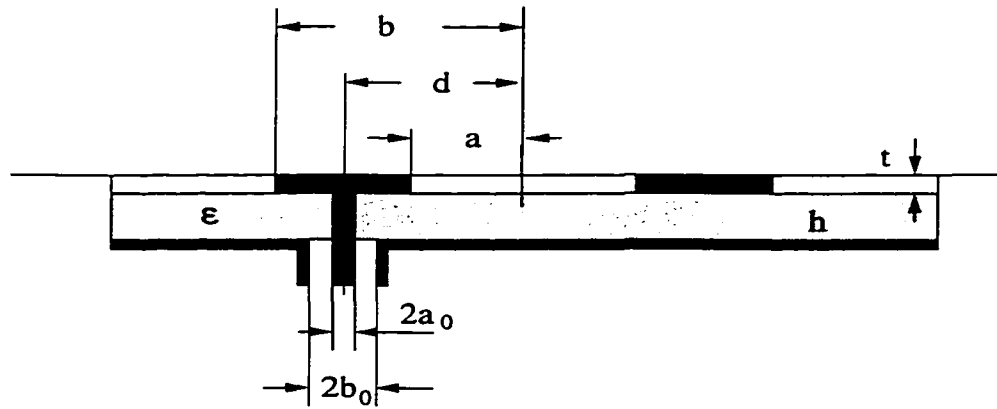


Figure 5.16: Geometry of an annular-ring patch antenna fed by a coaxial line.

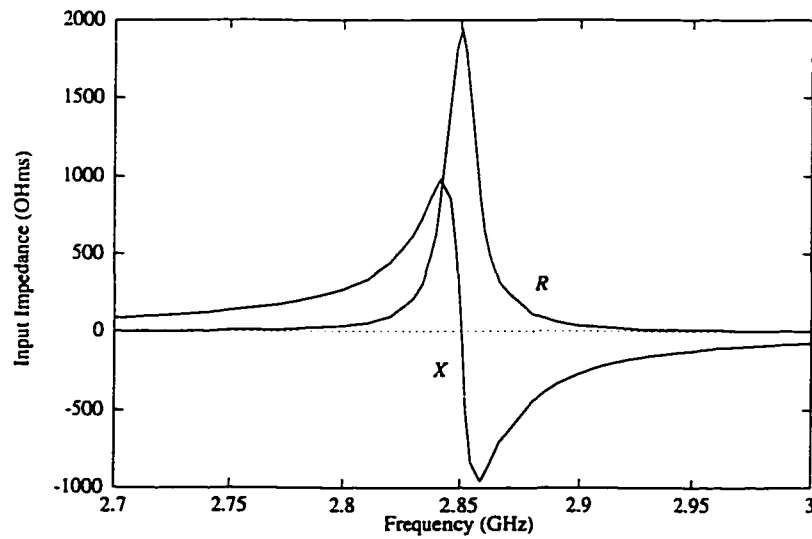


Figure 5.17: Input impedance of an annular-ring microstrip antenna fed by an off-centered coaxial line.

circular patch of approximately the same size. This property of the annular-ring patch antenna is attractive for applications in mobile communications, where small antennas operating at 0.9GHz and 1.8GHz are desired. It is also seen that the bandwidth of an annular-ring microstrip antenna for TM_{11} mode excitation is very narrow and the resonant resistance is very high compared to those of a circular patch antenna; this very high Q nature suggests that a ring patch is best used as a resonator, not as an antenna. However, studies ([45] and [46]) have revealed that an annular-ring microstrip patch excited in the TM_{12} can give superior performance as an antenna compared to the circular patch antenna.

5.4 Annular-Ring-Loaded Circular Disk Antenna

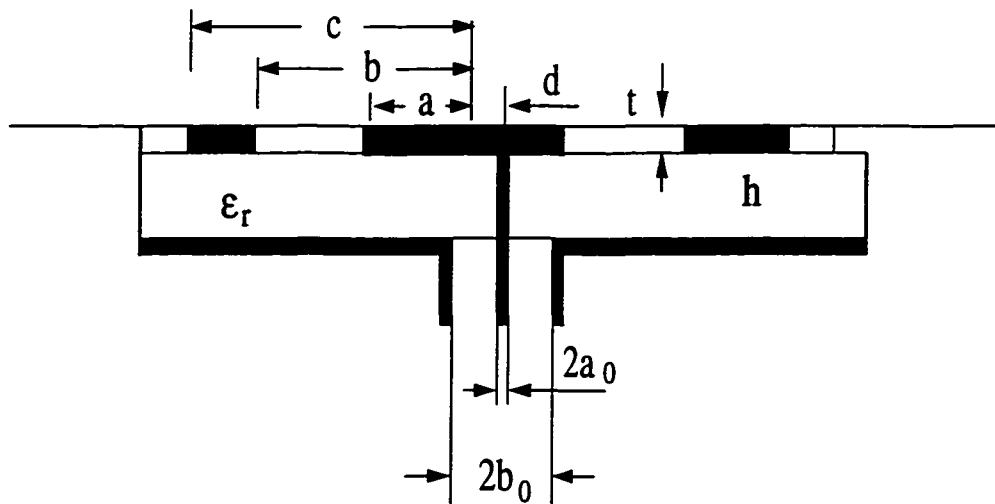


Figure 5.18: Geometry of an annular-ring-loaded circular microstrip antenna fed by a coaxial line.

To show the applicability of the waveguide modal-expansion method to more complicated microstrip antennas of circular shape, the annular-ring-loaded circular mi-

crostrip antenna shown in Figure 5.18 is investigated. The structural and electrical parameters of the considered example are as follows: $a_0 = 0.32\text{mm}$, $b_0 = 2.301a_0$, $a = 12\text{mm}$, $b = 15\text{mm}$, $c = 30\text{mm}$, $t_1 = 0.1\text{mm}$, $h = 2.8\text{mm}$, and $d = 8.2\text{mm}$. It is assumed that the substrate is an isotropic material of relative permittivity 2.65 and no superstrate is involved. Figure 5.19 gives the comparison of our computed results and the experimental results measured in [47] for the input impedance of the annular-ring-loaded circular microstrip antenna. Very good agreement is observed. By properly choosing the size of the loading annular-ring, it is possible to have two resonances within the operating frequency range [47]. The additional resonance provided by the annular-ring widens the bandwidth of the microstrip antenna.

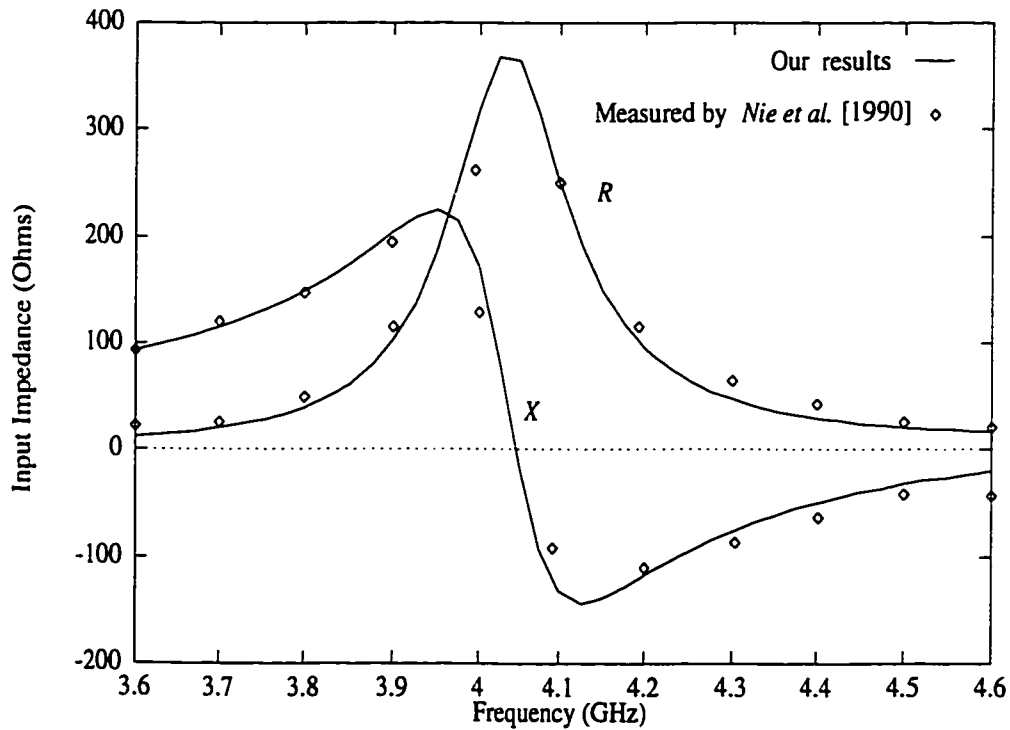


Figure 5.19: Input impedance of an annular-ring-loaded circular microstrip antenna fed by an off-centered coaxial line.

5.5 Stacked Circular Patch Antennas

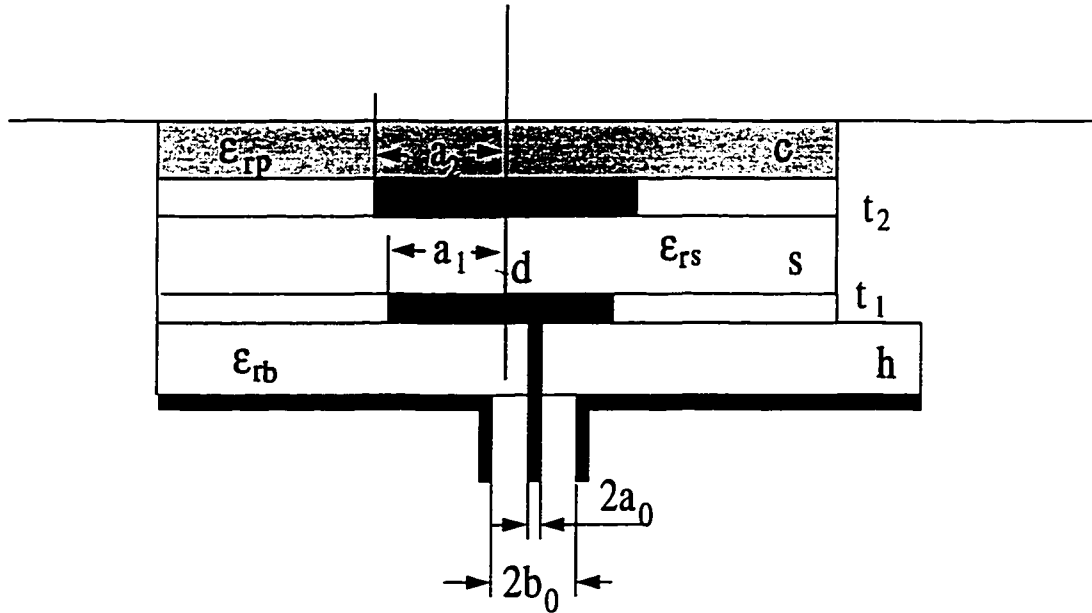


Figure 5.20: Geometry of a stacked circular microstrip antenna fed by an off-centered coaxial line.

The last example we considered in the category of microstrip antennas is a stacked circular microstrip antenna, as illustrated in Figure 5.20. The structure results from by setting $c_1 = d_1$ in Figure 4.6. It is well known that the parasitic circular patch provides additional resonance and increases the bandwidth. Figure 5.21 shows a comparison of our calculated results and measured data in [49] for the impedance loci of a stacked circular microstrip antenna fed by an off-centered coaxial line. The feed coaxial line of inner radius $a_0 = 0.635\text{mm}$ has a standard characteristic impedance of 50 Ohms. The driven circular patch is of radius $a_1 = 13.233\text{mm}$ and of thickness $t_1 = 0.1\text{mm}$. The parasitic patch is of radius $a_2 = 1.01a_1$ and of thickness $t_2 = 0.1\text{mm}$, and the distance between two patches is $s_1 = 0.36a_1$. The sandwiched dielectric is made of foam of relative permittivity $\epsilon_{rs} = 1.22$. The

substrate of thickness $h = 1.52mm$ and the superstrate $s_2 = 0.76mm$ are both made of an isotropic material of dielectric constant 2.45. The feed point is shifted from the center of the driven patch by $d = 0.6a_1$. It is seen that the agreement is fairly good. There are two resonances within the frequency range 3.2 – 5GHz and the bandwidth of a stacked antenna is much larger than that of a single circular antenna. Therefore, using the stacked configuration provides another way to widen microstrip antenna's bandwidth.

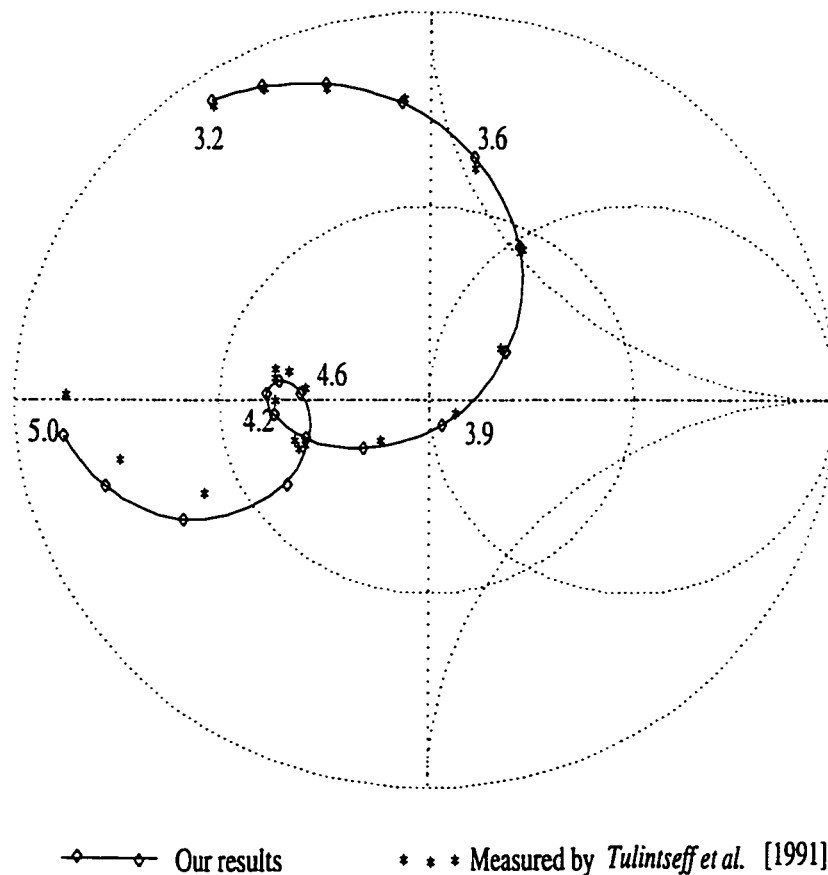


Figure 5.21: Impedance loci of a stacked circular microstrip antenna fed by an off-centered coaxial line.

5.6 Concluding Remarks

The waveguide modal-expansion method described in Chapter 4 has been applied to the analysis of five circular microstrip antenna structures in this chapter. Numerical results have been presented for probe-fed single and stacked, circular and annular-ring microstrip antennas. For these examples considered, it has been observed that the agreement between computed results by the waveguide modal-expansion method and measured data available in the literature is fairly good. Therefore, it can be concluded that the accuracy of the presented waveguide modal-expansion method is quite good.

Since all the E-field mode-matching matrices for all the waveguide junctions involved in the waveguide modal-expansion method are in closed form, no series summation or numerical integrations are needed in obtaining all the matrix elements. Thus, this waveguide modal-expansion method is also computationally efficient, though the size of the matrices involved is quite large. Comparatively, the method of moments [44], [37] deals with a relatively small matrix equation, while the computation of each element is time-consuming since numerical evaluation of Sommerfeld integral is often invoked.

Chapter 6

Conclusions

6.1 Summary of Contributions

Although antenna engineering has a history of over 80 years, it remains a vibrant field which is bursting with activities. Nowadays, many communication systems are becoming more and more complicated and the frequency range of interest is progressing upward. Designing novel antennas to catch up with this trend and to meet the tight system specifications is a challenge. Development of accurate and efficient modeling and simulation tools, prediction of radiation and impedance performance, and suggestion of novel structures become increasing important and highly desirable.

In this thesis, a rigorous full-wave modal-expansion method has been developed to model cylindrical monopole and microstrip patch antennas. This method initially introduces an appropriate boundary to transform the open-region antenna problems into “closed-region” guided-wave problems. The resulting waveguide structures are then solved by the formally exact modal-expansion method. Application of this

introduced technique to many practical antenna configurations has been demonstrated.

In the following, a summary of the major contributions made in this thesis is given.

1. A unified formulation for cylindrical monopole antennas has been developed. The presented formulation is very general and applies to many practical monopole structures such as: the conventional monopole, the sleeve monopole, dielectric-coated and -buried monopoles, and a multilayer insulated monopole antenna. Based on the idea of a “perfectly matched boundary”, the radiation antenna problem is initially transformed into a guided-wave transmission problem. Modal-expansion method is then employed to formulate the general problem. The developed formulation is valid for both thin and thick monopoles. The coaxial feed line and conductors’ finite thicknesses are rigorously taken into account. Analysis of a multilayered structure is implemented by an efficient recursive algorithm.
2. Extensive computed results for various monopole antennas have been presented. The effect of the junction between the monopole and the coaxial feed line, which was usually ignored in most previously published methods, has been examined in detail. Three types of junction are clarified and studied individually. It is found that the junction effect is sometimes significant and has to be taken into consideration in antenna matching. The effect of the sleeve’s finite thickness on the sleeve monopole’s input impedance has been examined. It is observed that using a thick sleeve can widen the monopole’s bandwidth. Impedance characteristics of a monopole coated by dielectric or buried in a dielectric substrate have been investigated. Variation of the in-

put impedance of an insulated monopole with various parameters has been numerically studied.

3. A monopole over a finite ground plane of finite thickness was analyzed by the waveguide modal-expansion method. Numerical results were presented and compared with experimental data available in the literature.
4. An improved formulation has been introduced for two cascaded waveguide junctions. Overall scattering matrices for three different types of cascading connection have been derived. The remarkable saving in computation effort gained from this improved formulation has been demonstrated and its application to the analysis of circular microstrip antennas is emphasized.
5. A simple technique for calculating the reflection coefficients of open-ended waveguides is proposed in this thesis. Based on the idea of complexification and extrapolation, the problem of an open-ended waveguide was transformed into a waveguide junction problem, which can be easily solved by the modal-expansion method. Numerical tests show that this technique is conceptually simple, computationally efficient, and numerically accurate.
6. A full-wave waveguide modal-expansion analysis has been presented for analyzing single and stacked probe-fed microstrip antennas with circular geometries. The coaxial feed line, which was often treated as a line current excitation in most previous works, is rigorously considered in this analysis. The effect of patch's finite thickness on the microstrip antenna's input impedance is examined. It is found that this effect is negligible in microwave bands, while it becomes noticeable in millimeter-wave bands. A superstrate residing on the patch has been shown to have a pronounced influence on the antenna's performance. The effect of the substrate's anisotropy on the microstrip antenna's

resonant frequency is also studied.

6.2 Recommendations for Future Research

In this thesis, there are a number of research topics which are worthy of further investigation.

1. Structurally similar to the dielectric-coated monopole antenna considered in Section 3.3.1, dielectric resonator antenna [83] fed by a centered or off-centered coaxial line is now receiving increasing attention due to its advantages such as small size and broad bandwidth. The modal-expansion method presented in this thesis can be employed to accurately study the input impedance and far-zone radiation pattern of the cylindrical dielectric resonator antenna. The coaxial feed line can also be rigorously taken into consideration in the modal-expansion analysis.
2. It is well-known that using a thick substrate can widen the bandwidth of a microstrip antenna. However, a thick substrate can excite strong surface waves which could degrade the antenna's radiation performance. In order to use a thick substrate and also to suppress the surface-wave excitation, cavity-backed microstrip antennas are then preferred [84]. The waveguide modal-expansion method presented in Chapter 4 can be extended with minor changes to analyze cavity-backed single and stacked probe-fed circular and annular-ring microstrip antennas.
3. Another type of antenna—the slot antenna has found wide application in communication systems. With a slight modification, the presented modal-expansion method can be generalized to analyze the impedance characteristics

of various slot antennas backed by a cavity of circular or rectangular shape [85].

4. Based on the same basic idea of the waveguide modal-expansion method introduced in Chapter 4, one can explore other feeding structures for circular microstrip antennas. Circular or rectangular waveguide end-feed through a circular or rectangular aperture can be easily characterized using this modal-expansion method. Feeding structures using apertures on the broad-wall of a rectangular waveguide can also be modeled; this type of feeding structure could be used for array applications.

Appendix A

Waveguide Modal Functions

A.1 Parallel-Plate Waveguide

A parallel-plate waveguide consists of two infinitely large parallel-plates separated by a distance d , as illustrated in Figure A.1.

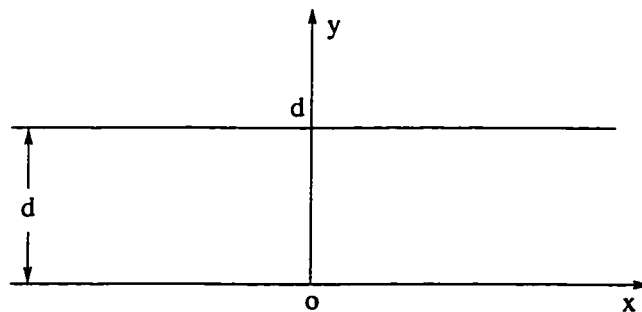


Figure A.1: Parallel-plate waveguide.

TM Modes

$$E_z = -\frac{n\pi}{d\gamma_n} \sqrt{\frac{\epsilon_n}{d}} \sin \frac{n\pi y}{d} e^{-j\beta_n z}, \quad E_y = \sqrt{\frac{\epsilon_n}{d}} \cos \frac{n\pi y}{d} e^{-j\beta_n z} \quad (\text{A.1})$$

$$H_x \hat{x} = Y_n^e \hat{z} \times (E_y \hat{y}) \quad (\text{A.2})$$

and

$$E_x = H_y = H_z = 0 \quad (\text{A.3})$$

where

$$Y_n^e = \frac{j\omega\epsilon}{\gamma_n}, \quad \gamma_n^2 = -\beta_n^2 = \left(\frac{n\pi}{d}\right)^2 - k^2, \quad n = 0, 1, \dots \quad (\text{A.4})$$

It should be pointed out here that *TM₀ mode is actually the TEM mode.*

TE Modes

$$\phi_n^h = \frac{d}{n\pi} \sqrt{\frac{\epsilon_n}{d}} \cos \frac{n\pi y}{d} e^{-j\beta_n z} \quad (\text{A.5})$$

$$E_x \hat{x} = \hat{z} \times \nabla_t \phi_n^h, \quad H_y \hat{y} = Y_n^h \hat{z} \times (E_x \hat{x}) \quad (\text{A.6})$$

and

$$E_y = E_z = H_x = 0 \quad (\text{A.7})$$

where

$$Y_n^h = \frac{\gamma_n}{j\omega\mu}, \quad \gamma_n^2 = -\beta_n^2 = \left(\frac{n\pi}{d}\right)^2 - k^2, \quad n = 1, 2, \dots \quad (\text{A.8})$$

A.2 Rectangular Waveguide

The length and width of a rectangular waveguide are assumed to be a and b , respectively, as shown in Figure A.2 along with the coordinate system.

TM Modes

$$\phi_{mn}^e = N_{mn} \sin \frac{m\pi x}{a} \sin \frac{n\pi y}{b}, \quad m, n = 1, 2, \dots \quad (\text{A.9})$$

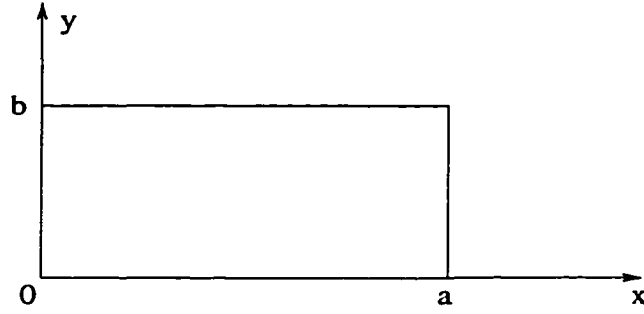


Figure A.2: Rectangular waveguide.

$$\vec{E}_t = \nabla_t \phi_{mn}^e, \quad \vec{H}_t = Y_{mn}^e \hat{z} \times \vec{E}_t \quad (\text{A.10})$$

$$k_{cmn}^2 = \left(\frac{m\pi}{a}\right)^2 + \left(\frac{n\pi}{b}\right)^2, \quad N_{mn} = \frac{\sqrt{\epsilon_m \epsilon_n}}{\pi k_{cmn}} \quad (\text{A.11})$$

$$\gamma_{mn}^2 = -\beta_{mn}^2 = k_{cmn}^2 - k^2, \quad Y_{mn}^e = \frac{j\omega\epsilon}{\gamma_{mn}}. \quad (\text{A.12})$$

TE Modes

$$\phi_{mn}^h = N_{mn} \cos \frac{m\pi x}{a} \cos \frac{n\pi y}{b}, \quad m, n = 0, 1, \dots \quad (\text{A.13})$$

$$\vec{E}_t = \hat{z} \times \nabla_t \phi_{mn}^h, \quad \vec{H}_t = Y_{mn}^h \hat{z} \times \vec{E}_t \quad (\text{A.14})$$

where

$$Y_{mn}^h = \frac{\gamma_{mn}}{j\omega\mu}. \quad (\text{A.15})$$

A.3 Circular Waveguide

The radius of a circular waveguide is assumed to be a . The cylindrical coordinates (ρ, ϕ) with its origin at the center of the waveguide are adopted here.

TM modes

$$\phi_{mn}^e = N_{mn}^e J_m\left(\frac{x_{mn}\rho}{a}\right) \cos(m\phi) \quad (\text{A.16})$$

$$\vec{E}_t = \nabla_t \phi_{mn}^e, \quad \vec{H}_t = Y_{mn}^e \hat{z} \times \vec{E}_t \quad (\text{A.17})$$

where

$$\gamma_{mn}^2 = -\beta_{mn}^2 = (x_{mn}/a)^2 - k^2 \quad (\text{A.18})$$

$$N_{mn}^e = \sqrt{\frac{\epsilon_m}{\pi}} \frac{1}{x_{mn} J_{m+1}(x_{mn})}, \quad Y_{mn}^e = \frac{j\omega\epsilon}{\gamma_{mn}}. \quad (\text{A.19})$$

TE modes

$$\phi_{mn}^h = N_{mn}^h J_m\left(\frac{x'_{mn}\rho}{a}\right) \sin(m\phi) \quad (\text{A.20})$$

$$\vec{E}_t = \hat{z} \times \nabla_t \phi_{mn}^h, \quad \vec{H}_t = Y_{mn}^h \hat{z} \times \vec{E}_t \quad (\text{A.21})$$

where

$$\gamma_{mn}^2 = -\beta_{mn}^2 = (x'_{mn}/a)^2 - k^2 \quad (\text{A.22})$$

$$N_{mn}^h = \sqrt{\frac{\epsilon_m}{\pi}} \frac{1}{\sqrt{(x'_{mn})^2 - m^2} J_m(x'_{mn})}, \quad Y_{mn}^h = \frac{\gamma_{mn}}{j\omega\mu}. \quad (\text{A.23})$$

A.4 Coaxial Waveguide

The radii of inner and outer conductors of a coaxial waveguide are, respectively, a and b .

TEM Mode

$$E_\rho = \frac{1}{\sqrt{2\pi \ln(b/a)}} \frac{1}{\rho}, \quad H_\phi \hat{\phi} = Y^T \hat{z} \times (E_\rho \hat{\rho}) \quad (\text{A.24})$$

where

$$Y^T = \sqrt{\frac{\epsilon}{\mu}}. \quad (\text{A.25})$$

TM Modes

$$\phi_{mn}^e = N_{mn}^e Z_m^{(1)}\left(\frac{x_{mn}\rho}{a}\right) \cos(m\phi) \quad (\text{A.26})$$

$$\vec{E}_t = \nabla_t \phi_{mn}^e, \quad \vec{H}_t = Y_{mn}^e \hat{z} \times \vec{E}_t \quad (\text{A.27})$$

where

$$Z_m^{(1)}\left(\frac{x_{mn}\rho}{a}\right) = J_m\left(\frac{x_{mn}\rho}{a}\right)Y_m(x_{mn}) - Y_m\left(\frac{x_{mn}\rho}{a}\right)J_m(x_{mn}) \quad (\text{A.28})$$

$$Z_m^{(1)}(x_{mn}) = 0, \quad N_{mn}^e = \frac{\sqrt{\pi\epsilon_m}}{2} \left(\left[\frac{J_m(x_{mn})}{J_m(bx_{mn}/a)} \right]^2 - 1 \right)^{-1/2} \quad (\text{A.29})$$

$$Z_m^{(1)}\left(\frac{bx_{mn}}{a}\right) = 0, \quad \gamma_{mn}^2 = -\beta_{mn}^2 = (x_{mn}/a)^2 - k^2, \quad Y_{mn}^e = \frac{j\omega\epsilon}{\gamma_{mn}} \quad (\text{A.30})$$

TE Modes

$$\phi_{mn}^h = N_{mn}^h Z_m^{(2)}\left(\frac{x'_{mn}\rho}{a}\right) \sin(m\phi) \quad (\text{A.31})$$

$$\vec{E}_t = \hat{z} \times \nabla_t \phi_{mn}^h, \quad \vec{H}_t = Y_{mn}^h \hat{z} \times \vec{E}_t \quad (\text{A.32})$$

where

$$Z_m^{(2)}\left(\frac{x_{mn}\rho}{a}\right) = J_m\left(\frac{x_{mn}\rho}{a}\right)Y'_m(x_{mn}) - Y_m\left(\frac{x_{mn}\rho}{a}\right)J'_m(x_{mn}), \quad Z_m^{(2)}(x'_{mn}) = 0 \quad (\text{A.33})$$

$$Z_m^{(2)}\left(\frac{bx'_{mn}}{a}\right) = 0, \quad \gamma_{mn}^2 = -\beta_{mn}^2 = (x'_{mn}/a)^2 - k^2, \quad Y_{mn}^h = \frac{\gamma_{mn}}{j\omega\mu}. \quad (\text{A.34})$$

$$N_{mn}^h = \frac{\sqrt{\epsilon_m\pi}}{2} \left(\left[\frac{J'_m(x'_{mn})}{J'_m(bx'_{mn}/a)} \right]^2 \left[1 - \left(\frac{ma}{bx'_{mn}}\right)^2 \right] - \left[1 - \left(\frac{m}{x'_{mn}}\right)^2 \right] \right)^{-1/2} \quad (\text{A.35})$$

Appendix B

E-Field Mode-Matching Matrices

B.1 Parallel-Plate Waveguide Junction

A junction between two parallel-plate waveguides is illustrated in Figure B.1, where a displacement b exists.

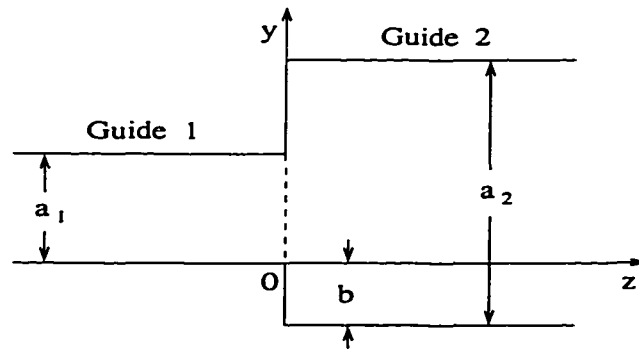


Figure B.1: Parallel-plate to parallel-plate waveguide junction.

$$\mathbf{M} = \begin{bmatrix} [M_{1,1}^{TT}] & [0] & [0] \\ [0] & [M_{n,m}^{hh}] & [0] \\ [M_{n,1}^{eT}] & [0] & [M_{n,m}^{ee}] \end{bmatrix} \quad (\text{B.1})$$

where

$$M_{1,1}^{TT} = \sqrt{\frac{a_1}{a_2}} \quad (\text{B.2})$$

$$M_{n,m}^{hh} = \frac{2}{a_1 a_2} SS(n, m, a_1, a_2, b) \quad (\text{B.3})$$

$$M_{n,1}^{eT} = \sqrt{\frac{2a_2}{a_1}} \frac{1}{n\pi} \left[\sin \frac{n\pi(a_1 + b)}{a_2} - \sin \frac{n\pi b}{a_2} \right] \quad (\text{B.4})$$

$$M_{n,m}^{ee} = \frac{2}{a_1 a_2} CC(n, m, a_1, a_2, b) \quad (\text{B.5})$$

with

$$SS(n, m, a_1, a_2, b) = \frac{m\pi \sin(n\pi b/a_2) - (-1)^m \sin(n\pi(a_1 + b)/a_2)}{a_1 ((m\pi/a_1)^2 - (n\pi/a_2)^2)} \quad (\text{B.6})$$

$$CC(n, m, a_1, a_2, b) = \frac{n\pi \sin(n\pi b/a_2) - (-1)^m \sin(n\pi(a_1 + b)/a_2)}{a_2 ((m\pi/a_1)^2 - (n\pi/a_2)^2)}. \quad (\text{B.7})$$

B.2 Rectangular Waveguide Junction

A rectangular-to-rectangular waveguide junction is shown in Figure B.2.

$$\mathbf{M} = \begin{bmatrix} [M_{nm,ki}^{hh}] & [0] \\ [M_{nm,ki}^{eh}] & [M_{nm,ki}^{ee}] \end{bmatrix} \quad (\text{B.8})$$

where

$$M_{nm,ki}^{hh} = K_{c,1ki}^2 N_{1,ki} N_{2,nm} CC(n, k, a_1, a_2, c) CC(m, i, b_1, b_2, d) \quad (\text{B.9})$$

$$M_{nm,ki}^{eh} = N_{1,ki} N_{2,nm} \left[\frac{n\pi}{a_2} \frac{i\pi}{b_1} CC(n, k, a_1, a_2, c) SS(m, i, b_1, b_2, d) - \frac{m\pi}{b_2} \frac{k\pi}{a_1} SS(n, k, a_1, a_2, c) CC(m, i, b_1, b_2, d) \right] \quad (\text{B.10})$$

$$M_{nm,ki}^{ee} = K_{c,2nm}^2 N_{1,ki} N_{2,nm} SS(n, k, a_1, a_2, c) SS(m, i, b_1, b_2, d). \quad (\text{B.11})$$

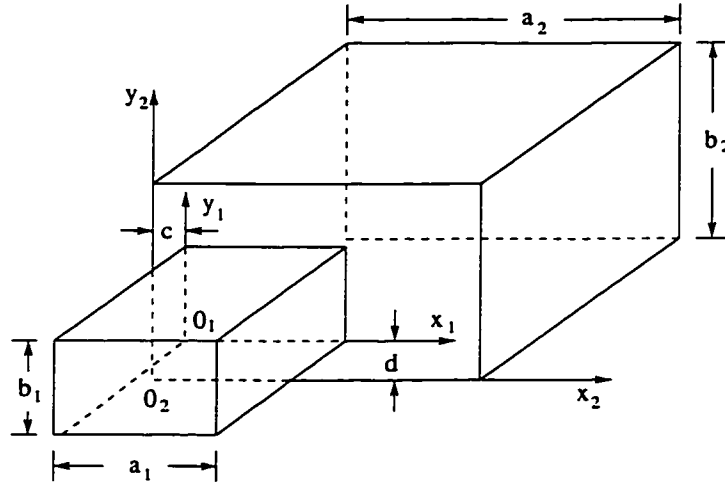


Figure B.2: Rectangular-to-rectangular waveguide junction.

B.3 Circular-to-Circular Waveguide Junction

A junction between two collinear circular waveguides is shown in Figure B.3.

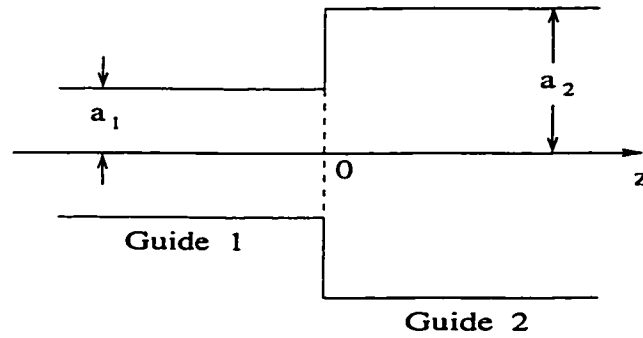


Figure B.3: Circular-to-circular waveguide junction.

$$M = \begin{bmatrix} [M_{nm,ki}^{hh}] & [0] \\ [M_{nm,ki}^{eh}] & [M_{nm,ki}^{ee}] \end{bmatrix} \quad (\text{B.12})$$

where

$$M_{nm,ki}^{hh} = \delta_{nk} \frac{\pi}{a_1 a_2} N_{ki}^h N_{nm}^h (x'_{ki})^2 x'_{nm} \frac{J_k(x'_{ki}) J'_k(\frac{a_1 x'_{nm}}{a_2})}{(x'_{ki}/a_1)^2 - (x'_{nm}/a_2)^2} \quad (\text{B.13})$$

$$M_{nm,ki}^{eh} = -n\pi\delta_{nk}N_{ki}^hN_{nm}^eJ_k(x'_{ki})J_k\left(\frac{a_1x_{nm}}{a_2}\right) \quad (\text{B.14})$$

$$M_{nm,ki}^{ee} = \frac{-2\pi}{\epsilon_n}N_{ki}^eN_{nm}^ex_{ki}\left(\frac{x_{nm}}{a_2}\right)^2\frac{J'_k(x_{ki})J_k\left(\frac{a_1x_{nm}}{a_2}\right)}{(x_{ki}/a_1)^2 - (x_{nm}/a_2)^2}. \quad (\text{B.15})$$

B.4 Coaxial-to-Circular Waveguide Junction

A junction between a coaxial waveguide and a circular waveguide is illustrated in Figure B.4.

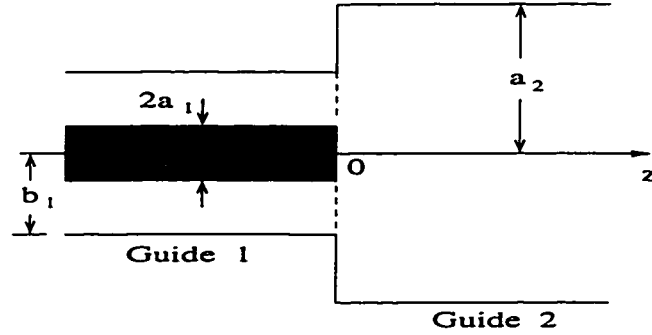


Figure B.4: Coaxial-to-circular waveguide junction.

$$\mathbf{M} = \begin{bmatrix} [0] & [M_{nm,ki}^{hh}] & [0] \\ [M_{nm,1}^{eT}] & [M_{nm,ki}^{eh}] & [M_{nm,ki}^{ee}] \end{bmatrix} \quad (\text{B.16})$$

where

$$M_{nm,ki}^{hh} = \delta_{nk}\frac{2x'_{ki}x'_{nm}}{a_1a_2}\frac{N_{ki}^hN_{nm}^h}{(x'_{ki}/a_1)^2 - (x'_{nm}/a_2)^2}\left[\frac{J'_k(x'_{ki})}{J'_k(b_1x'_{ki}/a_1)}J'_n\left(\frac{b_1x'_{nm}}{a_2}\right) - J'_n\left(\frac{a_1x'_{nm}}{a_2}\right)\right] \quad (\text{B.17})$$

$$M_{nm,1}^{eT} = \delta_{n0}\sqrt{\frac{2\pi}{\ln(b_1/a_1)}}N_{nm}^e\left[J_n\left(\frac{b_1x_{nm}}{a_2}\right) - J_n\left(\frac{a_1x_{nm}}{a_2}\right)\right] \quad (\text{B.18})$$

$$M_{nm,ki}^{eh} = \frac{-2n}{x'_{ki}}\delta_{nk}N_{ki}^hN_{nm}^e\left[\frac{a_1J'_k(x'_{ki})}{b_1J'_k(b_1x'_{ki}/a_1)}J_n\left(\frac{b_1x_{nm}}{a_2}\right) - J_n\left(\frac{a_1x_{nm}}{a_2}\right)\right] \quad (\text{B.19})$$

$$M_{nm,ki}^{ee} = \frac{4\delta_{nk}}{\epsilon_n}\frac{N_{ki}^eN_{nm}^e}{(a_2x_{ki}/a_1x_{nm})^2 - 1}\left[\frac{J_k(x_{ki})}{J_k(b_1x_{ki}/a_1)}J_n\left(\frac{b_1x_{nm}}{a_2}\right) - J_n\left(\frac{a_1x_{nm}}{a_2}\right)\right]. \quad (\text{B.20})$$

B.5 Coaxial-to-Coaxial Waveguide Junction

A junction between two coaxial waveguides with a shift d between their axes is shown in Figure B.5.

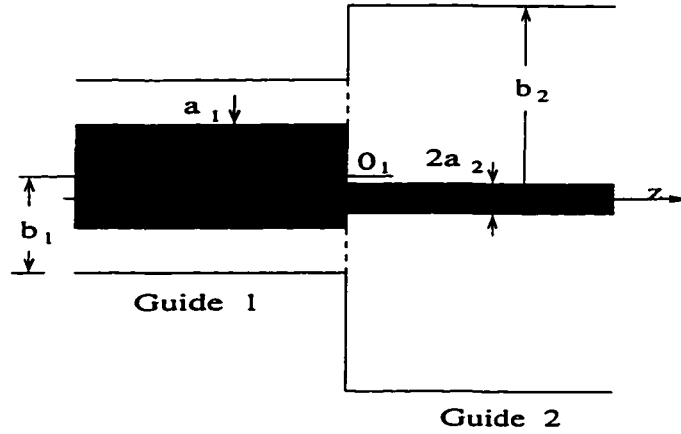


Figure B.5: Junction between two noncollinear coaxial waveguides.

$$\mathbf{M} = \begin{bmatrix} [M_{1,1}^{TT}] & [M_{1,ki}^{Th}] & [0] \\ [0] & [M_{nm,ki}^{hh}] & [0] \\ [M_{nm,1}^{eT}] & [M_{nm,ki}^{eh}] & [M_{nm,ki}^{ee}] \end{bmatrix} \quad (\text{B.21})$$

where

$$M_{1,1}^{TT} = \sqrt{\frac{\ln(b_1/a_1)}{\ln(b_2/a_2)}} \quad (\text{B.22})$$

$$M_{1,ki}^{Th} = \sqrt{\frac{2}{\pi \ln(b_2/a_2)}} \frac{N_{ki}^h}{x'_{ki}} \left[\left(\frac{d}{b_1}\right)^k \frac{a_1 J'_k(x'_{ki})}{b_1 J'_k(b_1 x'_{ki}/a_1)} - \left(\frac{d}{a_1}\right)^k \right] \quad (\text{B.23})$$

$$M_{nm,ki}^{hh} = \frac{2}{a_1 a_2} \frac{x'_{ki} x'_{nm} N_{ki}^h N_{nm}^h}{\left(\frac{x'_{ki}}{a_1}\right)^2 - \left(\frac{x'_{nm}}{a_2}\right)^2} \left[\frac{J'_k(x'_{ki})}{J'_k(b_1 x'_{ki}/a_1)} Z_n^{(2)}\left(\frac{b_1 x'_{nm}}{a_2}\right) - Z_n^{(2)}\left(\frac{a_1 x'_{nm}}{a_2}\right) \right] Q' \quad (\text{B.24})$$

$$M_{nm,1}^{eT} = (-1)^{-n} \sqrt{\frac{2\pi}{\ln(b_1/a_1)}} N_{nm}^e \left[Z_n^{(1)}\left(\frac{b_1 x_{nm}}{a_2}\right) - Z_n^{(1)}\left(\frac{a_1 x_{nm}}{a_2}\right) \right] J_n\left(\frac{d x_{nm}}{a_2}\right) \quad (\text{B.25})$$

$$M_{nm,ki}^{eh} = \frac{-2n}{x'_{ki}} N_{ki}^h N_{nm}^e \left[\frac{a_1 J'_k(x'_{ki})}{b_1 J'_k(b_1 x'_{ki}/a_1)} Z_n^{(1)}\left(\frac{b_1 x_{nm}}{a_2}\right) - Z_n^{(1)}\left(\frac{a_1 x_{nm}}{a_2}\right) \right] Q \quad (\text{B.26})$$

$$M_{nm,ki}^{ee} = 2 \frac{N_{ki}^e N_{nm}^e}{(a_2 x_{ki}/a_1 x_{nm})^2 - 1} \left[\frac{J_k(x_{ki})}{J_k(b_1 x_{ki}/a_1)} Z_n^{(1)}\left(\frac{b_1 x_{nm}}{a_2}\right) - Z_n^{(1)}\left(\frac{a_1 x_{nm}}{a_2}\right) \right] Q \quad (\text{B.27})$$

with

$$Q = J_{n-k}\left(\frac{dx_{nm}}{a_2}\right) + (-1)^n J_{n+k}\left(\frac{dx_{nm}}{a_2}\right) \quad (\text{B.28})$$

$$Q' = J_{n-k}\left(\frac{dx'_{nm}}{a_2}\right) - (-1)^n J_{n+k}\left(\frac{dx'_{nm}}{a_2}\right). \quad (\text{B.29})$$

Appendix C

Expressions of Matrix Elements in (2.49)-(2.56)

The elements of the matrices occurring in equations (2.49)-(2.56) are as follows:

$$P_{Bmn} = F_{mn}(D, d) \frac{\epsilon_{r1} \epsilon_m \epsilon_n \gamma_n^{II} J_0(\gamma_n^{II} a_0)}{\epsilon_r^{II} d D J_1(\gamma_n^{II} a_0)} \quad (C.1)$$

$$M_{IIA_{mn}} = -F_{nm}(D, d) \frac{U'_{1n}(a_0)}{\gamma_{1n}^2}, \quad M_{IIB_{mn}} = -F_{nm}(D, d) \frac{V'_{1n}(a_0)}{\gamma_{1n}^2} \quad (C.2)$$

$$M_{2A_{mn}} = -\frac{\epsilon_m}{L} F_{nm}(D, L) \frac{U'_{1n}(a_1)}{\gamma_{1n}^2}, \quad M_{2B_{mn}} = -\frac{\epsilon_m}{L} F_{nm}(D, L) \frac{V'_{1n}(a_1)}{\gamma_{1n}^2} \quad (C.3)$$

$$M_{IIC_{mn}} = e_{1n\rho}(a_0) S_{mn}(d, D), \quad M_{2C_{mn}} = \frac{\epsilon_m}{d} e_{1n\rho}(a_1) S_{mn}(L, D) \quad (C.4)$$

$$M_{3A_{mn}} = -\frac{\epsilon_m}{L} F_{mn}(H, L) \frac{U'_{3n}(a_2)}{\gamma_{3n}^2}, \quad M_{3B_{mn}} = -\frac{\epsilon_m}{L} F_{mn}(H, L) \frac{V'_{3n}(a_2)}{\gamma_{3n}^2} \quad (C.5)$$

$$Y_{1A_{mn}} = -\frac{U'_{2n}(a_1) \delta_{nm}}{\gamma_{2n}^2}, \quad Y_{1B_{mn}} = -\frac{V'_{2n}(a_1) \delta_{nm}}{\gamma_{2n}^2} \quad (C.6)$$

$$Y_{3A_{mn}} = -\frac{U'_{2n}(a_2) \delta_{nm}}{\gamma_{2n}^2}, \quad Y_{3B_{mn}} = -\frac{V'_{2n}(a_2) \delta_{nm}}{\gamma_{2n}^2} \quad (C.7)$$

$$P_{A_{nm}} = \frac{\epsilon_{1r} \epsilon_m}{\epsilon_{r2} D} F_{nm}(D, L), \quad P_{D_{nm}} = \frac{\epsilon_{r3} \epsilon_m}{\epsilon_{r2} H} F_{nm}(H, L) \quad (C.8)$$

$$M_{IAmn} = (-1)^{(n+1)} \frac{2\pi}{\gamma_{1n}^2} \int_{a_I}^{b_I} U'_{1n}(\rho) e_{1m\rho}(\rho) \rho d\rho \quad (\text{C.9})$$

$$M_{IBmn} = (-1)^{(n+1)} \frac{2\pi}{\gamma_{1n}^2} \int_{a_I}^{b_I} V'_{1n}(\rho) e_{1m\rho}(\rho) \rho d\rho \quad (\text{C.10})$$

$$P_{Cmn} = \left[\frac{j\omega\epsilon_1}{\alpha_n \tan(\alpha_n D)} \right] M_{ICnm} \quad (\text{C.11})$$

$$M_{ICmn} = 2\pi \int_{a_I}^{b_I} e_{Im\rho}(\rho) e_{1n\rho}(\rho) \rho d\rho \quad (\text{C.12})$$

where

$$F_{mn}(d, l) = \int_0^l \cos \frac{m\pi z}{d} \cos \frac{n\pi z}{l} dz$$

$$S_{mn}(l, d) = \int_0^l \cos \frac{m\pi z}{l} \frac{\cos(\alpha_n z)}{\cos(\alpha_n d)} dz$$

and $\delta_{nm} = 1$ for $n = m$; $\delta_{nm} = 0$ for $n \neq m$. All of the integrals given above can be evaluated in closed form (Abramowitz and Stegun [56], Ch.11).

Appendix D

Derivation of (4.58)

The procedures for calculating the radiation pattern of a stacked circular microstrip antenna (shown in Figure 4.6) were outlined in Section 4.3. This appendix details the derivation of equation (4.58).

From equations(A.20) and (A.21) in Appendix A, one has

$$\begin{aligned} \vec{e}_{6,ni}^h(\rho', \phi') = N_{6,ni}^h & \left[-\frac{n}{\rho'} J_n\left(\frac{x'_{6,ni}}{b_1} \rho'\right) \cos(n\phi') \hat{\rho}' \right. \\ & \left. + \frac{x'_{6,ni}}{b_1} J'_n\left(\frac{x'_{6,ni}}{b_1} \rho'\right) \sin(n\phi') \hat{\phi}' \right] \end{aligned} \quad (\text{D.1})$$

for ni -th TE mode in the last circular waveguide. Combining the following relations

$$\hat{\rho}' = \hat{x} \cos \phi' + \hat{y} \sin \phi'$$

$$\hat{\phi}' = -\hat{x} \sin \phi' + \hat{y} \cos \phi'$$

$$\hat{x} = \hat{r} \sin \theta \cos \phi + \hat{\theta} \cos \theta \cos \phi - \hat{\phi} \sin \phi$$

$$\hat{y} = \hat{r} \sin \theta \sin \phi + \hat{\theta} \cos \theta \sin \phi + \hat{\phi} \cos \phi$$

yields

$$\hat{\rho}' = \hat{r} \sin \theta \cos(\phi - \phi') + \hat{\theta} \cos \theta \cos(\phi - \phi') - \hat{\phi} \sin(\phi - \phi') \quad (\text{D.2})$$

$$\hat{\phi}' = \hat{r} \sin \theta \sin(\phi - \phi') + \hat{\theta} \sin \theta \cos(\phi - \phi') + \hat{\phi} \cos(\phi - \phi') \quad (\text{D.3})$$

Substituting (D.1) into (4.56) and using the above relations, one gets

$$\begin{aligned} \hat{r} \times (\hat{e}_{\delta,ni}^h \times \hat{z}) &= N_{\delta,ni}^h \left(\frac{x'_{\delta,ni}}{b_1} J'_n \left(\frac{x'_{\delta,ni}}{b_1} \rho' \right) \sin(n\phi') [\hat{\theta} \sin(\phi - \phi') + \hat{\phi} \cos \theta \cos(\phi - \phi')] \right. \\ &\quad \left. + \frac{n}{\rho'} J_n \left(\frac{x'_{\delta,ni}}{b_1} \rho' \right) \cos(n\phi') [-\hat{\theta} \cos(\phi - \phi') + \hat{\phi} \cos \theta \sin(\phi - \phi')] \right). \end{aligned} \quad (\text{D.4})$$

Substituting the expression (D.4) for the equivalent magnetic current into (4.57) and expanding $\sin(n\phi')$ and $\cos(n\phi')$ into

$$\sin(n\phi') = -\sin(n\phi - n\phi' - n\phi) = -\sin(n\phi - n\phi') \cos(n\phi) + \cos(n\phi - n\phi') \sin(n\phi)$$

$$\cos(n\phi') = \cos(n\phi - n\phi' - n\phi) = \cos(n\phi - n\phi') \cos(n\phi) + \sin(n\phi - n\phi') \sin(n\phi)$$

and using

$$\int_0^{2\pi} \exp(jz \cos \phi) \cos(n\phi) d\phi = 2\pi j^n J_n(z)$$

$$\int_0^{2\pi} \exp(jz \cos \phi) \sin(n\phi) d\phi = 0$$

$$J_{n+1}(z) - J_{n-1}(z) = 2J'_n(z)$$

$$J_{n+1}(z) + J_{n-1}(z) = \frac{2n}{z} J'_n(z)$$

one can derive

$$\begin{aligned} \vec{E}_{H,ni} &= \frac{j^n k_0 \exp(-jk_0 r)}{r} (-n) N_{\delta,ni}^h \cos(n\phi) \hat{\theta} \int_0^{b_1} \left[\frac{x'_{\delta,ni}}{b_1} J'_n \left(\frac{x'_{\delta,ni}}{b_1} \rho' \right) \frac{J_n(k_0 \rho' \sin \theta)}{k_0 \sin \theta} \right. \\ &\quad \left. + J_n \left(\frac{x'_{\delta,ni}}{b_1} \rho' \right) J'_n(k_0 \rho' \sin \theta) \right] d\rho' + \frac{j^n k_0 \exp(-jk_0 r)}{r} N_{\delta,ni}^h \cos \theta \sin(n\phi) \hat{\phi} \\ &\int_0^{b_1} \left[\frac{x'_{\delta,ni}}{b_1} J'_n \left(\frac{x'_{\delta,ni}}{b_1} \rho' \right) J'_n(k_0 \rho' \sin \theta) + \frac{n^2}{k_0 \rho' \sin \theta} J_n \left(\frac{x'_{\delta,ni}}{b_1} \rho' \right) J_n(k_0 \rho' \sin \theta) \right] d\rho' \quad (\text{D.5}) \end{aligned}$$

The integral in (D.5) can be worked out and the final expression is given in (4.58a).

Similarly, from equation (A.16) and (A.17), one gets

$$\begin{aligned} \vec{e}_{\delta,ni}(\rho', \phi') = N_{\delta,ni}^e & \left[\frac{x_{\delta,ni}}{b_1} J_n' \left(\frac{x_{\delta,ni}}{b_1} \rho' \right) \cos(n\phi') \right] \hat{\rho}' \\ & - \frac{n}{\rho'} J_n \left(\frac{x_{\delta,ni}}{b_1} \rho' \right) \sin(n\phi') \hat{\phi}' \end{aligned} \quad (\text{D.6})$$

for ni -th TM mode in the sixth circular waveguide.

Following the same procedures one can obtain

$$\begin{aligned} \vec{E}_{E,ni} = & \frac{j^n k_0 \exp(-jk_0 r)}{r} N_{\delta,ni}^e \cos(n\phi) \hat{\theta} \int_0^{b_1} \left[n^2 J_n \left(\frac{x'_{\delta,ni}}{b_1} \rho' \right) \frac{J_n(k_0 \rho' \sin \theta)}{k_0 \rho' \sin \theta} \right. \\ & + \left. \frac{x'_{\delta,ni}}{b_1} J_n' \left(\frac{x'_{\delta,ni}}{b_1} \rho' \right) J_n'(k_0 \rho' \sin \theta) \right] d\rho' - \frac{j^n k_0 \exp(-jk_0 r)}{r} N_{\delta,ni}^e n \cos \theta \sin(n\phi) \hat{\phi} \\ & \int_0^{b_1} \left[J_n \left(\frac{x'_{\delta,ni}}{b_1} \rho' \right) J_n'(k_0 \rho' \sin \theta) + \frac{x'_{\delta,ni}}{b_1} J_n' \left(\frac{x'_{\delta,ni}}{b_1} \rho' \right) \frac{J_n(k_0 \rho' \sin \theta)}{k_0 \sin \theta} \right] d\rho' \end{aligned} \quad (\text{D.7})$$

The integral in (D.7) can be easily worked out and the derived expression is given in (4.58b).

Bibliography

- [1] R.F. Harrington. *Field Computation by Moment Method*. Macmillan, New York, 1968.
- [2] K.S. Yee. Numerical solution of initial boundary value problems involving maxwell's equations in isotropic media. *IEEE Trans. Antennas Propagat.*, AP-14:302-307, 1966.
- [3] R.W.P. King. *The Theory of Linear Antennas*. Harvard University Press, Cambridge, MA, 1956.
- [4] R.W.P. King. *Tables of Antenna Characteristics*. IFI/Plenum, New York, 1971.
- [5] D.C. Chang. On the electrically thick monopole: Part I-theoretical solutions. *IEEE Trans. Antennas Propagat.*, AP-14(1):58-64, 1966.
- [6] M.E. Morris. Analysis of a finite length tubular monopole antenna driven by a coaxial line. Tech. rep. sand79-1557, Sandia Nati. Lab., Albuquerque, N.M., 1980.

- [7] J.S. Maloney G.S. Smith and W.R. Scott. Accurate computation of the radiation from simple antennas using the finite difference time-domain method. *IEEE Trans. Antennas Propagat.*, AP-38(7):1059–1068, 1990.
- [8] T. Do-Nhat and R.H. MacPhie. The admittance of a monopole antenna fed through a ground plane by a coaxial line. *IEEE Trans. Antennas Propagat.*, AP-39:1243–1247, 1991.
- [9] A.J. Poggio and P.E. Mayes. Pattern bandwidth optimization of the sleeve monopole antenna. *IEEE Trans. Antennas Propagat.*, AP-14:643–645, 1966.
- [10] J. Taylor. *The Sleeve Antenna*. Doctoral dissertation, Harvard University, Cambridge, MA, 1950.
- [11] L.W. Rispin and D.C.Chang. Wire and loop antennas. In Y.T. Lo and S.W. Lee, editors, *Antenna Handbook*, chapter 7, pages 7.23–7.36. Van Nostrand Reinhold, New York, 1988.
- [12] A.D. Wunsch. Fourier series treatment of the sleeve monopole antenna. *IEE Proceedings-H*, 135(4):217–225, 1988.
- [13] K. Lamensdorf. An experimental investigation of dielectric-coated antennas. *IEEE Trans. Antennas Propagat.*, AP-15(6):767–771, 1967.
- [14] C.Y. Ting. Theoretical study of finite dielectric-coated cylindrical antenna. *J. Mathematical Physics*, 10(3):480–493, 1969.
- [15] J.H. Richmond and E.H. Newman. Dielectric coated wire antennas. *Radio Science*, 11(1):12–20, 1976.
- [16] B.P. Sinha and S.A. Saoudy. Rigorous analysis of finite length insulated antenna in air. *IEEE Trans, Antennas Propagat.*, AP-38(8):1253–1258, 1986.

- [17] C.L. Chi and N.G. Alexopoulos. Radiation by a probe through a substrate. *IEEE Trans. Antennas Propagat.*, AP-34:1080–1091, 1986.
- [18] R.C. Hall and J.R. Mosig. Vertical monopole embedded in a dielectric substrate. *Proc. IEE*, 136-H(6):462–468, 1989.
- [19] R.W.P. King and G.S. Smith. *Antennas in Matter: Fundamentals, Theory and Application*. MIT Press, Cambridge, MA, 1981.
- [20] R.W.P. King K.M. Lee S.R. Mishra and G.S. Smith. Insulated linear antenna: Theory and experiment. *J. Appl. Phys.*, 45:1668–1697, 1974.
- [21] R.W.P. King S.R. Mishra K.M. Lee and G.S. Smith. The insulated monopole: admittance and junction effects. *IEEE Trans. Antennas Propagat.*, AP-23(2):172–177, 1975.
- [22] T.T. Wu R.W.P. King and D.V. Giri. The insulated dipole antenna in a relatively dense medium. *Radio Science*, 8:699–709, 1973.
- [23] K.M. Lee. Insulated linear antenna. In J.A. Kong, editor, *Research Topics in Electromagnetic Wave Theory*, pages 235–263. John Wiley & Sons, New York, 1981.
- [24] K.M. Lee T.T. Wu and R.W.P. King. Theory of an insulated linear antenna in a dissipative medium. *Radio Science*, 12:195–203, 1977.
- [25] J. Bardeen. The diffraction of a circularly symmetrical electromagnetic wave by a coaxial circular disc of infinity conductivity. *Phys. Rev.*, 36:1482–1488, 1930.
- [26] A.S. Meier and W.P. Summers. Measured impedance of vertical antennas over finite ground plane. *Proc. IEEE*, 37:609–616, 1949.

- [27] A. Leitner and R.D. Spence. Effect of a circular ground plane on antenna radiation. *J. Appl. Phys.*, 21:1001–1006, 1950.
- [28] R.F. Hahn and J.G. Fikioris. Impedance and radiation pattern of antennas above flat discs. *IEEE Trans. Antennas Propagat.*, AP-21(1):97–100, 1973.
- [29] J.E. Storer. The impedance of an antenna over a large circular screen. *J. Appl. Phys.*, 22:1058–1066, 1951.
- [30] G.A. Thiele and T.H. Newhouse. A hybrid technique for combining moment methods and the geometrical theory of diffraction. *IEEE Trans. Antennas Propagat.*, AP-23(1):62–69, 1975.
- [31] J.R. Wait and W.J. Surtees. Impedance of top-loaded antenna of arbitrary length over a circular grounded screen. *J. Appl. Phys.*, 25:553–555, 1954.
- [32] E.K. Yung and C.M. Butler. Coaxial-line driven monopole in an electrically thicker conducting cylinder over a ground plane. *IEE Proc.*, 131-H:54–60, 1984.
- [33] J.H. Richmond. Monopole antenna on circular disk. *IEEE Trans. Antennas Propagat.*, AP-32:1282–1287, 1984.
- [34] M.M. Weiner S.P. Cruse C.C. Li and W.J. Wilson. *Monopole Elements in Circular Ground Planes*. Artech House, Norwood, MA, 1987.
- [35] G.A. Deschamps. Microstrip microwave antennas. In *Third USAF Symposium on Antennas*, 1953.
- [36] Y.T. Lo D. Solomon and W.F. Richards. Theory and experiment on microstrip antennas. *IEEE Trans. Antennas Propagat.*, AP-27(3):137–145, 1979.

- [37] W.C. Chew and J.A. Kong. Analysis of a circular microstrip disk antenna with a thick dielectric substrate. *IEEE Trans. Antennas Propagat.*, AP-29(1):68–76, 1981.
- [38] K. Araki and T. Itoh. Hankel transform domain analysis of open circular microstrip radiating structures. *IEEE Trans. Antennas Propagat.*, AP-29(1):84–89, 1981.
- [39] S. Yano and A. Ishimaru. A theoretical study of the input impedance of a circular microstrip disk antenna. *IEEE Trans. Antennas Propagat.*, AP-29(1):77–83, 1981.
- [40] M. Davidovitz and Y.T. Lo. Input impedance of a probe-fed circular microstrip antenna with thick substrate. *IEEE Trans. Antennas Propagat.*, AP-34:905–911, 1986.
- [41] M.C. Bailey and M.D. Deshpande. Analysis of elliptical and circular microstrip antennas using moment method. *IEEE Trans. Antennas Propagat.*, AP-33(9):954–959, 1985.
- [42] A.A. Kishk and L. Shafai. The effect of various parameters of circular microstrip antennas on their radiation efficiency and the mode excitation. *IEEE Trans. Antennas Propagat.*, AP-34(8):969–976, 1986.
- [43] C. Wu K.L. Wu Z.Q. Bi and J. Litva. Accurate characterization of planar printed antennas using finite-difference time-domain method. *IEEE Trans. Antennas Propagat.*, AP-40:526–534, 1992.
- [44] J.T. Aberle D.M. Pozar and C.R. Birtcher. Evaluation of input impedance and radar cross section of probe-fed microstrip patch elements using an accurate feed model. *IEEE Trans. Antennas Propagat.*, AP-39(12):1691–1696, 1991.

- [45] W.C. Chew. A broad-band annular-ring microstrip antenna. *IEEE Trans. Antennas Propagat.*, AP-30(5):918–922, 1982.
- [46] S.M. Ali W.C. Chew and J.A. Kong. Vector Hankel transform analysis of annular-ring microstrip antenna. *IEEE Trans. Antennas Propagat.*, AP-30(3):637–644, 1982.
- [47] Z.Nie W.C. Chew and Y.T. Lo. Analysis of the annular-ring-loaded circular disk microstrip antenna. *IEEE Trans. Antennas Propagat.*, AP-38(6):806–813, 1990.
- [48] S.A. Long and M.D. Walton. A dual-frequency stacked circular-disk antenna. *IEEE Trans. Antennas Propagat.*, AP-27(2):270–273, 1979.
- [49] A.N. Tulintseff S.M. Ali and J.A. Kong. Input impedance of a probe-fed stacked circular microstrip antenna. *IEEE Trans. Antennas Propagat.*, AP-39(3):381–390, 1991.
- [50] J.S. Dahele K.F. Lee and D.P. Wood. Dual-frequency stacked annular-ring microstrip antenna. *IEEE Trans. Antennas Propagat.*, AP-35:1281–1285, 1987.
- [51] D.M. Pozar. Radiation and scattering from a microstrip patch on a uniaxial substrate. *IEEE Trans. Antennas Propagat.*, AP-35(6):613–621, 1987.
- [52] R.M. Nelson D.A. Rogers and A. Gomes D'Assuncao. Resonant frequency of a rectangular microstrip patch on several uniaxial substrates. *IEEE Trans. Antennas Propagat.*, AP-38(9):973–981, 1990.
- [53] R.F. Harrington. *Time-Harmonic Electromagnetic Fields*. McGraw-Hill, New York, 1961.

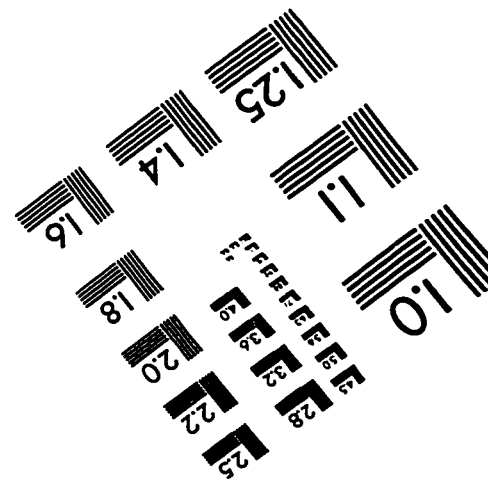
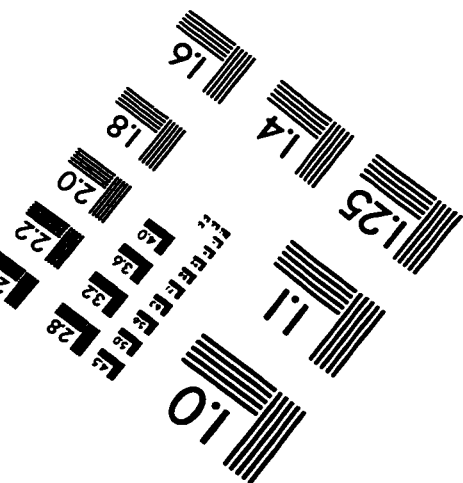
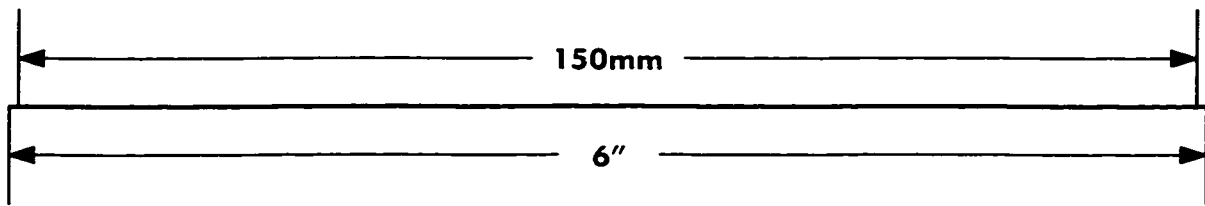
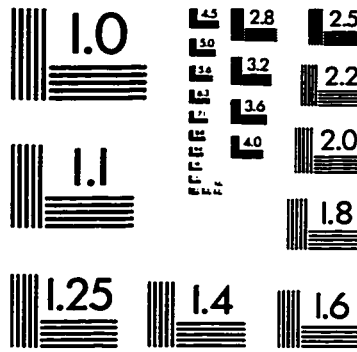
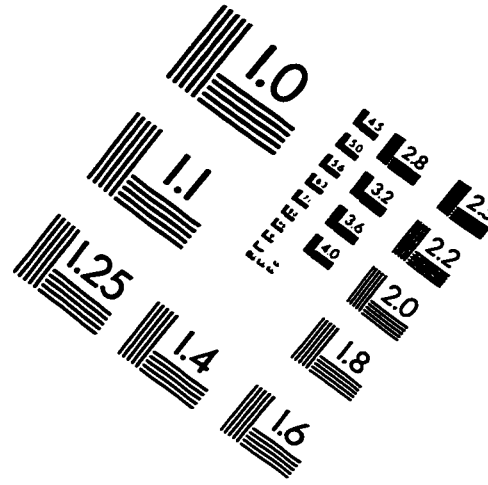
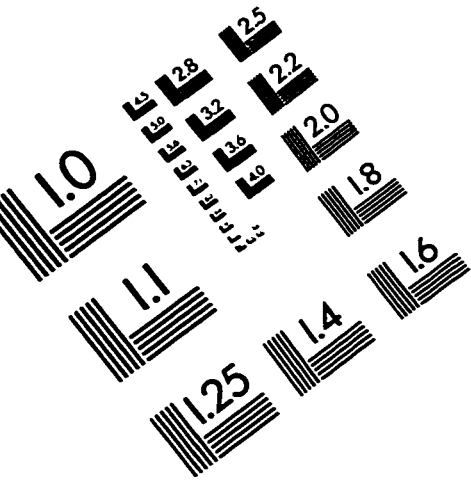
- [54] E. Kuhn. A mode-matching method for solving field problems in waveguide and resonator circuits. *Arch.Elek. Ubertragung*, 27:511–518, 1973.
- [55] F. Arndt et al. Optimized E-plane T-junction series power dividers. *IEEE Trans. Microwave Theory and Tech.*, MTT-35(11):1052–1059, 1987.
- [56] M. Abramowitz and I.A. Stegun. *Handbook of Mathematical Functions*. Dover, New York, 1965.
- [57] C.A. Balanis. *Antenna Theory: Analysis and Design*. Harper & Row, New York, 1982.
- [58] Z. Shen and R.H. MacPhie. Modal expansion analysis of monopole antennas driven from a coaxial line. *Radio Science*, 31(5):1037–1046, 1996.
- [59] R. Mittra and S.W. Lee. *Analytical Techniques in the Theory of Guided Waves*. Macmillan, New York, 1971.
- [60] E.O. Hartig. *Circular Apertures and Their Effects on Half-Dipole Impedance*. Doctoral dissertation, Harvard University, Cambridge, MA, 1950.
- [61] P.I. Somlo. The computation of coaxial line step capacitances. *IEEE Trans. Microwave Theory and Tech.*, MTT-15(1):48–53, 1967.
- [62] Z. Shen and R.H. MacPhie. Rigorous evaluation of the input impedance of a sleeve monopole by modal-expansion method. *IEEE Trans. Antennas Propagat.*, AP-44(12):1584–1591, 1996.
- [63] Z. Shen and R.H. MacPhie. Modeling of a monopole partially buried in a grounded dielectric substrate by the modal expansion method. *IEEE Trans. Antennas Propagat.*, AP-44(11):1535–1536, 1996.

- [64] Z. Shen and R.H. MacPhie. Input impedance of a multilayer insulated monopole antenna. In *Proc. of 1996 IEEE AP-S Symposium*, number 1, pages 338–341, Baltimore, 1996.
- [65] W.D. Murphy V. Rokhlin and M.S. Vassiliou. Acceleration methods for the iterative solution of electromagnetic scattering problems. *Radio Science*, 28(1):1–12, 1993.
- [66] Z. Shen and R.H. MacPhie. A simple method for calculating the reflection coefficient of open-ended waveguides. *IEEE Trans. Microwave Theory Tech.*, MTT-45(4):546–548, 1997.
- [67] R. Safavi-Naini and R.H. MacPhie. On solving waveguide junction scattering problems by the conservation of complex power technique. *IEEE Trans. Microwave Theory Tech.*, MTT-29:337–343, 1981.
- [68] Z. Shen and R.H. MacPhie. An improved modal expansion method for two cascaded junctions and its application to waveguide filters. *IEEE Trans. Microwave Theory Tech.*, MTT-43(12):2719–2722, 1995.
- [69] A.S. Omar and K. Schunemann. Transmission matrix representation of finline discontinuities. *IEEE Trans. Microwave Theory Tech.*, MTT-33(9):765–770, 1985.
- [70] R.R. Mansour and R.H. MacPhie. An improved transmission matrix formulation of cascaded discontinuities and its application to E-plane circuits. *IEEE Trans. Microwave Theory Tech.*, MTT-34(12):1490–1498, 1986.
- [71] F.E. Gardiol. Open-ended waveguides: principles and applications. In P.W. Hawkes, editor, *Advances in Electronics and Electron Physics*, volume 63, chapter 7, pages 139–187. 1985.

- [72] H. Levine and C.H. Papas. Theory of the circular diffraction antenna. *J. Appl. Phys.*, 22(1):29–43, 1951.
- [73] R.H. MacPhie and A.I. Zaghoul. Radiation from a rectangular waveguide with infinite flange—exact solution by the correlation matrix method. *IEEE Trans. Antennas Propagat.*, AP-28(4):497–503, 1980.
- [74] J.R. Mosig J.E. Besson M. Gex-Fabry and F.E Gardiol. Reflection of an open-ended coaxial line and application to nondestructive measurement of materials. *IEEE Trans. Instrum. Meas.*, IM-30:46–51, 1981.
- [75] H. Baudrand J.W. Tao and J. Atechian. Study of radiating properties of open-ended rectangular waveguide. *IEEE Trans. Antennas Propagat.*, AP-36(8):1071–1077, 1988.
- [76] J.R. Mautz and R.F. Harrington. Transmission from a rectangular waveguide into half space through a rectangular aperture. *IEEE Trans. Microwave Theory and Tech.*, MTT-26:44–45, 1978.
- [77] J.A. Encinar and J.M. Rebollar. Convergence of numerical solutions of open-ended waveguide by modal analysis and hybrid modal-spectral techniques. *IEEE Trans. Microwave Theory Tech.*, MTT-34(7):809–814, 1986.
- [78] Z. Shen and R.H. MacPhie. Waveguide modal analysis of single and stacked probe-fed microstrip antennas with circular geometries. In *Proc. of 1997 IEEE AP-S Symposium*, number 1, pages 338–341, Montreal, 1997.
- [79] Z. Shen and R.H. MacPhie. Input impedance of a center-fed circular patch antenna covered by a uniaxial superstrate. *Microwave and Optical Technology Letters*, 13(2):77–81, 1996.

- [80] Z. Shen and R.H. MacPhie. Scattering by a thick off-centered circular iris in circular waveguide. *IEEE Trans. Microwave Theory Tech.*, MTT-43(11):2639–2642, 1995.
- [81] N. Marcuvitz. *Waveguide Handbook*. McGraw-Hill, New York, 1951.
- [82] S. Pinhas S. Shtrikman and D. Treves. Moment method solution of the centered microstrip disk antenna involving feed and edge current singularities. *IEEE Trans. Antennas Propagat.*, AP-37(12):1516–1522, 1989.
- [83] S.A. Long M.W. Mcallister and L.C. Shen. The resonant cylindrical dielectric cavity antenna. *IEEE Trans. Antennas Propagat.*, AP-31(3):406–412, 1983.
- [84] F. Zavosh and J.T. Aberle. Single and stacked circular microstrip patch antennas backed by a circular cavity. *IEEE Trans. Antennas Propagat.*, AP-43(7):746–750, 1995.
- [85] M. Li K.A. Hummer and K. Chang. Theoretical and experimental study of the input impedance of the cylindrical cavity-backed rectangular slot antennas. *IEEE Trans. Antennas Propagat.*, AP-39:1156–1164, 1991.

IMAGE EVALUATION TEST TARGET (QA-3)



APPLIED IMAGE, Inc
1653 East Main Street
Rochester, NY 14609 USA
Phone: 716/482-0300
Fax: 716/288-5989

© 1983, Applied Image, Inc., All Rights Reserved